

Thermal analysis of the QARMAN re-entry satellite

Elien VERHEIRE

Promotoren: Frederik Desplentere

Co-promotoren: Vincent Van der Haegen
Paride Testani

Masterproef ingediend tot het behalen van
de graad van master of Science in de
industriële wetenschappen:
elektromechanica luchtvaarttechnologie

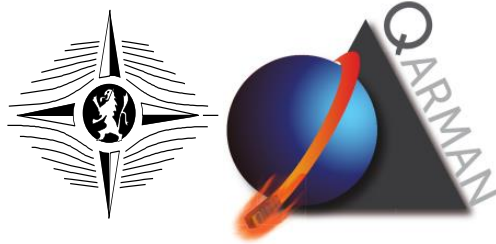
© Copyright KU Leuven

Zonder voorafgaande schriftelijke toestemming van zowel de promotor(en) als de auteur(s) is overnemen, kopiëren, gebruiken of realiseren van deze uitgave of gedeelten ervan verboden. Voor aanvragen tot of informatie i.v.m. het overnemen en/of gebruik en/of realisatie van gedeelten uit deze publicatie, wend u tot KU Leuven Technologicampus Oostende, Zeedijk 101, B-8400 Oostende, +32-59- 569000 of via e-mail iw.oostende@kuleuven.be.

Voorafgaande schriftelijke toestemming van de promotor(en) is eveneens vereist voor het aanwenden van de in deze masterproef beschreven (originele) methoden, producten, schakelingen en programma's voor industrieel of commercieel nut en voor de inzending van deze publicatie ter deelname aan wetenschappelijke prijzen of wedstrijden.

Thermal analysis of the QARMAN re-entry satellite

von Karman Institute for Fluid Dynamics
Aeronautics / Aerospace Department



QubeSat for Aerothermodynamic Research and Measurements on AblatioN

Elien VERHEIRE

Promotoren: Frederik Desplentere

Co-promotoren: Vincent Van der Haegen
Paride Testani

Masterproef ingediend tot het behalen van
de graad van master of Science in de
industriële wetenschappen:
elektromechanica luchtvaarttechnologie

Academiejaar 2014-2015

"Deze eindverhandeling was een examen. De tijdens de verdediging geformuleerde opmerkingen werden niet opgenomen."

"This thesis was an examination. The comments made during the defence are not included"

Acknowledgements

I would like to thank all the people who helped and supported me with the realisation of this Master thesis.

First of all I want to thank my promotors Prof. Dr. Ir. Frederik Desplentere, Vincent Van der Haegen and Paride Testani for their support during this project. The inspiring discussions about the thermal models and other details included in this thesis. They helped me from the beginning with this project, helped to correct parts of the text and were always attainable to answer my questions. I also got the opportunity to have an up-close look at the QARMAN satellites development with all its aspects, to have an introduction day of the ESATAN-TMS software at the university of Liège and to meet John Walker of ESA, the person who reviews the QARMAN project, during a progress meeting.

Special thanks Ertan Umit, Thorsten Scholz, Isil Sakraker, Jan Thoemel and Amadine Denis for their support. They clarified unclear issues

I also want to thank my home university KULeuven Faculteit Industriële ingenieurswetenschappen Technologicampus Oostende to give us many opportunities during our studies to develop skills that a future engineer needs.

Finally I want to thank my parents for reading my thesis and their support during my studies.

Abstract

This master thesis covers the thermal analysis of the QARMAN (Qubesat for Aerothermodynamic Research and Measurement on Ablation) satellite, as part of the QB50 project. The ultimate goal of this thesis is to take suitable measures to verify if the temperature of components are restricted to their projected margins. The QARMAN satellite needs to be thermally designed to withstand three totally thermally different phases, namely the re-entry and orbital cold and hot cases. This thermal control can only be done by passive means.

The calculation for internal temperatures needs computer models. To realise this, the software package ESATAN-TMS is chosen. One simplified heat balance has been manually calculated to check the conformity with the simulation. An own Conductive Interface Calculator has been developed in order to define systematically the conductive interfaces. This Conductor Interface Calculator also facilitates the calculation of different conductive interfaces that every satellite design contains.

The primary heat shield formed by the thermal protection system, doesn't guarantee that the electronic components survive until the end of the re-entry mission. Therefore, it had been chosen to house the electronics inside survival units (SU), which need to survive the re-entry. A screening analysis and a design of experiments indicated 3 main factors which significantly effect the components temperatures inside the SU, namely the outer surface SU emissivity, the SU insulation thickness and the length of electrical wiring. The calculated response surface has a certainty of 95% and an error of 4,20°C on the output values.

The keywords are: QARMAN – thermal design - thermal analysis – re-entry – orbital – ESATAN-TMS – Conductive Interface Calculator (CIC) – survival unit – screening analysis – Design of Experiments (DOE)

Abstract

Deze master thesis behandelt de thermische analyse van de QARMAN (Qubesat for Aerothermodynamic Research and Measurement on Ablation) satelliet, als onderdeel van het QB50 project. Het uiteindelijke doel van dit proefschrift stelt een thermisch ontwerp voor, zodanig dat er gecontroleerd kan worden dat alle componenten hun temperatuurlimieten niet overschrijden. De QARMAN satelliet is thermisch ontworpen om te kunnen functioneren in drie totaal verschillende thermische fases, namelijk de re-entry en de orbitale koude en warme fases. De thermische controle gebeurt alleen door passieve middelen.

De berekeningen voor de interne temperaturen vraagt een computer model, daarom is er gekozen om gebruik te maken van het software pakket ESATAN-TMS. Een eenvoudige warmte balans werd manueel uitgerekend en vergeleken met een simulatie. Een eigen ontwikkelde “Conductor Interface Calculator” werd ontwikkeld om op een systematische manier de “conductor interfaces” te kunnen definiëren. Deze “Conductor Interface Calculator” vergemakkelijkt ook het berekenen van soorten geleidingsweerstand die elk satellietontwerp bevat.

Het primaire hitteschild vormt onvoldoende bescherming, om te kunnen garanderen dat alle elektronische componenten de re-entry te overleven. Daarom werd er gekozen voor een concept met “Survival Units (SU)”, die elektronische componenten bevatten die de volledige re-entry moeten overleven. Een screening analyse en een “Design of Experiments” duidde drie significante parameters aan die de temperaturen van de componenten in de SU beïnvloeden, namelijk de emissiviteit van het buitenoppervlak van een SU, de isolatiedikte van de SU en de lengte van de elektrische bedrading. Het berekende responsoppervlak heeft een zekerheid van 95 % en een fout van 4,20 °C op de output waardes.

De trefwoorden zijn: QARMAN – thermisch ontwerp- thermische analyse – re-entry – orbital – ESATAN-TMS – Conductive Interface Calculator (CIC) – survival unit – screening analyse – Design of Experiments (DOE)

Table of contents

	Acknowledgements	
	Abstract	4
	Table of contents	6
	List of Figures	9
	List of Tables	11
	List of Symbols	12
	List of Abbreviations	15
	Introduction	17
	Von Karman Institute.....	17
	Motivation.....	18
	Objectives	19
	Research question	19
	Research methodology.....	21
1	QARMAN project	23
1.1	Objectives [1]	23
1.2	Satellite [3]	24
1.3	Mission design [5]	25
1.4	Subsystems [7] [8].....	26
2	The basic concepts of heat transfer [9] [10] [11]	30
2.1	Conduction [12].....	30
2.2	Radiation	31
2.2.1	Radiation intensity, emissivity and heat flux	32
2.2.2	Blackbody.....	34
2.2.3	Radiant heat exchange between 2 objects	36
2.2.4	Algebraic solution of multi-surface enclosure problems of grey bodies.....	37
2.3	Convection	38
3	The preliminary thermal design [17]	40
3.1	The thermal environment of an earth orbit.....	40
3.1.1	The orbit [17].....	40
3.1.2	Direct solar flux.....	41
3.1.3	Albedo flux.....	42
3.1.4	Earth IR	42
3.1.5	Overview thermal environment QARMAN	42
3.2	Passive and active thermal control [19].....	43
3.2.1	Overview applied thermal control systems	43
3.2.2	Thermal temperature control systems QARMAN.....	45

4	Simplified thermal model of QARMAN	47
4.1	Steady state calculation	47
4.2	Transient calculation	48
4.3	Validation of results	53
5	ESATAN-TMS and good practices	55
5.1	Geometry	55
5.2	TMM	56
5.3	GMM.....	57
5.4	Simulation and Post processing.....	58
6	Detailed design of conductor interfaces	59
6.1	Contact zone	60
6.1.1	Parameters influencing contact resistance.....	60
6.1.2	Contact conductance models	63
6.1.3	Validation of results	66
6.2	Bolted joint.....	67
6.2.1	Bolted joint resistance network [23].....	68
6.2.2	Contact resistance	70
6.2.3	Material resistance.....	72
6.2.4	Constriction resistance	73
6.2.5	Simplified thermal resistance for bolted joints [27]	74
6.3	Spacer.....	75
6.4	Soldering electronic component.....	76
6.5	Electrical wiring	80
7	QARMAN's thermal design.....	82
7.1	ESATAN-TMS model description	82
7.1.1	External geometry	83
7.1.2	Internal geometry	85
7.1.3	PCBs and electronic components	86
7.1.4	Protection units.....	87
7.1.5	Cabling	88
7.2	Thermal simulations	89
7.2.1	Thermal requirements.....	89
7.2.2	Boundary conditions.....	90
7.2.3	Simulation cases	91
7.3	Post-processed results.....	93
7.3.1	Re-entry	93
7.3.2	Cold orbital case.....	95
7.3.3	Hot orbital case.....	96
7.3.4	General conclusion	98

8	Uncertainty analysis re-entry.....	99
8.1	Screening analysis	99
8.1.1	Test parameters.....	99
8.1.2	Pareto analyse.....	101
8.1.3	Main effect plots.....	105
8.1.4	Reached temperature limit during re-entry.....	106
8.1.5	Adapted battery design.....	107
8.1.6	Different emissivities SU	108
8.2	Design of experiments.....	109
8.2.1	Basic principles [48].....	110
8.2.2	Analysis of experiments	112
8.2.3	Results	115
	Conclusions and recommendations	118
	Appendix A Calculation of the simplified thermal model of the QARMAN satellite	1
A.1	Steady state calculation	1
A.2	Transient calculation	5
	Appendix B Conductive interface calculator	1
B.1	Bolted joint.....	1
B.2	Spacer	3
B.3	Contact zone	4
B.4	Soldering of electronic components	5
B.5	Bundle of electrical cables	5
	Appendix C Uncertainty analysis re-entry.....	1
C.1	Pareto plots	1
C.2	Main effect plots.....	1
C.3	Reached temperature limit during re-entry.....	2
C.4	Results DOE.....	3

List of Figures

Figure 1:	Plasmatron facility (right picture: QARMAN TPS tested in plasma wind tunnel).....	17
Figure 2:	15 kW induction-coupled plasma minitorch.....	18
Figure 3:	Mach 6 (right) and the Mach 14 free piston hypersonic wind tunnel (left)	18
Figure 4:	Four objectives of the QB50 project.....	23
Figure 5:	Skeleton of an 1, 2 and 3 unit cube satellite [4].....	25
Figure 6:	QARMAN mission [6].....	25
Figure 7:	Differentiation of the spacecraft systems into a subsystem classification	26
Figure 8:	Heat flux normal to the isotherms, with $T_1 > T > T_2$ [12].....	31
Figure 9:	Planck's curve for various temperatures [13].....	32
Figure 10:	Radiation intensity through a unit sphere [11].....	33
Figure 11:	Calculation of dA_a	34
Figure 12:	Cross-section of a hohlraum [11].....	34
Figure 13:	Monochromatic emissive power (or hemispheric radiation intensity I_λ) of a black body, at several temperatures, in function of the emitted wavelengths [11]	35
Figure 14:	Thermal radiation between 2 surfaces [11].....	36
Figure 15:	Aerodynamic heating of a slender re-entry body (a) & blunted re-entry body (b)	39
Figure 16:	The classical orbital elements (COEs) (adapted picture [17])	40
Figure 17:	Energy balance between QARMAN satellite and space.....	42
Figure 18:	Survival unit concept (grey = negatively shaped Pyrogel®)	46
Figure 19:	Orbital plane (yellow) with β angle	52
Figure 20:	Simulation results with QARMAN seen from far sun direction.....	53
Figure 21:	QARMAN's outer surface temperature vs. time	54
Figure 22:	Work order for the thermal design.....	55
Figure 23:	a. No CIC (left) & b. Edge CIC (right).....	57
Figure 24:	Evolution of MCRT estimations (e = error and N = number of rays)	58
Figure 25:	Three types of conductors.....	59
Figure 26:	Thermal conductors (black) and thermal resistances (red) in parallel and series	60
Figure 27:	Effect of increased contact pressure	61
Figure 28:	Effect of reduced surface roughness (Above) and flatter surface (Below).....	62
Figure 29:	Influence of increased hardness and elasticity.....	62
Figure 30:	The root-mean-square roughness σ and the root-mean-square material asperity slope m of two contacting materials [23].....	63
Figure 31:	Thermal contact influenced by geometrical, thermal and mechanical properties.....	67
Figure 32:	Typical satellite bolted joint with thermal resistance	69
Figure 33:	Complete thermal resistance circuit.....	69
Figure 34:	Detailed drawing for bolt dimensions used in eqn. 4.2 [29]	70
Figure 35:	Conical pressure distribution between two bolted plates.....	71
Figure 36:	Parabolic and uniform under head pressure.....	72
Figure 37:	The aspect ratio of the cross-sectional area	73
Figure 38:	Fitted curve through graph dimensionless spreading resistance vs. parameter a/h	74
Figure 39:	Thermal resistance network of a spacer.....	75
Figure 40:	Temperature distribution in a flat heat sink (no fins) for different heat source areas	77
Figure 41:	Electronic component thermal resistance network	77
Figure 42:	Constriction resistance in electronics packaging [31].....	78
Figure 43:	Dimensionless constriction resistance versus dimensionless source area A_s [31]	78
Figure 44:	Coax cable thermal resistance network.....	81
Figure 45:	Previous concept QARMAN stowed configuration and internal parts view	82
Figure 46:	Current QARMAN satellite concept [35]	83
Figure 47:	TPS sidewall's connections	84
Figure 48:	Materials external structure	84
Figure 49:	QARMAN geometry.....	85
Figure 50:	Thermal design PC104 connection (see black).....	87
Figure 51:	Thermal design iridium component	87
Figure 52:	AeroSDS protection unit.....	88

Figure 53:	Electrical wiring QARMAN satellite.....	89
Figure 54:	Temperature boundary conditions during re-entry vs. altitude and time, for a satellite weighing 4 kg.....	91
Figure 55:	Temperature of components inside SU at the end of re-entry (1400s) (Right: with adapted heat sink and lift: without adapted heat sink)	93
Figure 56:	Schematic representation of the new heat sink	93
Figure 57:	Temperature of main SU electronic components.....	94
Figure 58:	XPLDAQ board temperature variation	94
Figure 59:	Spectrometer temperature variation	95
Figure 60:	Limits report cold orbital case with AeroSDS panels in deployed configuration.....	96
Figure 61:	Limits report cold orbital case with AeroSDS panels in deployed configuration.....	96
Figure 62:	Limits report hot orbital case with AeroSDS panels in deployed configuration	97
Figure 63:	Limits report hot orbital case with AeroSDS panels in folded configuration.....	97
Figure 64:	Transient analysis results for the temperatures of the components inside the main SU for a hot orbital case with AeroSDS panels in deployed configuration	98
Figure 65:	Thermal control system	100
Figure 66:	Pareto analysis of the main effects on battery 2	102
Figure 67:	Main effect plot for the 3 most significant parameters which influence battery 2	105
Figure 68:	Re-entry time when max. temperatures for case 2 and 3 are reached for battery 1 & 2	106
Figure 69:	Heat sink PCB-SU	107
Figure 70:	Time when the components inside the SU reaches there limit temperatures.....	109
Figure 71:	Geometric view of a 2 ³ factorial design.....	111
Figure 72:	Geometric presentation of contrasts corresponding to the main effects and interactions in the 2 ² design.....	112
Figure 73:	Two-sided T-test with significance level $\alpha=0,05$ [49]	114
Figure 74:	Surface plot (left) and contour plot (right) for Z = temperature response of battery 2	115
Figure 75:	Surface plot (left) and contour plot (right) for Z = temperature response of battery 2	115
Figure 76:	Aerogels (left: machined Microtherm® and right: Pyrogel®)	116
Figure 77:	Simplified QARMAN model.....	1
Figure 78:	Start interface conductive Interface Calculator.....	1
Figure 79:	Interface for the bolted joint	1
Figure 80:	Interface to determine other bolts	2
Figure 81:	Detailed calculation thermal resistance bolted joint	3
Figure 82:	Calculated pressure between bolted head and plate.....	3
Figure 83:	Interface for spacer	4
Figure 84:	Interface for contact zone	5
Figure 85:	Interface for soldering of an electronic component	5
Figure 86:	Interface for bundle of electrical wires	6
Figure 87:	Parteo plot for the main effects (time 1400s during re-entry selected as reference).....	1
Figure 88:	Main effect plots of battery 2 (time 1400s during re-entry selected as reference)	2
Figure 89:	Limit temperature at time t during re-entry	3

List of Tables

Table 1:	Orbital analysis cases.....	43
Table 2:	Overview of available passive and active thermal temperature devices.....	43
Table 3:	Environmental and orbital parameters used for example case.....	53
Table 4:	TMM analogies with electrical networks	56
Table 5:	Contact conductance for representative Solid-Solid interfaces	66
Table 6:	Dimensionless spreading resistance of an isoflux rectangular area.....	73
Table 7:	Temperature requirements for QARMAN components [36].....	89
Table 8:	Heat dissipation of electronic components	90
Table 9:	Orbital parameters and satellite's attitude for orbital simulations	92
Table 10:	12 test parameters for the sensitivity analysis.....	100
Table 11:	Calculated decision levels (DL) and significant effects (red marked).....	104
Table 12:	Simulation results different ebattery	108
Table 13:	Design matrix (red) and matrix of the factorial effects (bleu) for a 2 ³ -factorial design.....	110
Table 14:	Results DOE	112
Table 15:	Given parameters for the simplified thermal calculations	1
Table 16:	Total dissipated power for the different orbital cases (light grey column - used for this example calculation).....	2
Table 17:	Mass budget used for the transient calculation	5

List of Symbols

a	Internal plate radius [m] Semimajor axis [km] Surface [m ²] Width of the cross-sectional area of a constricted zone [m]
b	External bolt radius [m]
c	External plate radius [m]
C_o	Speed of light in vacuum, $2,99792458.10^8$ m/s
c_p	Specific heat capacity
d_2	Pitch diameter of a bolt [m]
d_n	Pitch diameter of the bearing surface of a nut [m]
d_{n1}	Pitch diameter of the bearing surface of a bolt [m]
D_H	Bearing surface inside diameter of a nut [m]
e	Eccentricity [-]
E	Hemispheric emissivity [W/ m ²] Young's modulus [MPa]
E'	Effective young's modulus [MPa]
E_f	Main effect on the output parameter
E_ω	Emissivity or emissive power [W/ m ² . steradian]
\bar{F}	Input value of screened variable
F	Axial tension [N]
F_{1-2}	View factor [-]
GF	Convection conductor [W/K]
GL	Linear conductor [W/K]
GR	Radiative conductor [J.m ² /K]
GV	F_{1-2} view factor in ESATAN software [-]
H	Altitude [m]
h	Planck's constant, $6,626068.10^{-34}$ J.s Height of the cross-sectional area of a constricted zone [m]
H_b	Brinell hardness [MPa]
h_c	Thermal contact conductance per unit area [W/m ² K]
H_e	Elastic micro-hardness [MPa]
H_p	Plastic micro-hardness [MPa]
i	Inclination [°]
\vec{i}	Unit vector in x-direction [-]
I_λ	Hemispheric radiation intensity [W/ m ² . m]
$I_{\lambda,\omega}$	Radiation intensity [W/ m ² . m . steradian]
$I_{o,1}$	Bessel function from the 1 st and 2 nd order [-]
\vec{j}	Unit vector in y-direction [-]
\vec{k}	Unit vector in z-direction [-]
k	Thermal conductivity [W/m.K]
k_b	Stefan-Boltzmann constant, $5,670400.10^{-8}$ W/m ² .K
k_s	Harmonic mean thermal conductivity [W/m.K]
$K_{o,1}$	Bessel function from the 1 st and 2 nd order [-]
L	Body thickness [m] Length [m]
m	Mass [kg] Material root-mean-square asperity slope [m] Initial number of effects [-]

\vec{n}	Unit vector [-]
n	Number of times that a certain test combination is repeated [-]
P	Contact pressure [N/m ² of Pa]
\dot{q}	Heat flux [W/m ²]
\dot{q}_n	Maximum heat flux [W/m ²]
\dot{Q}	Heat flow [J/s or W]
Q	Heat [J]
r	Radius [m]
$R_{Cx,y}$	Thermal contact resistance between material x and y [K/W]
R_{ctx}	Thermal constriction resistance of material x [K/W]
R_E	Earth radius, 6378.10 ³ m
R_{mx}	Thermal material resistance of material x [K/W]
S	Surface [m ²] Sample variance
s_o	First preliminary estimate for Lenth's method
T	Absolute temperature [K] Torque [N.m]
t	Time [s]
T_{orbit}	Orbital period [h]
v	Velocity [m/s ²] True anomaly [°]
w	Mass flow rate [kg/s]
x	Radius in the stress zone under the bolts head [m] Input value for the effect variable
z	Axial distance measured from the surface under the bolts head [m] Response value

Greek

∇	Scalar field
α	Amount of incident radiation which is absorbed [-] Half angle of the screw thread bolt [°] Angle of the stress cone of a bolted joint [°] Significance level of a T-test
α_s	Right ascension of the sun [°]
β	Lead angle bolt [°] Beta angle, angle between sun vector and orbital plane of the satellite [°] Regression coefficient for a 2 ^k -factorial design
δ_{ij}	Kronecker delta, as function for variables i and j [-]
δ_s	Declination of the sun [°]
γ	Gravity constant, 6,67.10 ⁻¹¹ Nm ² /kg
ε	Emittance
θ	Angle, between dA _a and the normal [°]
λ	Wavelength [μm] Relative mean plane separation [-] Argument of the Φ parameter [-]
μ	Friction coefficient of the bearing surface [-] Mean of a population
μ_n	Friction coefficient of the bearing portion [-]
ρ	Amount of incident radiation which is reflected [-] Density [kg/m ³]

σ	Boltzmann constant, $1,3806503 \cdot 10^{-23}$ J/K RMS surface roughness [m] Standard deviation
τ	Amount of incident radiation which is transmitted [-]
ν	Poisson's ratio [-]
Φ	Non-dimensional contact parameter
ω	Solid angle [steradian] Argument of the perigee [°]
Ω	Right ascension of the ascending node (=RAAN) [°]

Indices

<i>1</i>	Object 1
<i>2</i>	Object 2
(-1)	At low level
(+1)	At high level
<i>A</i>	Apogee
<i>a</i>	Apoapsis
<i>E</i>	Earth
<i>h</i>	Bolt's head
<i>i</i>	Inner
<i>n</i>	Nut
<i>net</i>	Net
<i>o</i>	Outer
<i>p</i>	Plate Periapsis Source
<i>s</i>	Sink
<i>Sat, earth</i>	Satellite facing to the earth
<i>Sat, space</i>	Satellite facing space

List of Abbreviations

ADCS	Attitude Determination and Control System
A(ero)SDS	Aerodynamic Stability and Deorbiting System
AstroDev Modem)	Astronautical Development (Here referring to AstroDev's Helium-100 Modem)
BCR	Battery Charge Regulators
BHN	Brinell Hardness Number
CAD	Computational Aided Design
CFD	Computational Fluid Dynamics
CI(C)	Conductive Interface (Calculator)
COE	Classical Orbital Elements
DL	Decision Level
DOE	Design Of Experiments
DOF	Degrees Of Freedom
e.g.	Example given
EMI	Electromagnetic Interference
EPS	Electrical Power System
ESATAN-TMS	European Space Agency Thermal Analysis Network-Thermal Modelling Suite
FD	Flatness Deviation
GMM	Geometric Mathematical Model
GPS	Global Positioning System
HD	High Definition
IC	Integrated Circuit
IMU	Inertial Measurement Unit
IR	InfraRed
IRID	Iridium (Here referring to an Iridium 9522B Satellite transceiver module)
LEO	Low Earth Orbit
LTAN	Local Time and Ascending Node
MCRT	Monte Carlo Ray Tracing
MLI	Multilayer Insulation
MPPT	Maximum Power Point Tracker
Ni	Nickel
OBC	On Board Computer
PbSn	Lead-Sink
PCB	Printed Circuit Board
PCM	Phase changing Materials
P-POD	Poly-Picosatellite Orbital Deployer
PSE	Pseudo Standard Error
QARMAN	QubeSat for Aerothermodynamic Research and Measurement of AblatioN
RAAN	Right ascension of the ascending node
RMS	Root-Mean-Square
SiC	Silicon Carbide
SS	Stainless Steel
SU	Survival Unit
STAé	Service Technique de l'Aéronautique
ThermNV	THERMal analysis model Network Viewer
TMM	Thermal Mathematical Model
TMS	Thermal Modelling Suite
TPS	Thermal Protecting System
ULg	Université de Liège

UV	Ultra Violet
VF	View Factor
VHF/UHF	Very High Frequency / Ultra High Frequency
VKI	Von Karman Institute for fluid dynamics
XPL(DAQ)	eXperimental PayLoad (Data AcQuisition)
Zr	Zirconium

Introduction

Von Karman Institute

The Von Karman Institute is an international educational and research institute for fluid dynamics, established in October 1956. But its history goes back to 1922 when a first building was erected under the ministry of defence. This first building, which housed the STAé (Service Technique de l'Aéronautique), accommodated a large low speed wind tunnel with an open return circuit and an open-jet section of 2 m diameter. This first wind tunnel was used for the aerodynamic tests of aircraft models and components during the pre-war years. New buildings, offices and tests facilities were constructed in the past decades to form the institute of today. The institute accommodates about 25 wind tunnels, covering the regimes from very low speeds to hypersonic speeds. In the high speed range, four wind tunnels are currently used for the research programs: two supersonic tunnels, Mach 2 and 3.5, a hypersonic Mach 6 blow-down facility and the world unique Longshot free piston tunnel providing a Mach 14 flow. There are also water tunnel, two phase flow, aeroacoustic, turbomachinery and plasma facilities. This thesis was in collaboration with the aeronautics and aerospace department of the VKI, which is one of the two other departments, namely the environmental and applied fluid dynamics department and the turbomachinery and propulsion department at the VKI. The following facilities are been used for development and qualification tests of the QARMAN CubeSat, namely:

- Plasmatron Facility

The plasmatron facility is a high enthalpy plasma generating facility with a test chamber kept at sub-atmospheric pressure (between 5 and 200 mbar). This facility is the most powerful induction-coupled plasma wind tunnel in the world. The electrodeless inductively-couples plasma generators generate a better plasma purity in comparison with classical arcjets, in order to reduce the pollution from any vaporized electrode material. The plasmatron will be used for the qualification testing of the TPS (Thermal Protecting System), the simulation of the complete re-entry heat flux trajectory of the QARMAN vehicle, for the calibration and qualification of the temperature, pressure and spectrometer sensors.

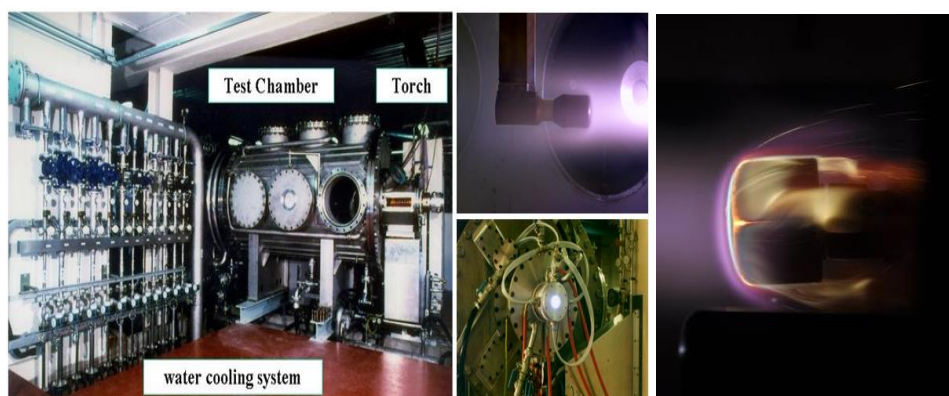


Figure 1: Plasmatron facility (right picture: QARMAN TPS tested in plasma wind tunnel)

- Minitorch and/or Micro-Wave Plasma Facilities

These are small scale plasma high enthalpy generating facilities that can be used for the testing and qualification of the spectrometer and the optical elements.



Figure 2: 15 kW induction-coupled plasma minitorch

- Mach 6 wind tunnel facility and Longshot Mach 14-20

The Mach 6 and the longshot facilities are suitable for simulating the high-aerodynamics effects on the QARMAN CubeSats at the lower altitudes of the re-entry phase. These facilities can be used in determining the shear force and aerodynamic force effects on the AeroSDS, transition to turbulence on the side walls of the CubeSat and other high Reynold number phenomena. The vacuum chamber at the end of the Mach 14 free piston hypersonic wind tunnel is also used to test the QARMAN batteries under vacuum conditions.

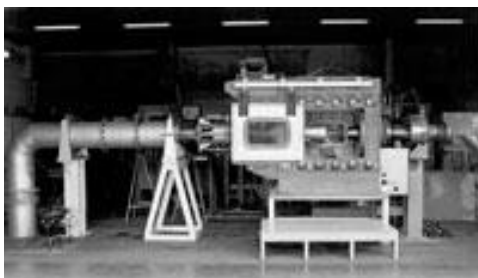


Figure 3: Mach 6 (right) and the Mach 14 free piston hypersonic wind tunnel (left)

Motivation

Research institutes have always been searching for more efficient and cheaper ways to explore space, instead of taking part in expensive space programs. Therefore we need a new concept to reduce the research costs. The QARMAN satellite will be part of a QB50 frame network. The CubeSat's allow miniaturisation of the systems and can be built in modular way. The QB50 project drives research teams to come up with solutions to miniaturise systems and systems on chip in a drastic way, which is a total new approach for packaging and integration. This project gives also the opportunity to demonstrate new technologies and new concepts (e.g. formation flying), to carry

out multiple measurements of the space environment and to give young engineers hands-on training.

The QARMAN satellite is also developed with the aim to understand the re-entry flight dynamics in order to optimize spacecraft design to ensure and to optimize the safety of future flights. Re-entry vehicles experience extreme aerodynamic heating and exothermic chemical reactions when they descend towards a planet with an atmosphere. Nowadays, space agencies try to understand the re-entry flight dynamics by using re-entry test vehicles (e.g. EXPERT, IXV or ARV) which consumes a lot money and time to qualify and develop. The QARMAN satellite could be a solution to reduce those costs and time, because:

- The QARMAN satellite is a standardized platform.
- Different configurations (e.g. sensors, trajectories, thermal protection systems, ...) can be tested on board at very low costs for scientific exploration.

Objectives

The QARMAN satellite will circle in low earth orbits (LEO's) around the earth at an altitude of about 120 up to 350 km during 3 months. The electronic components should be kept at constant temperatures, within certain margins. The worst case scenarios, such as re-entry, orbital cold and hot-cases, are simulated with ESATAN. The ESATAN-TMS thermal module, also known as ESATAN, is a numerical tool which help to predict temperatures and heat flows during these worst case scenarios. This software is a standard European thermal analysis tool to verify the thermal design of the QARMAN satellite. The outcomes of those simulations drive material choices and the position of PCB's and components. A good knowledge of material properties and conductive connections (e.g. bolted joint, spacers and bus connection) is needed to have a realistic simulation. The model will be constantly updated due to own inputs or due to design or electronic configuration inputs of other team members. The updated model is always tested to check if the changed thermal design has been influenced positively. These thesis concludes with the proposition of a critical thermal design of the QARMAN satellite, which is be able to withstand the severe orbital environment. The satellite will be able to perform in two totally different circumstances, namely extremely hot cases where electronic components should be able to dissipate there heat in a fast way and an extremely cold cases where electronic components are capable to keep their heat. The satellite should also be designed in such a way that the necessary electronic components for re-entry are able to withstand the severe thermal heat loads.

Research question

This thesis can be summarized in one main research question, namely: Is it possible to verify if the temperatures of the subcomponents are restricted to their projected margins? By answering this main question, also 4 other sub research questions need to be answered.

First sub research question

The first sub research question is phrased as following:

“What is a feasible QARMAN design in order to survive re-entry temperatures as well as the temperatures that the satellite will face during orbital hot and cold cases?”

This research question is partially answered in chapter 3. Chapter 3 gives an overview of the different possibilities to control the satellites temperatures with passive means. No active means are selected, because the small QARMAN satellite has no place to house any active means. A description of the preliminary thermal design is given in chapter 3, but according to the third research question, this preliminary design will be further developed in later chapters of this thesis.

Second sub research question

The second sub research question is phrased as following:

“Is there a possibility to conduct a preliminary analysis to compare the satellites temperatures with simulation results?”

Chapter 4 shows how a thermal simulation software calculates the temperatures of different subcomponents. By answering this research question, it became clear that only the satellites outer temperatures could be calculated with these hand calculations. The satellites outer temperature is compared with a thermal simulation to check the conformity of these determined temperature profiles. The calculation for internal temperatures needs computer effort, because more than thousands of iterations are needed and therefore is the software package ESATAN-TMS chosen to perform those thermal simulations. A thermal simulation software needs a thermal model of the satellite, so a third sub-research question rises.

Third sub research question

The third sub research question is phrased as following:

“How could the conductive conductor values be calculated in a more systematic way?”

There is a good understanding needed about the conductive conductor values, in order to define a Geometrical Mathematical Model of the QARMAN satellite. Every detail of the thermal design of the satellite, like bulk properties, surface properties, thickness of materials, geometry, conductor values,... can be programmed within ESATAN-TMS. But the conductor values need to be calculated by the thermal engineer. Therefore, an own Conductive Interface Calculator developed to facilitate the calculation of different conductive interfaces that every satellite design contains, namely: bolted joints, spacers, contact zones, soldering of electronic components and bundles of

electrical harnessing. The calculations used for this Conductive Interface Calculator is explained in more detail in chapter 6.

Fourth sub research question

The fourth sub research question is phrased as following:

“Which are the critical parameters that influence the QARMAN’s thermal design?”

A sensitivity analysis was performed to answer this fourth sub research question. The sensitivity analysis reduce the number of parameters that needed to be researched in a more detailed Design of Experiments (DOE). The outcomes of these analyses are summarized in some recommendations about the thermal design. More details about the answer on this sub research question is answered in chapter 7.

Research methodology

Various ways were used to gain the necessary information. First of all, relevant reference works to acquire the basic knowledge about the subject heat transfer were found in the library of KU Leuven Technologiecampus Oostende. This resulted in 23 books that were found, 2 were retained. The other books were not used because the subject was treated to superficial or to restricted.

The E-book “*Spacecraft thermal control handbook*”, which was recommended by Lionel Jacques from the University of Liège, is used as a reference work through this thesis. Other reference books were “*Handbook of space technology*” and “*Heat Transfer Handbook*”.

Beside this, relevant articles were found in scientific journals, such as “*Journal of thermophysics and heat transfer*” in the library of the VKI. The ResearchGate network has also been used to find relevant papers about the heat conduction through bolted joints.

The scientific journals were selected, based on the presence of one or more of the following keywords, namely: thermal contact resistance, bolted joint, satellite, spreading resistance, conductance model, microhardness, thermal spreading resistance and constriction resistance in the title of the journal. This resulted in 436 journals. The used keywords in the search field for articles in the selected magazines were bolted joint and thermal resistance. As filter, there was only searched in the title, the articles had to be at most 20 years old. The article had to be completely available and not only the abstract. The keywords were used separated and combined with the ‘AND’ operator with. Also the wildcard method was used to find variations on keywords. This resulted in 15 articles which were retained, based on the relevance of the title.

The remaining articles were judged, based on the abstract. For 15 articles, the complete text has been carefully read. The final result was 6 useful articles. Actually, some more articles have been used in this thesis, because some of the previously founded articles are also bundled in the book

the “*Heat Transfer Handbook*” of A. Bejan and A. D. Kraus which is used as a reference work for this thesis.

Structure of the thesis

Chapter 1 Describes the QARMAN project with its objectives, the concept of a CubeSat, the mission design and an explanation of the subsystems and components used in the satellite.

Chapter 2 Gives a brief introduction of the different heat transfer modes, namely conduction, convection and radiation. The equations explained in this chapter are also referred to the calculation methods of ESATAN.

Chapter 3 Presents the preliminary thermal design of the QARMAN satellite. The settings of the thermal environment within the ESATAN thermal simulations are explained. Also the different passive and active control systems are explained and an overview of the one chosen for the QARMAN satellite is given.

Chapter 4 Gives a first preliminary thermal analysis of the QARMAN satellites outer temperatures. The energy balance for a satellite is explained. The results of the preliminary hand calculations are compared with simulation results.

Chapter 5 Gives an overview of the work method used for the thermal simulations within ESATAN-TMS and the thermal simulation software used for this thesis. The post-processing of the thermal simulation data is done with the ThermNV software.

Chapter 6 Explains a detailed thermal model for contact zones, bolted joints, spacers, interfaces between electronic components and PCBs and bundles of electrical wires.

Chapter 7 Provides a description about the thermal model of the QARMAN satellite. This chapter also includes the simulation results for the orbital hot, orbital cold and re-entry cases for the QARMAN satellite.

Chapter 8 Includes a sensitivity analysis, where first some parameters were selected by a screening analysis for a further Design of Experiments (DOE) investigation.

1 QARMAN project

1.1 Objectives [1]

The QARMAN satellite, developed by the Von Karman Institute, is developed in the framework of the QB50 project. The QB50 project includes four objectives, namely: facilitating access to space, scientific research, education and in-orbit demonstration.



Figure 4: Four objectives of the QB50 project

Facilitating access to space

The aim of the QB50 project is to explore the lower thermosphere with a launching network of 50 CubeSats. The low cost sats make it possible to explore the lower thermosphere. This is a huge opportunity for space research and planetary exploration, performed by university teams and independent research institutions all over the world. The project allows to test materials and subsystems in real space flight conditions, which increases the technology readiness level for future space projects.

Scientific research

The QB50 network of satellites are going to carry out scientific research within the lower thermosphere at an altitude of 200-300 km. The QB50 sats are going to collect multi-point measurements during a period of months, instead of a few minutes, which are performed by expensive rocket flight missions nowadays. The satellites which are going to collect scientific data in the lower thermosphere, are accommodating one or more scientific sensors. The scientific sensor which are going to be used during the research are the ion-neutral mass spectrometer, the flux- Φ -probe and the multi-needle langmuir probe. The ion-neutral mass spectrometer measures the composition and structure of positive ions and neutral particles. An on-board flux- Φ -probe measures the concentration of atomic oxygen in LEO, while the cubesat loses height. This will give a better insight in the atomic oxygen distribution in LEO's, which helps to develop future LEO space missions. The multi-needle langmuir probe performs high-speed absolute electron temperature, electron density and plasma electric potential measurements. This three previous

mentioned scientific sensors are used for all the satellites except for the QARMAN satellite within the QB50 constellation, because QARMAN has its own scientific units on-board. The scientific units for the QARMAN satellite are described in some more detail in paragraph “1.4 Subsystems” section payload.

In-orbit demonstration

The QARMAN (QubeSat for Aerothermodynamic Research and Measurement of Ablation) is one of the QB50 cube sats which is not equipped with one of the above mentioned scientific sensors, but is carrying his own payload. The QARMAN sat is going to serve as a platform for the study of the atmospheric re-entry process and the associated aerothermodynamic phenomena. The satellite consists of 3 units, one unit in the front incorporates the thermal protection system, which is necessary to survive the enormous re-entry heat fluxes and heat loads up to a height of 120 km. The following objectives will be achieved during the mission: measurement of the thermal protection system (recession¹ and thermal profile within the material), measurements of the aerothermodynamic parameters (pressure, temperature distribution, plasma sheet and skin friction), species detection and measurement of the radiative heat flux. [2]

Education

The QB50 project is a great opportunity for young engineers to have some hand-on experience, by designing and testing those satellites. They are guided by experienced staff by means of reviews and feedback.

1.2 Satellite [3]

Satellites can be classified in the following weight categories, namely:

- A large satellite weighing more than 1000 kg,
- A medium-sized satellite with a weight between 500 and 1000 kg,
- A minisatellite with a mass of between 100 and 500 kg,
- A microsatellite a mass of between 10 and 100 kg,
- A nanosatellite a mass of between 1 and 10 kg,
- A picosatellite a mass of between 0,1 and 1 kg,
- A femtosatellite weighing less than 0,1 kg.

The QARMAN satellite is a cubesat consisting of 3 units. The first unit consists of the ablative heat shield to protect the satellite during the enormous heat fluxes / loads and the last 2 units are used for the components needed for the essential satellite operations. The satellite must meet the following cubesat standard dimensions of $34 \times 10 \times 10 \text{ cm}^3$. The QARMAN satellite weights almost 5 kg. Note that the QARMAN's mass deviates from the cubesat standard maximum weight of 4 kg.

¹ Recession refers to a gradual change of the shape of the ablation thermal protection system and therefore changing the aerodynamics of the re-entry vehicle.

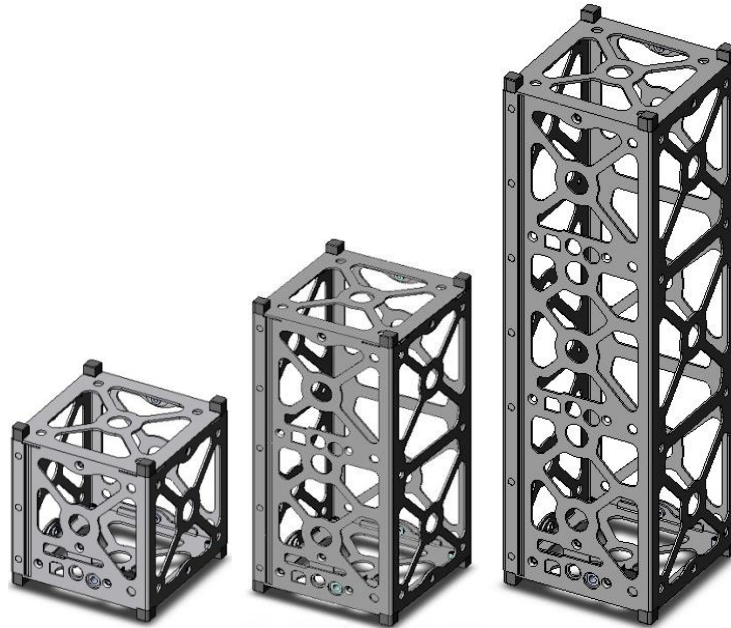


Figure 5: Skeleton of an 1, 2 and 3 unit cube satellite [4]

1.3 Mission design [5]



Figure 6: QARMAN mission [6]

The satellite starts with the “commissioning and de-tumbling phase” (PHASE 0) after the QARMAN satellite is launched and separated from the launcher. The systems are activated, health-checks runs and a first connection with the ground stations is achieved before the de-tumbling routine starts. The de-tumbling routine damps the residual angular momentum, which is needed to achieve a stable orientation. The routine stops when a resultant of the angular rate is below 1deg/sec. After this, functional tests are performed before the PHASE 1, namely the differential drag phase, starts. The QARMAN satellite chases a virtual point or another satellite. The ADCS component calculates the necessary inputs for the magnetorquers and reaction wheel, in order to achieve the reorientation of the satellite to a commanded target altitude. The satellite descends

from an altitude of 380 km to an altitude of about 350 km during phase 1. During PHASE 2 are the aeroSDS (Aerodynamic Stability and Deorbiting System) panels deployed and the deorbiting starts. The deployed panels increase the drag area of the satellite and the satellite descends down to a height of 120 km. The satellite goes in low power mode at an altitude of 150 km, in order to recharge the batteries for the re-entry phase. The re-entry phase (PHASE 3 and PHASE 4) are the last phases of the mission, where some measurements will be performed for “in-orbit demonstration” (see section above). The experimental data is stored during the black-out phase of the re-entry. The data is sent in compressed format to the ground-station right after the black-out period during PHASE 4. The period in which the satellite sends its information down to earth is expected to last for about 4-5 minutes and ends when the satellite crashes.

1.4 Subsystems [7] [8]

A spacecraft carries a payload and all the subsystems which are needed to accomplish the space mission. Every spacecraft has a more or less common design, production and operation for their subsystems. The figure 7 below gives an overview of the different subsystems within a spacecraft. This overview explains the function of the different electronic components and subsystems, which are also mentioned and named throughout the following chapters of this thesis.

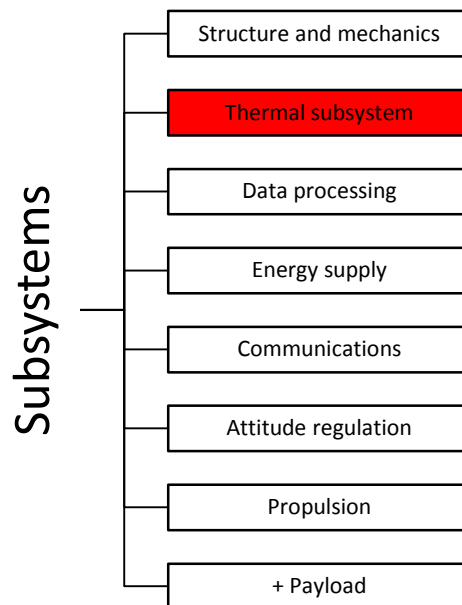


Figure 7: Differentiation of the spacecraft systems into a subsystem classification

Structure and mechanics

The mechanical structure of the QARMAN satellite accommodates all the other below mentioned subsystems, such as thermal subsystem, data processing, energy supply,... A commercial off-the-shelf chassis for cubesats can't be used for the QARMAN satellite, because the QARMAN mission demands a special design to withstand extreme thermal loads and a maximum structural load of 10,8 g. This means that a 5 kg weighing satellite undergoing a g-force of 8 g, experiences

a 40 kg force. The structure consists of ceramic structural elements and a titanium frame to withstand the enormous dynamic loads during re-entry, hinges for AeroSDS panel deployment, PCB stacks and a back plate to accommodate the VHF-UHF antennas. Dynamic aspects, such as the loads during launch, **AeroSDS panel** deployment and spinning of the satellite, effects the structure and the other subsystems. The AeroSDS panels, namely the panels for aerodynamic stability and de-orbiting systems, are mechanically deployed by torsion-spring-driven hinge systems and two burn wires which release the spring loaded mechanism. There is also a deployment system for the **VHF/UHF antenna** system. The structure of the satellite should be designed in such a way that it meets the requirements for the interface with QUADPACK (QB50 deployer) standardized interface to the launcher.

Thermal subsystem

The thermal subsystem keeps the temperatures of the components within the specified limits, not only to meet the tolerances but also for the performances of the components. For example, the maximum temperature limit for the batteries for QARMAN is 50 °C, but the batteries can still work at temperatures higher than 50 °C with reduced performances. This thermal subsystem, which is the topic of this thesis, will be explained in more detail throughout the following chapters.

Data processing

Data registered by QARMAN's payload is processed, formatted and stored on the **OBC On Board Computer**. The OBC is the central element in this data processing subsystems with the following main tasks, namely: control and surveillance of the mission, payload monitoring and control, data handling, command execution and error handling. A difference with the other subsystem hardware is that the OBC still can be modified after launch. Only the OBC will be used for time tagging to ensure a correct and consistent time stamping.

Energy supply

The **solar cells** provide power to charge the **batteries**. The **EPS** (Electrical Power System) power circuit management PCB protects the batteries from over-current, distributes the power to the other subsystems, protects the batteries from a short-circuit when leads are left during re-entry because the solar panels are burned away, converts solar power to charge the batteries and houses **Battery Charge Regulators** (BCRs). At least four regulators provide regulated power to the bus. Those regulators have an inbuilt Maximum Power Point Tracker (MPPT). This MPPT tracks the maximum illuminated side of the AeroSDS panels and switches on the dominant panels to charge the batteries. The AeroSDS have solar cells on the opposing faces, so in this configuration there will always be one side of the panel directly illuminated and the other side gets energy due to albedo illumination.

Communications

The communication subsystem makes it possible to monitor the satellites subsystems from the ground, transmits data collected by QARMAN's payload and receives mission commands from the ground stations at the VKI and the ULg (Université de Liège). The **AstroDev Helium-100 modem** with the UHF antenna system at the backplate serves as the communication system during the orbital phase. A high amount of free electrons within the plasma sheet disturbs the communication by UHF electromagnetic waves during re-entry. Therefore is an Iridium communication network used for data transmission during re-entry. Transmission of data during re-entry remains possible without any change of trajectory profile, only the location of the antenna needs to be changed to the inboard of the satellite in anti-velocity direction. The **Iridium antenna** on board of the QARMAN satellite transmits the data collected by the payload to a satellite of the Iridium satellite constellation network, which is within the transmission cone of QARMAN. That satellite of the Iridium constellation transmits at his turn the gathered data to the ground. This previous described method for radio-transmission is also used to transmit the gathered data during re-entry.

Attitude regulation

The attitude control subsystem, which is one of the most complex subsystems, controls and monitors the orientation of the spacecraft in space. It requires a good understanding of the dynamic properties of the spacecraft to define this subsystem. The **ADCS** Attitude Determination and Control Subsystem consists of a PCB stack with a Cube Control. The Cube Computer unit is activated during PHASE 0 (see 1.3 Mission design). The Cube Control board (ADCS 2) interfaces with the **reaction wheel, magnetorquer rods** and the **GPS receiver**. The reaction wheel is an electric flywheel driven at low speeds. Acceleration and deceleration causes a torque moment about the flywheel axis to change the satellites orientation. The magnetorquers also control the attitude of the satellite by interacting with local earth's magnetic field. The Cube Computer (ADCS 1) serves as an attitude control computer. PHASE 0 is called the "De-tumbling phase", where the ADCS is active for de-tumbling. Thus de-tumbling mode recovers the 3 DOF pitching, rolling and yawing motion into a stable Y-momentum mode with a residual pitch rate (around Y-axis) lower than 1deg/min. In PHASE 1 is a differential-drag-based manoeuvre used to chase a target. The ADCS actuators, namely the magnetorquers and reaction wheel, control the surface exposed to the residual atmosphere. By changing the attitude of the satellite, it is possible to change the atmospheric drag and differential force to speed up or maintain the satellites orbital velocity. This technique makes it possible for QARMAN to chase a virtual target and to maintain its relative position within the constellation when the rendezvous with the virtual target is accomplished. After PHASE 1 are AeroSDS panels deployed for PHASE 2, for the de-orbiting. Since the drag is increased by the deployment of the panels, the satellite starts to descend to a stabilized attitude. An on-board **GPS receiver, pressure sensors** and **accelerometers** inside the **IMU Inertial measurement unit** are used to determine the attitude of the satellite and to verify the feasibility of the AeroSDS Aerodynamic Determination and Control Subsystem. The GPS and the IMU are combined together in a mathematical algorithm that combines the long-term accuracy of the GPS

and the short-term accuracy of the IMU. The acceleration measured with accelerometers of the IMU, is integrated into velocity and the velocity is at his turn integrated in position with a low relative error over short time.

Propulsion

There are no active propulsive systems to control the trajectory of the QARMAN satellite. There is no propellant needed to manoeuvre the satellite to a rendez-vous point.

Payload

The payload forms the centre of the space flight mission and defines therefore the satellites requirements, because successful payload operation opens the door to mission success. The following payloads are on-board of the QARMAN satellite:

- Differential drag payload is used for an in-orbit demonstration of differential-drag-based manoeuvres. There the relative position with respect to a chaser and the trajectory of the QARMAN satellite is controlled. The differential drag payload has the Attitude Determination and Control System ADCS as main hardware.
- AeroSDS payload demonstrates the feasibility of a passive de-orbiting system. This Aerodynamic Determination and Control Subsystem has the following advantages over the ADCS, namely a lower power consumption and a reduced influence when disturbance torque increases with decreased altitude.
- The thermal protection system payload contains the ablative cork at the nose section and TPS sidepanels.
- There is also an aerothermodynamic experiment payload that consists of a set of six experiments, namely XPL01 to XPL06.
 - XPL01 front TPS efficiency experiment: 12 thermocouples measure the temperature evolution inside the cork and the recession of the ablative material.
 - XPL02 front TPS pressure experiment: The pressure along the front TPS is measured to record the pressure distribution in diagonal direction.
 - XPL03 stability experiment: Pressure sensors measure the static pressure in order to determine the stability of the satellite during the de-orbiting phase 2.
 - XPL04 Transition experiment: This experiment measures shear forces to monitor the transition from laminar flow to turbulent flow along the side panels.
 - XPL05 Side panel TPS efficiency experiment: Thermal sensors measure the temperature increase at the side panels during re-entry.
 - XPL06 Radiation experiment: A **spectrometer** will give researchers a better understanding of the re-entry plasma physics. The measured spectrum will be compared with the data gathered from ground tests in the plasmatron facilities at the VKI and simulations.

2 The basic concepts of heat transfer [9] [10] [11]

Heat transfer is the amount of energy transported from a region of higher temperature to a region of lower temperature. The coldest region is heating up and the hottest region is cooling down due to the energy transfer until an equilibrium state between both regions is established. The amount of transported heat will be presented as Q [J]. The heat flow is the amount of transported heat per time unit, presented as \dot{Q} [J/s or W]. The heat flow which flows through a unit cross-sectional area is called the heat flux \dot{q} [W/m²]. There are three different types of heat transport, often referred as *modes*, namely: conduction, radiation and convection. The thermal behaviour of the QARMAN satellite will only be affected by radiation and conduction, not by convection due to the low pressure in space. There is no convection due to the lack of air molecules.

2.1 Conduction [12]

Conduction takes place, in solids or gasses and fluids at rest, between two bodies in physical contact with each other. The conduction takes place at molecular level. The energy is transported from the molecules with high kinetic energy (high-temperature regions) to molecules with low kinetic energy (low-temperature regions). The high energetic molecules collide with molecules with low energy and exchange energy and momentum. The energy transportation, by means of collisions, occurs within gases and liquids. The heat inside dielectrics is conducted by lattice waves caused by atomic motion. The heat inside metals is mainly transported by the motion of free electrons.

The formulas for conduction are based on Fourier's law (see equation 2.1). Fourier's law says that the conductive heat flow, in a specified direction (e.g. x-direction), is proportional to:

- The *temperature gradient* $\frac{\partial T}{\partial x}$,
- The *surface* S perpendicular to the flow field direction,
- The *thermal conductivity* k which is a characteristic of the material.

$$\dot{Q} = -k \cdot S \cdot \frac{\partial T}{\partial x} = GL_{(i,j)} \cdot (T_i - T_j) \text{ with } GL_{(i,j)} = \frac{-k \cdot S}{\partial x} \quad (2.1)$$

The minus sign refers to the fact that heat is transported in the direction of decreasing temperature. The GL is the linear conductor used for the ESATAN-TMS model. The GL parameter models the heat flow path between the 2 thermal nodes i and j . The heat flow is proportional to the linear differences in the nodal temperatures.

The temperature flux (see equation 2.2) is the amount of heat flow per unit surface S .

$$\dot{q} = -k \cdot \frac{\partial T}{\partial x} \quad (2.2)$$

The \dot{q}_n flows perpendicular to the isotherms (see Figure 8), in the direction of the steepest temperature gradient.

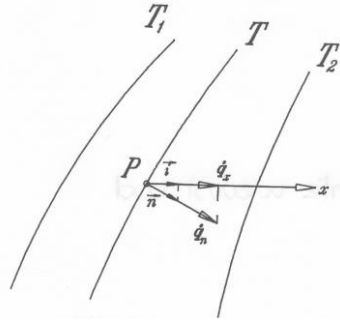


Figure 8: Heat flux normal to the isotherms, with $T_1 > T > T_2$ [12]

The equation for the heat flux \dot{q}_n can be written as following:

$$\dot{q}_n = -k \cdot \frac{\partial T}{\partial n} \quad (2.3)$$

$$\text{with the vector form of } \vec{q}_n = -k \cdot \frac{\partial T}{\partial n} \cdot \vec{n} \quad (2.4)$$

If the unit vector \vec{i} in the x-direction, starting from point P isn't coincident with the unit vector \vec{n} , \dot{q}_x can be written as following:

$$\dot{q}_x = \dot{q}_n \cdot \vec{n} \cdot \vec{i} = -k \cdot \frac{\partial T}{\partial x} \quad (2.5)$$

The Fourier's law can be written as a more general statement with P in the three-dimensional orthogonal coordinate system with \vec{i} , \vec{j} and \vec{k} .

$$\vec{q}_n = -k \cdot \frac{\partial T}{\partial x} \cdot \vec{i} - k \cdot \frac{\partial T}{\partial y} \cdot \vec{j} - k \cdot \frac{\partial T}{\partial z} \cdot \vec{k} = -k \cdot \nabla T \quad (2.6)$$

These temperature T is a scalar field, so the temperature at each point is a function of $T(x, y, z)$. The gradient of T at a certain point, defined by the x, y and z-coordinate, shows the direction of the maximum temperature change at that point. The rate of the heat transfer by conduction depends on the thermal conductivity of the material and the temperature gradient. The net heat transfer occurs in the opposite direction of the temperature gradient, because heat flows from regions with high temperatures to regions with a low temperature. The net heat transfer is in the direction of the negative temperature gradient.

2.2 Radiation

Each body with a body temperature above the absolute temperature of 0 K emits constantly electromagnetic energy, with an intensity depending on the temperature of the object and the nature of the surface. Thermal radiation occurs only in a small portion of the electromagnetic wave spectrum. The electromagnetic wave spectrum from 0,4 (near UV) and 15 μm (near IR) is the interesting spectrum for practical purposes. The incident photons with a wavelength of 0,4-15 μm can change the vibrational, rotational and electronic energy of atoms within materials, which

changes the internal energy of the materials. An internal energy change causes always an internal temperature change of the material. Heat transfer by means of radiation doesn't need any material medium like it is the case for conduction. Radiation is most efficient in a vacuum environment, because any body surrounded by any atmosphere (gas) with a body-temperature above 0 K radiates at all wavelengths.

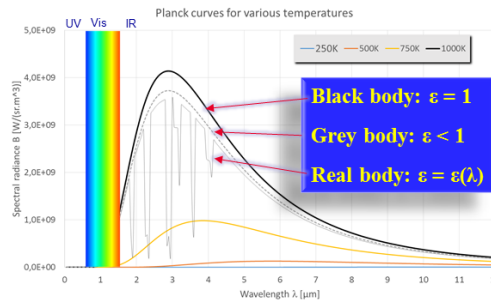


Figure 9: Planck's curve for various temperatures [13]

Figure 9 shows Planck's law, where for each wavelength at each temperature the associated hemispheric radiation intensity I_λ is shown for a black body. Grey bodies and real bodies never reaches these intensities and don't follow Planck's law. A grey body emits at every wavelength a similar radiation portion, so the emissivity ϵ is independent from the wavelength λ . The emitted radiation of a real body depends on the emitted wavelength λ .

Some definitions about how to express radiative heat transfer, will be explained first. Followed by laws of a black body into a vacuum environment, because all the other law's for thermal radiation are derived from this situation. Stefan-Boltzman's law (see eqn. 2.13), Wien's displacement law (see equation. 2.14), Planck's law (see eqn. 2.15) and Kirchoff's law are explained in section 2.2.2 Black body. An algebraic solution for the radiative heat transfer within a multi-surface enclosure of gray bodies is shown at the end of this section.

2.2.1 Radiation intensity, emissivity and heat flux

The *radiation intensity* $I_{\lambda,\omega}$ [W/ m² . steradian] is the amount of emitted energy at one specific wavelength λ , emitted I from an area dA of 1m² and radiated at a certain small angle $d\omega$ in steradians. The *hemispheric radiation intensity* I_λ [W/ m² . m] is the amount of emitted energy at one specific wavelength λ , emitted from an area dA of 1 m² and radiated over a hemisphere 2π .

The same principles such as for the radiation intensities, apply for the different emissivities with one difference that the complete spectral output with their different wavelengths will be taken in account. The *emissivity (or emissive power)* E_ω [W/ m² . steradian] is the amount of emitted energy at all the different wavelength's λ , emitted from an area dA of 1 m² and radiated at a certain small angle $d\omega$ in steradians. The hemispheric emissivity can also be calculated by the integration of $I_{\lambda,\omega}$ for all the possible incident wavelength's λ . The *hemispheric emissivity* E [W/ m²] is the amount of emitted energy at all the different wavelength's λ , emitted from an area dA of 1 m² and radiated

over a hemisphere 2π . The hemispheric emissivity can be calculated by the integration of I_λ for all the possible incident wavelength's λ .

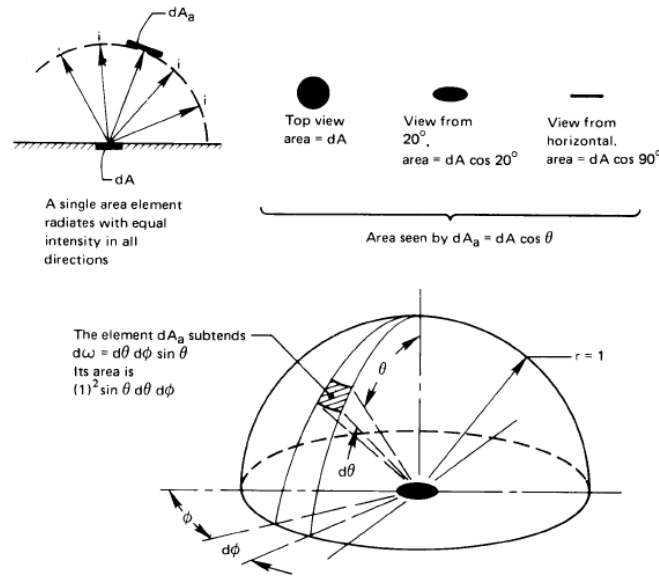


Figure 10: Radiation intensity through a unit sphere [11]

The heat flux emitted from surface dA is intercepted by surface dA_a . The amount of heat flux intercepted by dA_a depends on the angles of orientation between the two surfaces (see Figure 10). The area dA_a is normal to the radius r and is placed at an angle θ from dA .

The radiation thermal flow $\dot{Q}_{outgoing}$ (see equation 2.7) is the amount of energy which flows through the surface dA_a .

$$\dot{Q}_{outgoing} = \int E \cdot dA_a \text{ with } E = \int_0^\omega E_\omega \cdot d\omega = \int_{\lambda=0}^\infty \int_0^\omega I_{\lambda,\omega} \cdot d\omega \cdot d\lambda \quad (2.7)$$

The area seen by dA_a , depends on the angle θ from which dA_a is placed normal to the radius from dA , namely:

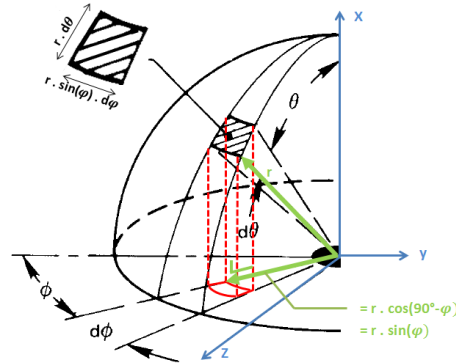
$$dA_a = \cos(\theta) \cdot dA \quad (2.8)$$

The formulas 2.7 and 2.8 are combined to form equation 2.9.

$$\dot{Q}_{outgoing} = \int \int_{\lambda=0}^\infty \int_0^\omega I_{\lambda,\omega} \cdot \cos(\theta) \cdot d\omega \cdot d\lambda \cdot dA \quad (2.9)$$

The SI unit of the solid angle ω is expressed in an amount of steradians, which is a dimensionless unit. One steradian is calculated dividing the spherical segment area by the squared radius r . This means that a $d\omega$ for a sphere is equal to $4\pi r^2/r^2 = 4\pi$. The aperture dA_a subtends $d\omega = \frac{dA_a}{r^2}$. The area of dA_a (see Figure 11) can be expressed with following equation:

$$dA_a = r \cdot d\theta \cdot r \cdot \sin(\varphi) \cdot d\varphi = r^2 \cdot \sin(\varphi) \cdot d\theta \cdot d\varphi \quad (2.10)$$

Figure 11: Calculation of dA_a

Finally the heat flux can be calculated by dividing eqn. 2.9 by dA . The total radiative heat flux is determined by integrating *radiation intensity* $I_{\lambda, \omega}$ over the entire considered spherical segment and wavelength spectrum.

$$\begin{aligned} \dot{q}_{outgoing} &= \int_{\lambda=0}^{\infty} \int_0^{\varphi} \int_0^{\theta} I_{\lambda, \omega} \cdot \cos(\theta) \cdot \frac{r^2 \cdot \sin(\varphi) \cdot d\theta \cdot d\varphi}{r^2} \cdot d\lambda \\ &= \int_{\lambda=0}^{\infty} \int_0^{\varphi} \int_0^{\theta} I_{\lambda, \omega} \cdot \cos(\theta) \cdot \sin(\varphi) \cdot d\theta \cdot d\varphi \cdot d\lambda \end{aligned} \quad (2.11)$$

2.2.2 Blackbody

The black body is a standard, used to gauge the radiative behaviour of real materials. The black body can be seen as a perfect radiator and follows exactly Planck's law (see Figure 9). Real materials don't absorb all the radiant energy but reflect a small part, this means that they emit less than a black body in order to maintain their equilibrium temperature. It is possible to construct a nearly ideal blackbody, which is a good approximation for experimental analysis, named a *hohlraum* in German (see Figure 12). The hohlraum is a sphere with a small opening. A small part of radiation crosses through the opening and is trapped inside the cavity. The cavity is kept at a constant temperature and the inside surfaces are made of non-reflecting material. The radiation rays are reflected against the surfaces and the surface material absorbs a small part of each incident ray. The energy leaving the cavity is close to that of a black body with the same cavity temperature. The radiation inside the hohlraum is isotropic, which means that the magnitude of the radiation is equal in each direction at each point inside the cavity.

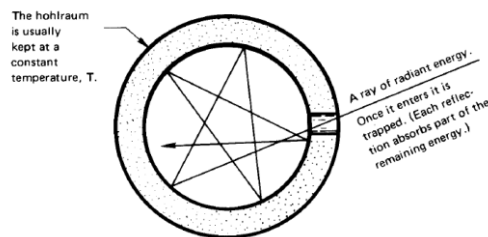


Figure 12: Cross-section of a hohlraum [11]

It is possible to define the characteristics of a black body with the help of the above presented experimental method, namely:

- The blackbody is a surface or volume which absorbs all the radiant energy of each wavelength coming from each direction.
- A blackbody is isotropic, emits all the incident energy flux at every wavelength in every direction.
- The spectrum and intensity of the emitted radiation depends only on the temperature of the blackbody surface or volume. In other words it follows Plank's law.

If radiant heat flux \dot{q} is incident at a real surface, which is not a black body, a fraction of the incident heat flux will be absorbed (α), reflected (ρ) and transmitted (τ). The relation between all those fractions can be seen in equation 2.12.

$$1 = \alpha + \rho + \tau \quad (2.12)$$

For a black body in a closed system at thermal equilibrium, all the incident energy will be absorbed and emitted again at a certain temperature, thus $\alpha_T = \varepsilon_T = 1$ and $\rho = \tau = 0$. A more general statement $\alpha_{T,\lambda,\theta} = \varepsilon_{T,\lambda,\theta}$ applies for black and non-black bodies and is called the Kirchoff's law, where absorptance and emittance depends on the surface temperature T , the wavelength λ and angle θ of incident energy. All the absorbed energy is emitted again, in order to maintain an equilibrium blackbody surface temperature. The theoretical maximum emitting energy, coming from a black body, is given by the Stefan-Boltzmann's law.

$$E_{blackbody}(T) = \int_0^\lambda I_{blackbody}(\lambda, T). d\lambda = \sigma \cdot T^4 \quad [W/m^2] \quad (2.13)$$

Stefan Boltzmann established experimentally the relation between the absolute temperature T [K] and hemispheric radiation intensity I_λ [W/ m². m] of a black body, with σ the Stefan-Boltzmann's constant $5,670400 \cdot 10^{-8}$ W/m².K for vacuum. The relation of a black body at a given temperature and the unique emitted distribution of wavelengths is given in Figure 13.

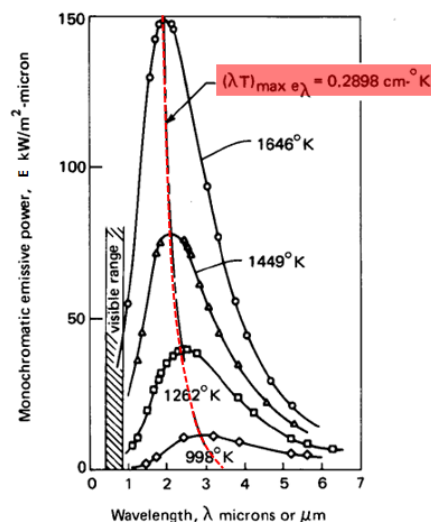


Figure 13: Monochromatic emissive power (or hemispheric radiation intensity I_λ) of a black body, at several temperatures, in function of the emitted wavelengths [11]

The hemispheric radiation intensity I_λ of a black body has always a maximum value (see red dot line) for each temperature. The maximum hemispheric radiation intensity I_λ of a blackbody at

each temperature can be determined with $\frac{dI_{blackbody}(\lambda, T)}{d\lambda} = 0$. The obeyed relationship is called the *Wien's displacement law* (see equation 2.14).

$$\lambda_{max} = \frac{2898\mu m}{T} \quad (2.14)$$

The Wien's law states that the maximum monochromatic emissive power, or hemispheric radiation intensity I_λ , decreases when the temperature increases.

The relation between the emissive power of a black body $I_{blackbody}$ and the wavelength λ was described by *Max Planck's law*.

$$I_{blackbody}(\lambda, T) = \frac{2 \cdot \pi \cdot h \cdot c_0^2}{\lambda^5 \cdot \left[e^{\left(\frac{h \cdot c_0}{k_B \cdot T \cdot \lambda} \right)} - 1 \right]} \quad [W/m^2 \cdot \mu m] \quad (2.15)$$

Where C_o is the speed of light in vacuum, $2,99792458 \cdot 10^8$ m/s; h is planck's constant $6,626068 \cdot 10^{-34}$ J.s and k_B is the Boltzmann's constant, $1,3806503 \cdot 10^{-23}$ J/K.

2.2.3 Radiant heat exchange between 2 objects

Two surfaces at a different temperature will exchange heat by means of radiation. The heat $d\dot{Q}_{1 \text{ to } 2}$ flows from surface 1 at temperature T_1 to surface 2 at temperature T_2 . For $d\dot{Q}_{2 \text{ to } 1}$ applies the same logic. The netto heat flow $d\dot{Q}_{net}$ from the hotter surface 1 to the colder surface 2. (see Figure 14)

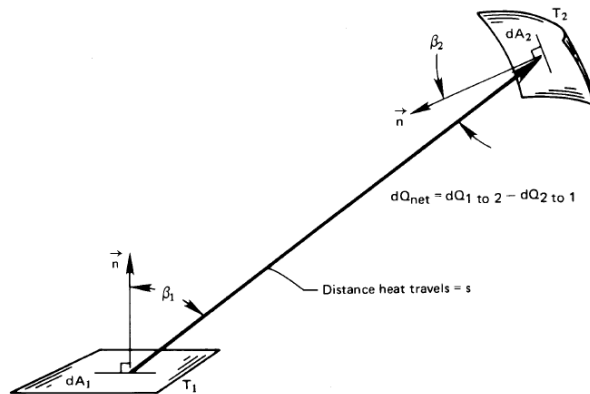


Figure 14: Thermal radiation between 2 surfaces [11]

The netto heat exchange $d\dot{Q}_{net}$ depends on the following influences:

- The temperatures T_1 and T_2 of the surfaces.
- The areas dA_1 and dA_2 of the surfaces.
- The shape and orientation of both surfaces.
- The distance s between both surfaces 1 and 2.
- The radiative properties of the surfaces.
- The medium, if it absorbs, emits or reflects radiation.
- The fact that there could be an additional surface in the environment, which reflects to one of the two surface 1 or 2 or to both surfaces.

The relation between the heat flow \dot{Q} and the emissivity E is already been presented in equation 2.7. It is supposed that only surface 1 radiates to surface 2 and that both surfaces are black bodies. All the heat which leaves surface 1 is intercepted by surface 2 ($\dot{Q}_{1\ to\ 2} = A_1 \cdot E_{blackbody}(T_1)$) and all the heat leaving surface 2 is intercepted by surface 1 ($\dot{Q}_{2\ to\ 1} = A_1 \cdot E_{blackbody}(T_2)$). The netto heat, transferred from the hotter surface to the colder surface, is noted with Q_{net} .

$$\dot{Q}_{net,between\ blackbodies} = \dot{Q}_{1\ to\ 2} - \dot{Q}_{2\ to\ 1} = A_1 \cdot E_{blackbody}(T_1) - A_1 \cdot E_{blackbody}(T_2) \quad (2.16)$$

The emissivity of a black body $E_{blackbody}(T)$ can be replaced by Boltzmann's law (2.13).

$$\dot{Q}_{net,between\ blackbodies} = A_1 \cdot \sigma \cdot (T_1^4 - T_2^4) \quad (2.17)$$

Equation 2.17 will be multiplied with a correction factor, named the *view factor* F_{1-2} , if the first object sees other objects in the environment, besides object 2.

$$\dot{Q}_{net,between\ blackbodies} = A_1 \cdot \sigma \cdot F_{1-2} \cdot (T_1^4 - T_2^4) \quad (2.18)$$

An emittance factor ε_1 of surface 1 is added to equation 2.18 for the calculation of the radiative heat flow between two non-black bodies. The emittance factor of a non-black surface is lower than the value 1, which is used for black bodies, because the absorbed heat by a non-black surface is also smaller than 1. Some of the incident heat flow at a non-black surface is transmitted through the material and/or reflected by the surface. Equation 2.12 has shown that the total sum of absorbed (α), reflected (ρ) and transmitted (τ) heat flow is 1.

$$\dot{Q}_{net,between\ non-blackbodies} = \underbrace{A_1 \cdot \sigma \cdot \varepsilon_1(T_1) \cdot F_{1-2} \cdot T_1^4}_{\text{Emitted from plate 1}} - \underbrace{A_1 \cdot \sigma \cdot \alpha_1(T_1, T_2) \cdot F_{1-2} \cdot T_2^4}_{\text{Radiated from plate 2 and absorbed by plate 1}} \quad (2.19)$$

The absorptance α_2 depends on the temperatures of both plates, because T_1 determines the absorptance capacity of plate 1 and T_2 determines which radiative heat spectrum is radiated from plate 2.

The view factor can be calculated with the following equation 2.20.

$$F_{1-2} = \frac{1}{A_1} \cdot \int_0^{A_1} \int_0^{A_2} \frac{\cos(\beta_1) \cdot \cos(\beta_2)}{\pi \cdot s^2} \cdot dA_2 \cdot dA_1 \quad (2.20)$$

2.2.4 Algebraic solution of multi-surface enclosure problems of grey bodies

The radiating surfaces of the satellite are considered to be grey. The following assumptions, according to the ESATAN-TMS calculations, are been made:

- All surfaces are perfectly diffuse (radiation properties are independent of wavelength and direction).
- Emissivity ε is equal to absorptivity α .
- Surface emissivities and absorptivities are constant.

- All surfaces are independent of wave length (grey surface).
- Opaque surface with $\tau=0$.

This means that equation 2.19 can be adapted to a grey body approximation, with $\varepsilon_1 \cong \alpha_1$, namely:

$$\begin{aligned} \dot{Q}_{net,between\ non-blackbodies} &= A_1 \cdot \sigma \cdot \varepsilon_1(T_1) \cdot F_{1-2} \cdot T_1^4 - A_1 \cdot \sigma \cdot \alpha_1(T_1, T_2) \cdot F_{1-2} \cdot T_2^4 \\ &\cong A_1 \cdot \sigma \cdot \varepsilon_1 \cdot F_{1-2} \cdot T_1^4 - A_1 \cdot \sigma \cdot \varepsilon_1 \cdot F_{1-2} \cdot T_2^4 \\ &= A_1 \cdot \sigma \cdot \varepsilon_1 \cdot F_{1-2} \cdot (T_1^4 - T_2^4) \end{aligned} \quad (2.21)$$

The GR is a radiative conductor used for the ESATAN-TMS model. The value of the GR conductor is $A_1 \cdot \sigma \cdot \varepsilon_1 \cdot F_{1-2}$. The software ESATAN-TMS will take in account multiple reflections for the calculation of the view factor F_{1-2} , named the GV conductor in the ESATAN software.

The algebraic solution for a multi-surface enclosure problem of grey bodies is presented below [11] is formulated in a matrix equation.

$$\sum_{j=1}^n \left[\frac{\delta_{ij}}{\varepsilon_i} - \frac{(1-\varepsilon_j)}{\varepsilon_j \cdot A_j} \cdot A_i \cdot F_{i-j} \right] \cdot Q_{net_j} = \sum_{j=1}^n A_i \cdot \sigma \cdot F_{i-j} \cdot (T_i^4 - T_j^4) \text{ for } i = 1, \dots, n \quad (2.22)$$

For numerical purposes, a Kronecker delta has been introduced.

$$\delta_{ij} = \begin{cases} 1 & \text{for } i = j \\ 0 & \text{for } i \neq j \end{cases} \quad (2.23)$$

This Kronecker delta is a function consisting of 2 variables, namely i and j. If both variables are equal, the function is 1 and otherwise 0.

2.3 Convection

Convection takes place when a fluid flow pasts an object and heat is absorbed by the object or fluid flow, depending on which one is hotter. The thermal heat transfer isn't affected by convection in space due to lack of air molecules. But convection will affect the QARMAN satellite's temperature during the re-entry of the earth's atmosphere at high speeds.

When the satellite starts its re-entry it has a high amount of kinetic energy due to its high speed and a high amount of potential energy due to its distance to earth. But when the satellite reaches the earth's surface it has a small height and velocity, which automatically reflects in a small amount of kinetic and potential energy. So where is all the residual energy? A shock wave is formed when the re-entry vehicle moves faster than the local speed of sound. *H. Julian Allen* concludes in his research, namely "A study of the motion and aerodynamic heating of missiles entering the earth's atmosphere", that blunt shapes have lower convective heat-transfer in the region of the nose. The air behind the shock wave is compressed, which causes an enormous pressure and temperature increase. The increased temperature gives the air molecules energy and this leads to dissociation and ionization of the air molecules. The heat fluxes of these hot gases are convected to the

spacecraft's body. The kinetic energy has been transformed into heat, which results in a temperature increase. [14]

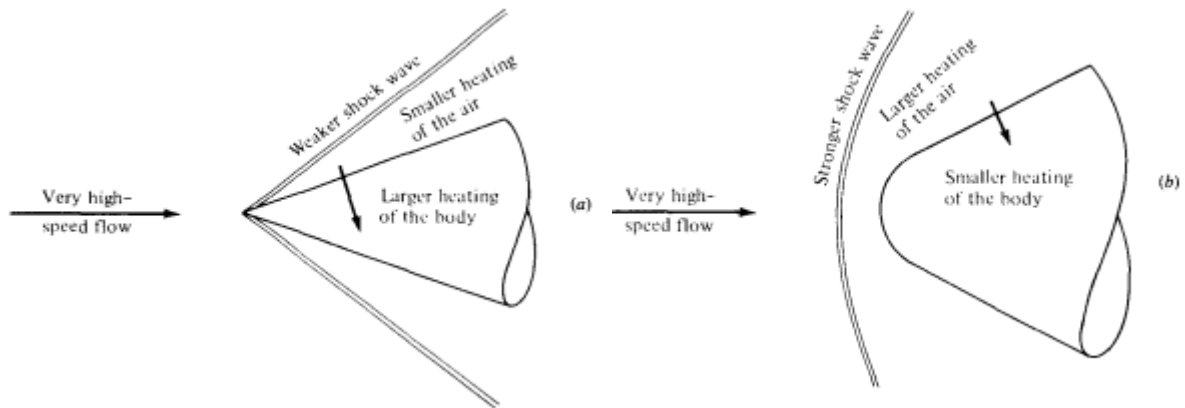


Figure 15: Aerodynamic heating of a slender re-entry body (a) & blunted re-entry body (b) [15]

When the shock wave is attached to the slender re-entry body (see Figure 15 a), a large amount of the heat flux is convected to the body and a small amount of heat is exchanged to the air around the re-entry vehicle. The heat is spread out over a larger area by using blunted re-entry bodies, which reduces local heating. When the shock wave is detached shock (see Figure 15 b) to the blunted body, a small amount of the heat flux is convected to the body and a large amount of heat is exchanged to the air around the re-entry vehicle. The convective heat flux during re-entry can be calculated by the following formula 2.24. [16]

$$\dot{q} = 1,83 \cdot 10^{-4} \cdot v^3 \cdot \sqrt{\frac{\rho}{r_{nose}}} \quad (2.24)$$

Where v is the vehicle's velocity, ρ the air density and r_{nose} the vehicles nose radius.

The equation 2.24 is a rough approximation of the convective heat flux during re-entry, which only counts for axisymmetric bodies. The convective heat of the QARMAN satellite has been predicted by CFD analyses and tests in the plasmatron.

3 The preliminary thermal design [17]

3.1 The thermal environment of an earth orbit

It's very important to understand the different parameters to describe the orbit of the satellite and its thermal environment. The classical orbital elements (COEs) and the three heat sources for the satellite in space environment, namely direct sunlight, reflected sunlight off earth (albedo) and the IR energy emitted from the earth are present. All those parameters will be used to define the radiative case in the ESATAN program, which describes the QARMAN orbital cold and hot case model.

3.1.1 The orbit [17]

The classical orbital elements describe the size, orientation, shape of the earth orbit and the position of the satellite in that orbit. A method of describing the orbit was developed by *Johannes Kepler*. Kepler's method consists of describing the orbit and spacecraft position with 6 orbital elements, known as the COEs (Classical orbital elements). The 6 COEs are:

- The *semimajor axis* a describes the orbital size.
- The *eccentricity* e defines the orbital shape.
- The *inclination* i and *right ascension of the ascending node* Ω describes the orientation of orbital plane in space.
- The *argument of the perigee* ω gives information about the orientation of the orbit within the plane.
- The *true anomaly* v represents the spacecraft's location.

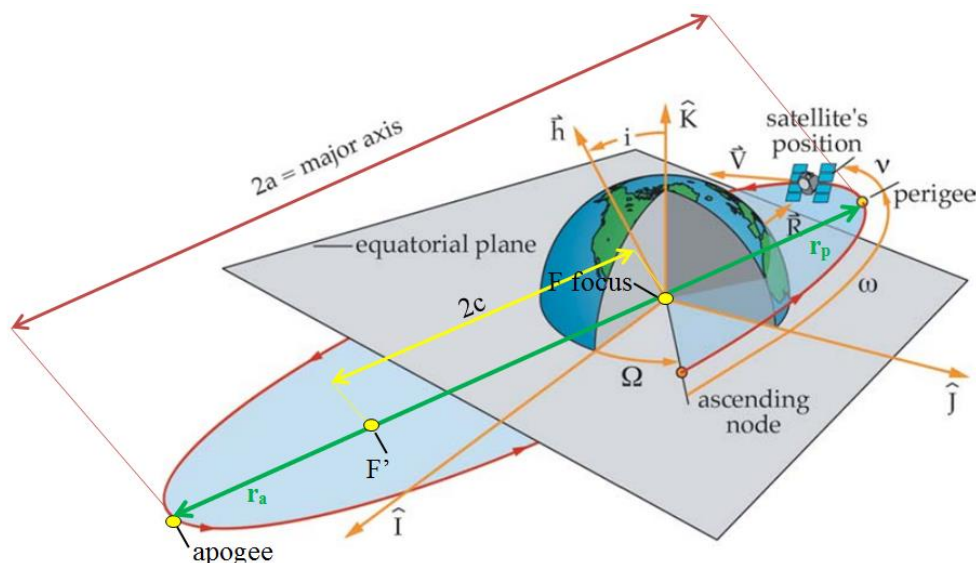


Figure 16: The classical orbital elements (COEs) (adapted picture [17])

The *semi major axis* a is half the major axis $2a$ and takes the distances across the orbits plane in account. The *major axis* $2a$ is bounded by the *perigee or periapsis* (closest point to earth, see yellow dots figure 16) and the *apogee of apoapsis* (furthest point to earth, see yellow dots figure 16). The orbits shape, described with the eccentricity factor, gives an idea of the “out of roundness” of the orbital plane (see figure 16 light blue plane). The *eccentricity* e is given by the ratio of the distance $2c$ between the two foci F' and F and the major axis length $2a$. The eccentricity e can also be expressed in terms of the *periapsis radius* r_p (see green arrow figure 16) and the *apoapsis radius* r_a (see green arrow figure 16), namely $e = \frac{(r_a - r_p)}{(r_a + r_p)}$. The spacecraft describes a circle orbit when e is equal to 0 and an ellipse when the value of e is between 0 and 1. The geocentric-equatorial coordinate system, consisting of the axes \hat{I} , \hat{J} and \hat{K} , is the coordinate system used for the equatorial plane (see figure 16 grey plane). The \hat{K} axis runs through the poles of the earth and the \hat{I} axis is the *vernal equinox*. The *inclination angle* i , with a range of values between 0° and 180° , describes the tilt of the orbital plane with respect to the equatorial plane (see figure 16 blue plane). The *right ascension angle* Ω is the angle between the principal direction \hat{I} of the equatorial plane and the ascending node. The angle Ω , with its values ranging from 0° to 360° , gives information about the rotation of the orbital plane around the \hat{K} axis starting from the \hat{I} axis in eastward direction. The fifth classical orbital element is *the argument of perigee* ω , an angle with values ranging from 0° up to 360° , is measured from the ascending node to the perigee along the orbital path in the direction of the satellites motion. The perigee is a point on the spacecraft's orbital path which is closest to the earth's surface, which is also the point that gives the best HD pictures of the earth's surface. The *true anomaly* v , with values ranging from 0° up to 360° , is the angle measured from the perigee to the spacecraft's motion vector \hat{R} along the orbital path in the direction of the satellites motion.

3.1.2 Direct solar flux

The direct solar flux incident heating (see figure 17) on the satellite is the largest heating source. The sun itself is a very stable energy source, with emitted radiation which varies only with 1% during the 11-year solar cycle. But the earth's orbit is elliptical, which means that we have the largest earth-sun distance of 152.10^6 km during summer (around the 4th of July) and the smallest earth-sun distance of 147.10^6 km during winter (around the 3rd of January) [18]. The incident sunrays are assumed to be parallel because the distance between the sun and the earth is extremely large. The intensity of the sunlight reaching the earth varies with $\pm 3,3\%$ due to the difference in distance between the earth surface and the sun. The intensity of the sunlight reaching the earth during summer solstice is 1414 W/m^2 . The intensity of sunlight reaching the earth during winter solstice is 1322 W/m^2 [19]. The thermal behaviour of the QARMAN satellite will be tested in a cold and hot case. A difference in incident solar intensity can't be set within the ESATAN software, but the “sun planet distance” will be adapted to define a winter or summer solstice. The cold and hot orbital cases aren't only affected by the winter and summer solstice, there are also other parameters which are needed to be taken in account, such as the position of the orbit (explained in 3.1.1 Orbit) and if the satellite is in the eclipse or not. A complete overview of the used parameters is presented in table 1.

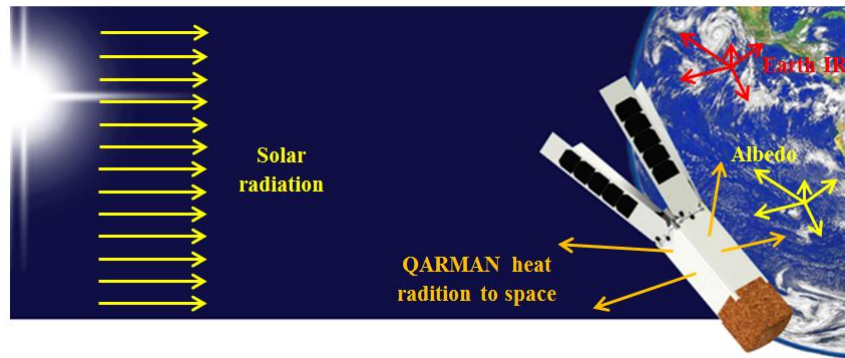


Figure 17: Energy balance between QARMAN satellite and space

The IR emitted by the sun has a shorter wavelength than IR emitted by bodies near room-temperature. This knowledge will be used for the selection for the finishes of the thermal protection side panels of the QARMAN satellite. The finishes of the TPS reflects highly the solar spectrum and has a high emissivity at room temperatures. This means that the incident solar heat load is minimized and the satellites ability of emitting internal heat is maximized.

3.1.3 Albedo flux

The albedo is the flux of sunlight reflected from a planet or moon. The earth albedo is expressed by a fraction of the incident sunlight which is reflected back by the earth. The albedo flux is rather difficult to evaluate and is highly variable, because the amount of reflected sunlight depends on the environmental conditions. The reflectivity depends on the fact that the sunlight rays are incident on a continental or oceanic region, on a snow/ice coverage, on cloud coverage,... The earth albedo reflectance coefficient is selected to be 0,4 for the hot orbital case and 0,2 for the cold orbital case. [20]

3.1.4 Earth IR

A part of the incident solar rays will be reflected by the albedo, another part is absorbed by the earth's surface and eventually reemitted as earth IR energy. The reemitted IR energy depends on the local temperature of the earth's surface, the amount of clouds and the emissivity of various terrain. The earth IR emissivity depending on the previous given factors, ranges from 0,75 to 0,99 [21]. Some of the radiation emitted from the earth is absorbed by the clouds, so the given values will be reduced due to the cloud coverage. These local variations of the earth emitted IR are less significant than the variations of the albedo [19], so the ESATAN default value of 1 for the IR emissivity shall be selected.

3.1.5 Overview thermal environment QARMAN

An overview (see table 1) of the thermal and orbital environment for the cold and hot orbital cases for the QARMAN satellite is presented below.

Table 1: Orbital analysis cases

Parameter	Cold case	Hot case	Reference
Season	Winter solstice	Summer Solstice	[12]
Sun planet distance [km]	147.10 ⁹	152.10 ⁹	[9]
Solar declination [°]	-23,45	23,45	[12]
Planet temperature [K]	288	288	[12]
Altitude of apogee [km]	380	380	[6]
Altitude of perigee [km]	380	380	[6]
Inclination [°]	98	98	[6]
Right ascension of the ascending node Ω [°]	115	115	[6]
LTAN	8AM	12AM	[6]

3.2 Passive and active thermal control [19]

The thermal control systems are needed to keep the temperatures of internal components and structures within its temperature boundaries, for all the operating modes and all the thermal environments where the QARMAN satellite maybe exposed to.

3.2.1 Overview applied thermal control systems

The thermal control systems are divided in 2 mean categories, namely the passive and active control devices. The following table 2 gives an overview of the possible available thermal control systems.

Table 2: Overview of available passive and active thermal temperature devices

Passive devices	Active devices
Insulation	Radiators
Thermal surface finishes	Heaters
Heat switches	Louvers
Phase-change materials	Pumped fluid loops
Satellites geometry (conductive paths)	

The passive devices don't need any heaters or mechanical systems. Only passives devices will be used in the QARMAN satellite, because the QARMAN cubesat has a very small volume of 34×10×10 cm³ like mentioned in paragraph 1.2. The small volume of the cubesat will be fully occupied by the PCBs, with the needed electronic components for the satellites functions. There

is no place for complex mechanical systems, such as radiators, heaters, louvers¹ or fluid loops. Therefore only the functionality of the passive devices is discussed below.

Insulation can be achieved by multilayer insulation (MLI) and single-layer radiation barriers, which are the most common thermal control elements on a spacecraft. The MLI blankets prevent excessive heat loss of electronic components and excessive heating due to high environmental heat fluxes. The single-layer radiation barrier materials are placed where less thermal protection is needed, because those materials are lighter and easier to manufacture. The layered blanket consists of multiple layers with low-emittance films.

Thermal surface finishes know a wide range of different wavelength dependent coatings available on the market. The coatings, which are space qualified, mostly don't have problems with outgassing or mechanical adhesion. Highly polished foils can be used to minimize the absorbed solar energy and IR emission. Solar reflectors (white paints, silver or aluminium blanked Teflon,..) minimize absorption of solar energy. Black paints, used on internal components (e.g. batteries), to facilitate radiant heat transfer. The influence of different internal surfaces can be easily evaluated by simulation without any change of the satellites geometry.

Heat switches are installed between warm electronic or instrumentation and a heat sink. The heat switches, also known as thermal switches don't control the temperatures of components by opening or closing electrical circuits at given temperatures, like thermostats do, but adapt the heat conduction path. If the temperature of the hot component rises above the set-point, the switch conductance rises (act as a good thermal conductor) and the heat flows easily to the heat sink. The contrary is also valid when the temperature of the component drops below the set-point, the switch conductance decreases (act as a good thermal insulator) and the heat flows easily from the heat sink to the component.

Phase-change materials (PCMs) protect components which are only switched on for a short duty-cycle for cooling down and protect highly power dissipating components from over-heating. Another function of phase-change materials is that energy is stored, by phase change, when electronics are working and this stored energy is dissipated again when the electronics are inoperative. The 4 possible phase-changes are: solid-liquid (melting/freezing), liquid-gas (vaporization), solid-gas (sublimation) and anhydrous salt transformations. Only solid-liquid and anhydrous salt transformations are often used, because vaporization and sublimation has too large volumetric changes. The following materials are often used, namely: inorganic salt hydrates, organic compounds (e.g. paraffin), eutectics of organic materials and natural inorganic elements (e.g. sulphur).

¹ Louvers are an assembly of blades which cover a underlying baseplate with a low absorptance-to-emissivity ratio. By controlling the blade positions becomes the louver system a variable emissivity radiator. While closed, louvers decouple and shield the baseplate from the surrounding environment, but while open, there is a radiative coupling.

The **Satellite's geometry** can be thermally tuned by insulating some parts or promoting the heat transfer by means of conductive paths. The conductive path consists of a network of bolts, spacers, washers, frames, plates, ...

3.2.2 Thermal temperature control systems QARMAN

The stacks of PCBs (Printed Circuit Boards) and survival unit boxes are connected via screws and spacers with the frame of the satellite, which provides a direct conduction path to the satellite's structure. The satellite's structure acts as a large heat sink. A detailed thermal model for bolted joints and spacers is given in chapter 6.

The outer walls of the satellite consists of a composition of a silicon carbide layer and a fiberfrax layer. A fiberfrax blanket is made of ceramic fibres which have a high thermal stability. The fiberfrax is characterized by: low thermal conductivity, low heat storage, light weight and excellent thermal shock resistance. Most of the fiberfrax materials are composed by alumina-silicate fibres. This thermal protection system (TPS), a composite insulation, is needed for protection against the high convective and radiative heating during atmospheric re-entry. The silicon carbide is a high emissivity coating for the fiberfrax ceramics. The outer satellite TPS panels are conductive insulated from the satellites frame.

The nose of the QARMAN satellite is a cork TPS system which protects the satellite against enormous aerothermodynamic heat loads caused by the plasma sheet generated by the plasma during re-entry, with a temperature field ranging between more than 1090 °C at the a height of 120 km and 221,85 °C at the a height of 30 km.

The outer surfaces of the survival units need to have a low emissivity. It has originally been chosen to have a low emissivity foil at the in- and outside of the survival unit. This previous mentioned idea about low emissivity foils has been further developed throughout this thesis. The PCB inside the box is glued to an aluminium plate, which acts as a heat sink. The temperatures of the internal components don't drop below minimum allowable operating temperatures, in the periods during an eclipse (satellite in earth's shadow) or during a cold radiative case. The mass of the heat sink is high enough to stock heat during the hot cases and will keep the components hot during the cold cases. The low emissivity foil makes it possible to keep heat inside the survival unit during the cold radiative cases. The low absorptivity foil acts as a protective layer during hot radiative orbital case, which protects the inside of the survival unit from heating up. The waste heat of electronic components is conducted to the heat sink. The TPS will be filled with Pyrogel®, a lightweight and low-conductive material. The aerogel protects the electronic components from overheating during the hot radiative case and especially during re-entry. The Pyrogel® has been selected over the aerogel, because the aerogel is very brittle and difficult to manufacture. The following concept (see figure 18) has been chosen, namely a titanium box filled with a Pyrogel® layer.

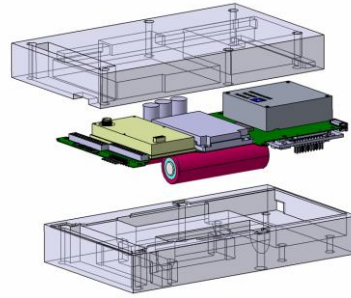


Figure 18: Survival unit concept (grey = negatively shaped Pyrogel®)

Pyrogel® is the product name of an aerogel type produced by Aspen Aerogels. Throughout the thesis is Pyrogel used instead of Pyrogel®, which refers to an aerogel insulation material. Aerogels are ultra-light materials, where the liquid component of the silica gel has been replaced by a gaseous component. The process of extracting the liquid from the gel is called supercritical drying. The air gaps are surrounded by chains of amorphous silica agglomerates, with particle sizes ranging from 5 to 25 nm.

4 Simplified thermal model of QARMAN

This chapter gives a first preliminary thermal analysis of the QARMAN satellites outer temperatures. The temperature of the satellite is influenced by the thermal environment, as explained in Chapter 3, and the dissipated heat of electronic components inside the satellite. This chapter explains the energy balance of a satellite. At first, a steady state calculation is performed, which will be the reference for future transient calculations of the temperature behaviour of the satellite during orbit.

4.1 Steady state calculation

Bodies in the low atmosphere, namely low earth orbits (LEO), interact only with a small amount of atoms and molecules. Heat transfer by means of convection can therefore be neglected in the thermal design. The low earth orbit satellite interacts with the environment only by radiation. The temperature of the satellites subsystems are affected by conduction and radiation. The heat fluxes from the satellite to the environment, from the environment to the satellite and between the subsystems are controlled, in order to get the temperatures of the subsystems within their temperature limits. Heat exchange between the satellite and its environment is influenced by the optical properties of the external surfaces of the satellite. The resistance of the thermal flow between subsystems, see Chapter 5, plays an important role for the heat conductance between the systems.

The general satellites heat balance is based on the principle of conservation of energy, which states that there is no energy created or destroyed. The heat balance consists of the algebraic sum of the following terms:

- Heat generated by electronic components: \dot{Q}_{elect} ,
- Heat fluxes entering the satellite: \dot{Q}_{albedo} , \dot{Q}_{sun} and \dot{Q}_{earth} ,
- Heat fluxes exiting the satellite: $\dot{Q}_{sat,earth}$ and $\dot{Q}_{sat,space}$,
- Heat accumulated by the system during orbit.

The heat balance is balanced when the amount of incoming heat equals to the amount of heat leaving the system. The heat balance is called a steady state calculation, if the term “heat accumulated by the system during orbit” equals to zero. A formula for the steady state heat balance of the QARMAN satellite can be derived based on this knowledge, see equation 4.1.

$$\begin{aligned} \dot{Q}_{in} &= \dot{Q}_{out} \\ \dot{Q}_{elect} + \dot{Q}_{albedo} + \dot{Q}_{sun} + \dot{Q}_{earth} &= \dot{Q}_{sat,earth} + \dot{Q}_{sat,space} \end{aligned} \quad (4.1)$$

The following terms are used in equation 4.1:

- \dot{Q}_{elect} heat dissipated by electronic components,
- \dot{Q}_{albedo} reflected sunlight by the earth’s surface = $\alpha_{sun} \cdot albedo_{flux} \cdot A_{sat} \cdot F_{earth-sat} \cdot I_{sun}$,

- \dot{Q}_{sun} heat radiated by the sun = $\alpha_{sun} \cdot A_{sat} \cdot F_{sun-sat} \cdot I_{sun}$,
- \dot{Q}_{earth} IR radiated by the earth's surface = $\alpha_{IR} \cdot A_{sat} \cdot F_{earth-sat} \cdot I_{earth}$,
- $\dot{Q}_{sat,earth}$ heat radiated back to earth = $\epsilon_{IR} \cdot A_{sat} \cdot F_{sat-earth} \cdot \sigma \cdot (T_{sat}^4 - T_{earth}^4)$,
- $\dot{Q}_{sat,space}$ heat radiated back to deep space = $\epsilon_{IR} \cdot A_{sat} \cdot F_{sat-space} \cdot \sigma \cdot (T_{sat}^4 - T_{space}^4)$.

The steady state temperature for the satellite receiving solar rays can be calculated with formula 4.2. The solar panels receive sun energy, which is converted to electrical energy to charge the batteries.

$$T_{sat,sun} = \sqrt[4]{\frac{\frac{\dot{Q}_{elect}}{\epsilon_{IR} \cdot A_{sat} \cdot F_{sat-space} \cdot \sigma} + \frac{\alpha_{sun} \cdot albedo_{flux} \cdot F_{earth-sat} \cdot I_{sun}}{\epsilon_{IR} \cdot A_{sat} \cdot F_{sat-space} \cdot \sigma}}{\frac{\alpha_{sun} \cdot F_{sun-sat} \cdot I_{sun}}{\epsilon_{IR} \cdot A_{sat} \cdot F_{sat-space} \cdot \sigma} + \frac{\alpha_{IR} \cdot A_{sat} \cdot F_{earth-sat} \cdot I_{earth}}{\epsilon_{IR} \cdot A_{sat} \cdot F_{sat-space} \cdot \sigma}} + T_{space}^4} \quad (4.2)$$

The term $\epsilon_{IR} \cdot A_{sat} \cdot F_{sat-earth} \cdot \sigma \cdot (T_{sat}^4 - T_{earth}^4)$ is neglected, because the following simplification is assumed: $T_{earth} \approx T_{sat}$.

No direct sun rays, neither reflected sun energy from the earth's surface reaches the satellite when the satellite is in the shadow of the earth. The formula 4.2 is rewritten for the steady state temperatures during this eclipse (see equation 4.3).

$$T_{sat,eclipse} = \sqrt[4]{\frac{\frac{\dot{Q}_{elect}}{\epsilon_{IR} \cdot A_{sat} \cdot F_{sat-space} \cdot \sigma} + \frac{\alpha_{IR} \cdot A_{sat} \cdot F_{earth-sat} \cdot I_{earth}}{\epsilon_{IR} \cdot A_{sat} \cdot F_{sat-space} \cdot \sigma}}{T_{space}^4}} \quad (4.3)$$

The calculations of the QARMAN's steady state heat balance for an orbital cold case with the solar panels in folded positions is given in Appendix A.1.

4.2 Transient calculation

The temperature variation between the two previous presented steady-state conditions, namely the satellite in the sun and in the shadow of the earth, is calculated with a transient calculation with an invariant temperature distribution $\partial T / \partial t$. This transient calculation is based on the following equation 4.4, where the thermal energy flow \dot{Q} is proportional to the temperature T.

$$\dot{Q} = T \cdot \sum_{i=1}^n m_i \cdot c_{p,i} \quad (4.4)$$

Where the spacecraft is considered as being a thermal node with a mass m_i and a specific heat capacity $c_{p,i}$ of the n different subsystems. Differentiating equation 4.4, with respect to time, leads to the new equation 4.5.

$$\frac{d\dot{Q}}{dt} = \frac{dT}{dt} \cdot \sum_{i=1}^n m_i \cdot c_{p,i} \quad (4.5)$$

The temperature for the steady state calculation is independent of time, which means that $\frac{dT}{dt} = 0$ and $\dot{Q}_{in} = \dot{Q}_{out}$. The satellite tries to reach the maximum equilibrium temperature $T_{sat,sun}$ during the heat up phase and the minimum equilibrium temperature $T_{sat,eclipse}$ during the eclipse phase. But both phases, namely the heating up and the eclipse phase, change more quickly than the time that satellite needs to reach its equilibrium temperatures. As a result, the actual satellites temperature T_a differs from the calculated equilibrium temperatures.

The differential equation 4.5 is rewritten and the term \dot{Q} is replaced by the equation 2.21, namely: $A_1 \cdot \sigma \cdot \varepsilon_1 \cdot F_{1-2} \cdot (T_1^4 - T_2^4)$ with $T_1 > T_2$. The parameters of equation 2.21 are defined as following:

- Surface A_1 is the outer surface A_{sat} of the QARMAN satellite,
- Emissivity ε_1 is defined as ε_{IR} , an averaged IR emissivity value for satellite outer surface,
- The view factor F_{1-2} is equal to 1, because the satellite outer surface “sees” the environment in every direction,
- The temperature $T_1 = T_{sat,sun}$ (see eqn. 4.2) and $T_2 = T(t)$ for the heating up phase and $T_1 = T(t)$ and $T_2 = T_{sat,eclipse}$ (see eqn. 4.3) for the cooling down phase.

The following equation 4.6 is integrated for the **heating up phase**. The satellites actual temperature T_a is higher than the starting temperature T_o .

$$\frac{\sum_{i=1}^n m_i \cdot c_{p,i}}{\varepsilon_{IR} \cdot A_{sat} \cdot \sigma} \cdot \int_{T=T_o}^{T_a} \frac{1}{(T_{sat,sun}^4 - T^4)} dT = \int_{t=0}^t dt = \Delta t_{sun} \quad (4.6)$$

The term $(T_{sat,sun}^4 - T^4)$ is factorised as $(T_{sat,sun}^2 - T^2) \cdot (T_{sat,sun}^2 + T^2)$. The integral $\int_{T=T_o}^{T_a} \frac{1}{(T_{sat,sun}^2 - T^2) \cdot (T_{sat,sun}^2 + T^2)} dT$ is integrated by using the method of partial fractions.

The term inside the integral is split in partial fractions, where $T(t)$ is time dependent and $T_{sat,sun}$ is a constant term.

$$\frac{1}{(T_{sat,sun}^2 - T^2) \cdot (T_{sat,sun}^2 + T^2)} = \frac{(a \cdot T + b) \cdot (T_{sat,sun}^2 + T^2)}{(T_{sat,sun}^2 - T^2) \cdot (T_{sat,sun}^2 + T^2)} + \frac{(c \cdot T + d) \cdot (T_{sat,sun}^2 - T^2)}{(T_{sat,sun}^2 + T^2) \cdot (T_{sat,sun}^2 - T^2)}$$

$$\Leftrightarrow a \cdot T \cdot T_{sat,sun}^2 + a \cdot T^3 + b \cdot T_{sat,sun}^2 + b \cdot T^2 + c \cdot T \cdot T_{sat,sun}^2 - c \cdot T^3 + d \cdot T_{sat,sun}^2 - d \cdot T^2 = 1$$

$$\left. \begin{array}{l} T \cdot T_{sat,sun}^2 \cdot (a + c) = 0 \\ T^3 \cdot (a - c) = 0 \\ T_{sat,sun}^2 \cdot (b + d) = 1 \\ T^2 \cdot (b - d) = 0 \end{array} \right\} \text{solve} \rightarrow \begin{array}{l} a = c = 0 \\ b = d = \frac{1}{2 \cdot T_{sat,sun}^2} \end{array}$$

$$\Leftrightarrow \int \frac{1}{(T_{sat,sun}^4 - T^4)} dT = \frac{1}{2 \cdot T_{sat,sun}^2} \cdot \int \left(\underbrace{\frac{1}{(T_{sat,sun}^2 - T^2)}}_{\textcircled{1}} + \underbrace{\frac{1}{(T_{sat,sun}^2 + T^2)}}_{\textcircled{2}} \right) dT; \text{ with}$$

the terms $\textcircled{1}$ and $\textcircled{2}$ further elaborated below.

① $\int \frac{1}{(T_{Sat,sun}^2 - T^2)} dT = \int \frac{1}{(T_{Sat,sun} - T) \cdot (T_{Sat,sun} + T)} dT$; with the term inside the integral partial fractioned as following:

$$\frac{1}{(T_{Sat,sun} - T) \cdot (T_{Sat,sun} + T)} = \frac{a \cdot (T_{Sat,sun} + T)}{(T_{Sat,sun} - T) \cdot (T_{Sat,sun} + T)} + \frac{b \cdot (T_{Sat,sun} - T)}{(T_{Sat,sun} + T) \cdot (T_{Sat,sun} - T)}$$

$$\Leftrightarrow a \cdot T_{Sat,sun} + a \cdot T + b \cdot T_{Sat,sun} - b \cdot T = 1$$

$$\Leftrightarrow \left. \begin{array}{l} T_{Sat,sun} \cdot (a + b) = 1 \\ T \cdot (a - b) = 0 \end{array} \right\} \text{Solve} \rightarrow a = b = \frac{1}{2 \cdot T_{Sat,sun}}$$

$$\begin{aligned} \Leftrightarrow \int \frac{1}{(T_{Sat,sun}^2 - T^2)} dT &= \frac{1}{2 \cdot T_{Sat,sun}} \int \frac{1}{(T_{Sat,sun} - T)} + \frac{1}{(T_{Sat,sun} + T)} dT \\ &= \frac{1}{T_{Space}} \int \frac{1}{2 \cdot (T + T_{Sat,sun})} - \frac{1}{2 \cdot (T - T_{Sat,sun})} dT = \frac{1}{T_{Space}} \cdot \text{arctanh} \left(\frac{T}{T_{Sat,sun}} \right) \end{aligned}$$

$$\textcircled{2} \int \frac{1}{(T_{Sat,sun}^2 + T^2)} dT = \frac{1}{T_{Sat,sun}} \int \frac{T_{Sat,sun}}{(T_{Sat,sun}^2 + T^2)} dT = \frac{1}{T_{Sat,sun}} \cdot \text{arctan} \left(\frac{T}{T_{Sat,sun}} \right)$$

The solution for the transient calculation for the QARMAN satellite in the heating up phase (see eqn. 4.7) is solved by combining the above given intermediate results in equation 4.6.

$$\begin{aligned} \Delta t_{sun} &= \frac{\sum_{i=1}^n m_i \cdot c_{p,i}}{\varepsilon_{IR} \cdot A_{sat} \cdot \sigma} \cdot \int_{T=T_o}^{T_a} \frac{1}{(T_{Sat,sun}^4 - T^4)} dT \\ \Delta t_{sun} &= c_{sun} \cdot \left[\left(\text{arctanh} \left(\frac{T_a}{T_{Sat,sun}} \right) + \text{arctan} \left(\frac{T_a}{T_{Sat,sun}} \right) \right) - \left(\text{arctanh} \left(\frac{T_o}{T_{Sat,sun}} \right) + \text{arctan} \left(\frac{T_o}{T_{Sat,sun}} \right) \right) \right] \quad (4.7) \end{aligned}$$

With the temperature at the end of the eclipse used as starting temperature T_o for the heating up phase and the constant c_{sun} calculated with equation 4.8. The calculation for the time Δt_{sun} when the satellite is exposed to sunlight during one orbital revolution is explained below in equation 4.14.

$$c_{sun} = \frac{\sum_{i=1}^n m_i \cdot c_{p,i}}{\varepsilon_{IR} \cdot A_{sat} \cdot \sigma \cdot 2 \cdot T_{Sat,sun}^3} \quad (4.8)$$

For the **cooling phase** (see eqn. 4.10) is equation 4.9 integrated, with the equilibrium temperature $T_{Sat,eclipse}$ lower than the temperature T of the satellite. The temperature of the satellite decreases from the starting temperature T_o to the actual temperature of the satellite T_a at the end of the eclipse phase. The temperature T_o , used for the heat transfer formula 4.9 for the cooling down phase, is equal to the actual temperature T_a at the end of the heating up phase. The minus sign within the left hand side of equation 4.9 makes sure that the solution of the integral has a positive value, because $T_o > T_a$ and $T(t) > T_{Sat,eclipse}$.

$$\frac{\sum_{i=1}^n m_i \cdot c_{p,i}}{\varepsilon_{IR} \cdot A_{sat} \cdot \sigma} \cdot - \int_{T=T_o}^{T_a} \frac{1}{(T^4 - T_{Sat,eclipse}^4)} dT = \int_{t=0}^t dt = \Delta t_{eclipse} \quad (4.9)$$

The term $(T^4 - T_{Sat,eclipse}^4)$ is factorised as $(T^2 - T_{Sat,eclipse}^2) \cdot (T^2 + T_{Sat,eclipse}^2)$. The integral $\int_{T=T_o}^{T_a} \frac{1}{(T^2 - T_{Sat,eclipse}^2) \cdot (T^2 + T_{Sat,eclipse}^2)} dT$ is integrated by using the method of partial fractions.

$$\begin{aligned} & \frac{1}{(T^2 - T_{Sat,eclipse}^2) \cdot (T^2 + T_{Sat,eclipse}^2)} \\ &= \frac{(a \cdot T + b) \cdot (T^2 + T_{Sat,eclipse}^2)}{(T^2 - T_{Sat,eclipse}^2) \cdot (T^2 + T_{Sat,eclipse}^2)} + \frac{(c \cdot T + d) \cdot (T^2 - T_{Sat,eclipse}^2)}{(T^2 + T_{Sat,eclipse}^2) \cdot (T^2 - T_{Sat,eclipse}^2)} \end{aligned}$$

$$\Leftrightarrow a \cdot T^3 + a \cdot T \cdot T_{Sat,eclipse}^2 + b \cdot T^2 + b \cdot T_{Sat,eclipse}^2 + c \cdot T^3 - c \cdot T \cdot T_{Sat,eclipse}^2 + d \cdot T^2 - d \cdot T_{Sat,eclipse}^2 = 1$$

$$\Leftrightarrow \left. \begin{aligned} T^3 \cdot (a + c) &= 0 \\ T \cdot T_{Sat,eclipse}^2 \cdot (a - c) &= 0 \\ T^2 \cdot (b + d) &= 0 \\ T_{Sat,eclipse}^2 \cdot (b - d) &= 1 \end{aligned} \right\} \text{Solve} \rightarrow \begin{aligned} a &= c = 0 \\ b &= \frac{1}{2 \cdot T_{Sat,eclipse}^2} \\ d &= -\frac{1}{2 \cdot T_{Sat,eclipse}^2} \end{aligned}$$

$$\Leftrightarrow -\int \frac{1}{(T^4 - T_{Sat,eclipse}^4)} dT = \frac{1}{2 \cdot T_{Sat,eclipse}^2} \cdot \int \left(\frac{-1}{(T^2 - T_{Sat,eclipse}^2)} + \frac{1}{(T^2 + T_{Sat,eclipse}^2)} \right) dT; \text{ with}$$

①
②

the terms ① and ② further elaborated below.

$$\begin{aligned} \textcircled{1} \int \frac{-1}{(T^2 - T_{Sat,eclipse}^2)} dT &= \int \frac{-1}{(T - T_{Sat,eclipse}) \cdot (T + T_{Sat,eclipse})} dT \\ &= \frac{1}{T_{Sat,eclipse}} \int \frac{-T_{Sat,eclipse}}{(T - T_{Sat,eclipse}) \cdot (T + T_{Sat,eclipse})} dT = \frac{1}{T_{Sat,eclipse}} \cdot \operatorname{arccoth} \left(\frac{T}{T_{Sat,eclipse}} \right) \end{aligned}$$

$$\textcircled{2} \int \frac{1}{(T^2 + T_{Sat,eclipse}^2)} dT = \frac{1}{T_{Sat,eclipse}} \int \frac{T_{Sat,eclipse}}{(T_{Sat,eclipse}^2 + T^2)} dT = \frac{1}{T_{Sat,eclipse}} \cdot \operatorname{arctan} \left(\frac{T}{T_{Sat,eclipse}} \right)$$

The solution for the transient calculation for the QARMAN satellite in the cooling down phase (see eqn. 4.10) is solved by combining the above given intermediate results in equation 4.9.

$$\begin{aligned} \Delta t_{eclipse} &= \frac{\sum_{i=1}^n m_i \cdot c_{p,i}}{\varepsilon_{IR} \cdot A_{sat} \cdot \sigma} \cdot -\int_{T=T_o}^{T_a} \frac{1}{(T^4 - T_{Sat,eclipse}^4)} dT \\ \Delta t_{eclipse} &= c_{eclipse} \cdot \left[\left(\operatorname{arccoth} \left(\frac{T_a}{T_{sat,eclipse}} \right) + \operatorname{arctan} \left(\frac{T_a}{T_{sat,eclipse}} \right) \right) - \left(\operatorname{arccoth} \left(\frac{T_o}{T_{sat,eclipse}} \right) + \operatorname{arctan} \left(\frac{T_o}{T_{sat,eclipse}} \right) \right) \right] \end{aligned} \quad (4.10)$$

Temperature T_o is the temperature of satellite at the end of the sun phase. The constant $c_{eclipse}$ is calculated with equation 4.11. The time of the eclipse, namely $\Delta t_{eclipse}$, is calculated with equation 4.10. With the temperature at the end of the heating up phase used as starting temperature T_o for the eclipse phase and the constant $c_{eclipse}$ calculated with equation 4.11. The calculation for the time $\Delta t_{eclipse}$ when the satellite is exposed to earth's shadow during one orbital revolution is explained below in equation 4.13.

$$C_{eclipse} = \frac{\sum_{i=1}^n m_i \cdot c_{p,i}}{\varepsilon_A \cdot A_{sat} \cdot \sigma} \cdot \frac{1}{2 \cdot T_{sat,eclipse}^3} \quad (4.11)$$

The β angle is the angle defined between the sun vector and the orbital plane of the satellite (see yellow line figure). This β angle isn't one of the 6 orbital elements (see paragraph 3.1.1) which defines the unique orbital plane of the spacecraft by Kepler's method, but all satellites with the same β angle at a given altitude are exposed to the sun for the same amount of time. The beta angle varies between $+90^\circ$ and -90° . A positive beta angle is used for satellites which are orbiting clockwise around the earth, seen from the sun point of view. A negative beta angle is used for satellites which go around the earth counter-clockwise, seen from the sun. The most extreme situation for satellites is a circular orbital plane with an β angle of -90° or $+90^\circ$, where the satellite is constantly exposed to the sun independent from its altitude.

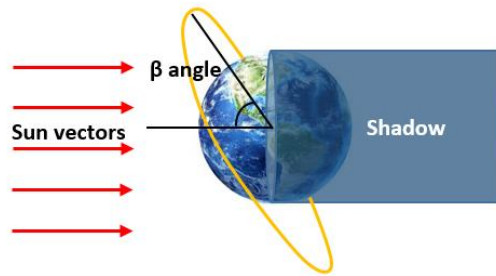


Figure 19: Orbital plane (yellow) with β angle

The β angle is mathematically defined with following equation 4.12. Where the beta angle is a function of the following angles, namely: declination to the sun δ_s , orbit inclination i , right ascension of the ascending node Ω and right ascension of the sun α_s .

$$\beta = \arcsin(\cos(\delta_s) \cdot \sin(i) \cdot \sin(\Omega - \alpha_s) + \sin(\delta_s) \cdot \cos(i)) \quad (4.12)$$

The eclipse fraction $\Delta t_{eclipse}$ [s] depends on the earth radius R_E ($6378 \cdot 10^3$ m), the altitude of the orbit H , the orbital period T_{orbit} [h] and the orbit beta angle β .

$$\Delta t_{eclipse} = \frac{T_{orbit}}{\pi} \cdot \cos^{-1} \left(\frac{\sqrt{(H^2 + 2R_E H)}}{(R_E + H) \cdot \cos \beta} \right) \quad (4.13)$$

The time when the satellite is exposed to the sun, is the time for one orbital revolution Δt_{orbit} reduced with the eclipse time. The period for one orbital revolution depends on the mass of the earth M_E ($5,97 \cdot 10^{24}$ kg), the gravity constant γ ($6,67 \cdot 10^{-11}$ Nm²/kg) and the radius a . The radius a is defined by the sum of the earth radius R_E and the altitude of the apogee H_A , where H_A is equal to the radius of the satellites orbit R for circular orbits.

$$\Delta t_{sun} = \Delta t_{orbit} - \Delta t_{eclipse} = \sqrt{\frac{4 \cdot \pi^2 \cdot a^3}{\gamma \cdot M_E}} - \Delta t_{eclipse} = \sqrt{\frac{4 \cdot \pi^2 \cdot (R_E + H_A)^3}{\gamma \cdot M_E}} - \Delta t_{eclipse} \quad (4.14)$$

The orbital period needed for equation 4.13 can be calculated by dividing the time for one orbital revolution Δt_{orbit} by 3600 s, in order to have the orbital period's unit in hours (see equation 4.15).

$$T_{orbit} = \frac{\Delta t_{orbit}}{3600 s} \quad (4.15)$$

A transient calculation of the QARMAN's heat balance for an orbital cold case with the solar panels in folded positions is given in Appendix A.2.

4.3 Validation of results

The calculation for the heat balance based on the QARMAN satellite model with folded solar panels in an orbital cold case is presented in Appendix A. One side of the satellite is facing the earth. The satellite is orbiting at a height of 380 km above the earth's surface in a circular orbit with an inclination angle of 98°. Table 3 gives an overview of the environmental and orbital parameters that were used to determine the orbital case for the ESATAN-TMS simulation and the hand calculation presented in appendix A.

Table 3: Environmental and orbital parameters used for example case

Environmental and orbital parameters	
I_{sun}	1368 W/m ²
Albedo flux	0,3
I_{earth}	246,5 W/m ²
T_{space}	3K
Altitude of the satellite H	380 km
Declination of the sun δ_s	23,45°
Orbit inclination i	98°
Right ascension of the ascending node Ω	0°
Right ascension of the sun α_s	0°

Figure 20 shows the results for the orbital simulation for the above mentioned environmental and orbital parameters (see table 3) seen from a far sun direction. This means that the sun can be situated in the positive direction of the X-axis. The satellites displayed in the front of the sphere of figure 20 are in sun phase and the satellites in the back are in eclipse. The behaviour of the averaged outer temperatures is displayed in figure 21, assuming that the satellite is one thermal node with the same material and thermal properties as the real satellite.

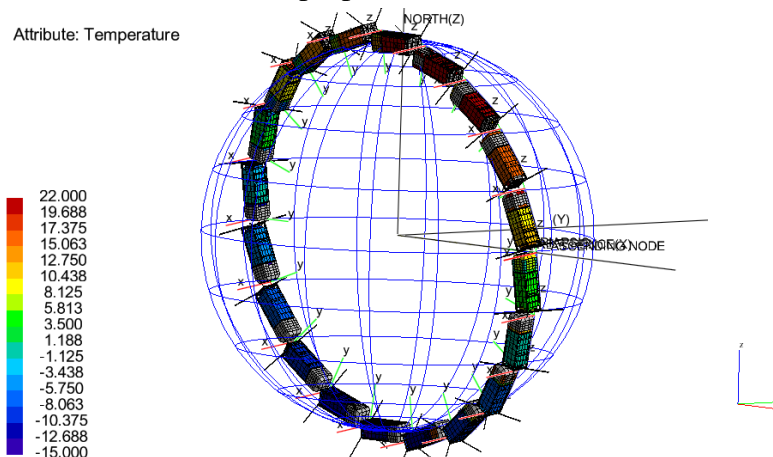


Figure 20: Simulation results with QARMAN seen from far sun direction (temperature indication in degrees Celsius)

There were 10 iterations needed for the hand calculation to calculate the temperature that the outer surfaces of the satellite reaches at the end of the eclipse and sun phase. Figure 21 shows the results for a period of 1 orbit. It can be clearly seen in the graph below that the system, namely the whole satellite, tends to have an inertia. The system has a thermal response time. There is heat stored in the satellite materials, meaning that it takes time to heat up and cool down the satellite. The red graph shows the temperature fluctuations for an ideal case, where the satellite starts to heat up immediately when the eclipse phase ends and starts to cool down when the sun phase ends. The temperature fluctuation is more realistic approximated with the ESATAN-TMS, which is presented in the blue graph in figure 21. Here is the thermal inertia of the satellite visible, because the satellite is still heating up for some more seconds when it enters the shadow and remains also cooling down when the satellite is already exposed to the sun rays. This previous conclusion explains also the lower calculated maximum temperature and higher calculated minimum temperature in comparison with the minimum and maximum temperatures found by the ESATAN-TMS simulations. Figure 21 shows a relative error of 2,1 % for the calculated maximum temperature and a percent error of 4,9 % for the calculated minimum temperature. Those low percentage errors values confirms that the simplified thermal model is a good approach of the real satellites orbital temperature behaviour, but doesn't take in account the thermal inertia of the satellite.

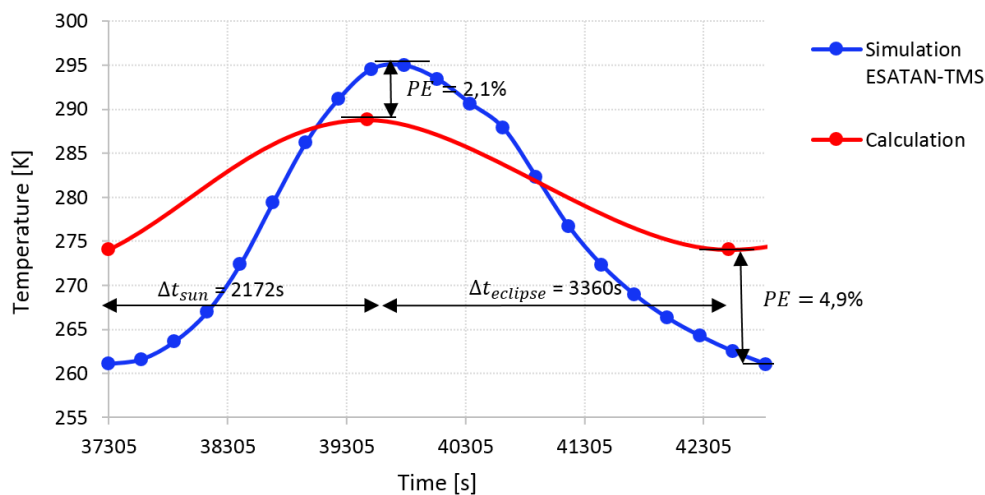


Figure 21: QARMAN's outer surface temperature vs. time
(Blue: ESATAN-TMS simulation & red: calculation (see Appendix A))

Calculations of the internal temperatures with a simplified thermal model is impossible, because complex calculations of view factors, internal conductive and radiative links have to be taken in account. A typical thermal design contain easily several thousand of radiative couplings. Therefore, the software ESATAN-TMS is chosen to simulate and evaluate the temperature behaviour of the QARMAN satellite in more detail during re-entry and several other orbital cases. The next chapter explains in more detail the methodology of the thermal simulation software ESATAN-TMS.

5 ESATAN-TMS and good practices

This chapter gives an overview of the work method used for the thermal simulations. ESATAN-TMS is the thermal simulation software used for this thesis. All the post-processing of the thermal simulation data is done with the ThermNV software. It is important to have a good understanding of the working of ESATAN-TMS, in order to know how to build a realistic thermal model of the QARMAN satellite. Some lessons learned along the way are also mentioned in this chapter, in the hope to help new ESATAN-TMS users.

Computer simulations of the temperature behaviour of the spacecraft reduce the high costs which come along with the physical testing of the satellite. There are simulations performed with different orbital cases that the satellite will encounter during its life. Normally one physical test will be performed with a real satellite model to verify the results of the physical test under known conditions with the simulations. This means that great reliance is placed on the simulations of the thermal model of the satellite.

The European Space Agency Thermal Analysis Network-Thermal Modelling Suite ESATAN-TMS is commonly used for the thermal analysis of spacecraft. ESATAN-TMS's main program language is based on MORTRAN. The first two steps, namely GMM and TMM, were respectively performed with ESARAD and ESATAN software in the older versions of the simulation program. Those initially separated modules are nowadays merged into one thermal analysis program ESATAN-TMS, in order to have a more user friendly program. The following iterative work method, see figure 22, is used to build the thermal model.

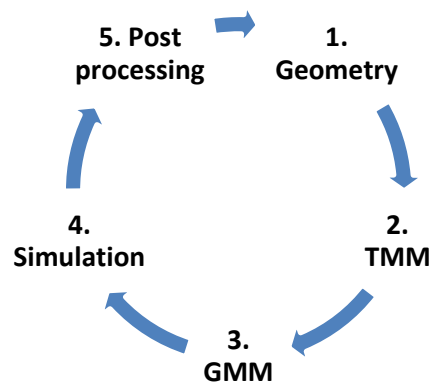


Figure 22: Work order for the thermal design

5.1 Geometry

The geometry model is modelled in such a way that it is representative with the real design, without neglecting essential features. Many people are used to work with CAD-packages where 3D-models

are built up by making a 2D sketch and extrude that sketch. In ESATAN-TMS are 3D-geometries built up by flat geometrical shapes. The thermal engineer uses its own judgement to choose where to approximate complex structures by simple shapes. For example, small electronic components, in comparison with the general dimensions of the satellite, can be approximated by thermal nodes. There is also no need to design spacers, bolts and connectors in geometrical detail, but insert a comparable thermal resistance between the two connected points. More about how to calculate these thermal resistances in chapter 6. Shapes within ESATAN-TMS are defined by coordinates, therefore it is good to have a well thought representative geometrical design. So the first thing to do before starting to design the geometry is to think about the reference plane. It is also important to keep track of the used node numbers. The node numbers are manually entered into the ESATAN-TMS program and therefore are overlapping node numbers common mistakes. If two neighbour nodes have a large temperature difference, it is worth to check the node numbering. The optical and bulk properties of the geometrical elements are defined during the geometry phase.

5.2 TMM

The Thermal Mathematical Model is based on a lumped parameter method. This means that thermal properties are assigned to thermal nodes. The thermal nodes are situated in the middle of an element and different elements form a geometry. A geometry is “meshed” into several elements. The thermal properties assigned to the nodes, are equally distributed over the nodes surface area. So calculated temperatures are constant over a node and energy is transferred among those nodes. The TMM has analogies with an electrical network as show in table 4.

Table 4: TMM analogies with electrical networks

Quantity	Thermal system	Electrical system
Potential	T	U
Flow	\dot{Q}	I
Resistance	R	R
Conductance	GL	$1/R$
Capacitance	C	C
Ohm's Law	$R = T/\dot{Q}$	$R = U/I$

There is a possibility to Auto-Generate conductive links within the TMM. But there are difficulties to define a conductive interface for an edge contact, either automatically or manually. A horizontal surface can't be connected by means of a CI Conductive Interface with a horizontal surface (see figure 23 a), unless the horizontal surface is divided in 2 surfaces (see figure 23 b) with an edge in the middle where the 3 edges of the 3 surfaces touch each other.

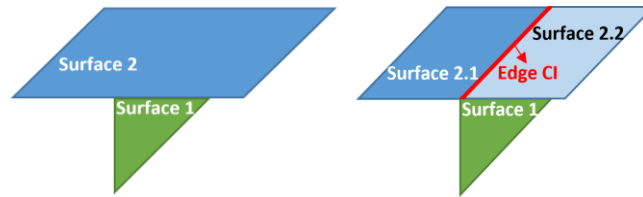


Figure 23: a. No CIC (left) & b. Edge CIC (right)

More information about how to define the conductance GL values for two nodes connected by a bolted joint, a spacer, a contact zone, the soldering of electronic components and electrical wiring is explained in chapter 6. There is no need to design those conductive interfaces as mentioned in the paragraph geometry. Therefore is an own Conductive Interface Calculator developed for the purpose of this thesis. The Conductive Interface Calculator makes it possible to calculate conductance values, which are needed to program the thermal design of a satellite within the ESATAN-TMS, more systematically. The second advantage of the Conductance Interface Calculator is that you as a thermal engineer have more control over the different input parameters. There are in literature for example tables available with numbers for contact conductance, but the material combinations mentioned are maybe not the ones you need for your design and there is also no indication for which surfaces roughness the values apply.

Another lesson learned concerning the TMM is about the node numbers of the meshes are changed. It is possible to define groups within ESATAN-TMS, which consist of different geometries. The four side faces of the QARMAN satellite are for example forming the group side panels. A group is defined by referring to the names of the geometries to that group. When the node numbering of a geometry is changed, even when the name of the geometry remained the same, the concerning group should be deleted and redefined. ESATAN-TMS will crash during the thermal simulation if the group isn't redefined when node numbers are changed for one of the geometries.

5.3 GMM

The Geometric Mathematical Model is a mathematical representation of the physical surfaces. Surface activities, like conductive, radiative, combination of conductive and radiative or non-active are defined during this GMM phase. Two different types of radiative cases are used for the thermal simulations of the QARMAN satellite, namely enclosure analysis and orbital analysis. A radiative case with environmental and orbital parameters is set to calculate the radiative couplings, direct and absorbed heat fluxes, view factors (VF) between the surfaces within the thermal design and radiative exchange factors. The enclosure analyses are used for the re-entry phase, where view factors are calculated for one geometrical orientation. For an enclosure analysis are temperature variations over time defined as boundary conditions for the outer surfaces of the satellite. The temperature profiles are the result of performed CFD analyses. There is also a possibility of entering a thermal flux profile over time instead of a temperature profile. The orbital analyses are used to simulate hot and cold conditions of the satellite model in an orbit around a planet.

The calculation of the heat fluxes, radiation exchange factors and view factors is performed by a Monte Carlo Ray Tracing Method (MCRT). The basis for this method is that a geometry is affected

by an infinite number of rays, where the ray-tracing procedure considers the individual history of the energy packets. The energy packets are emitted, reflected in many directions and finally absorbed by one point. But it is impossible to follow the energy packets of an infinite number of fired rays. Therefore are the radiative couplings and heat fluxes estimated by a finite number of fired rays. The MCRT method simulates a finite amount of rays and collect information about the emission points and emission directions. The rays are fired in random directions and therefore is the MCRT method a stochastic method, because ray and face interactions are randomly determined. Figure 24 shows that the evolution of the estimated values is within a band, where the width is inversely proportional to the square root of the number of fired rays. More rays fired means estimated values with a higher accuracy but means also a higher computer computation time. If the error e is reduced by fifty percent, the computer effort is quadrupled. The computer computation time increases also when the surfaces have a lower emissivity and absorptivity, because the rays are more reflected before they are finally absorbed by the material.

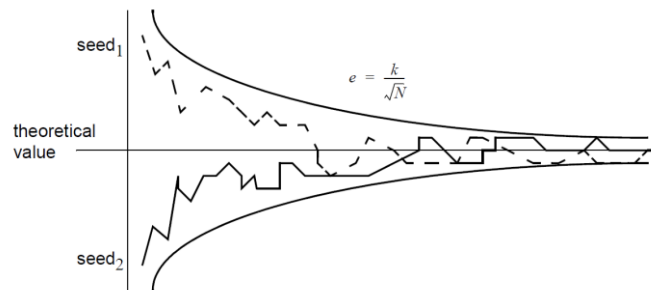


Figure 24: Evolution of MCRT estimations (e = error and N = number of rays)

The MCRT method is controlled by two numbers, namely the number of fired rays and the seed number (see figure 24). Both numbers can be set in the radiative execute ESATAN-TMS dialog. It is important to keep the seed number constant during the thermal design, because starting every simulation with the same seed produces the same sequence of pseudo-random initial distribution of rays orientation and therefore are the calculations repeatable. Different seed numbers lead to different results.

5.4 Simulation and Post processing

The SOLFM solver, namely a solver which is based on a matrix resolution method, is used for the enclosure simulations. The SLCRNC Crank-Nicholson forward-backward transient solver, which is a finite difference method, is used for the orbital simulations.

It is important to post-process the results after simulation. The first post-processing can be done within ESATAN-TMS by visualizing the temperatures of the subcomponents. Here it is important to check if there aren't any large temperature gradients between two neighbouring nodes. A second post processing can be done with the Thermal Analysis model Network Viewer (ThermNV) to make charts about the temperature profiles of the different components. The TMD files for the re-entry or the TMD2 files for the orbital cases are uploaded in ThermNV, a template layout file is generated with the different nodes of interest and reports can be generated.

6 Detailed design of conductor interfaces

This chapter explains how the contact conductances for different contact interfaces are calculated. The conductive interfaces covered in this chapter are: contact zones, bolted joints, spacers, soldering of electronic components and bundles of electrical harnessing. All the equations and calculations explained along this chapter are implemented in the Conductor Interface Calculator.

The Thermal Mathematical Model shows analogies with an electrical network as explained in chapter 5. The Ohm law and Kirchhoff's laws which apply for the electrical network, also apply for the thermal network by simply changing variables. The analogies between both networks was presented in table 4 in chapter 5. The thermal conductors are the TMM elements which are used to represent the thermal path through which energy is transferred from one to another node. There are three types of conductors according to the three types of heat transportation, see figure 25. The names of the different types of conductors, see red indications in figure 25, are the ones used in ESATAN-TMS.

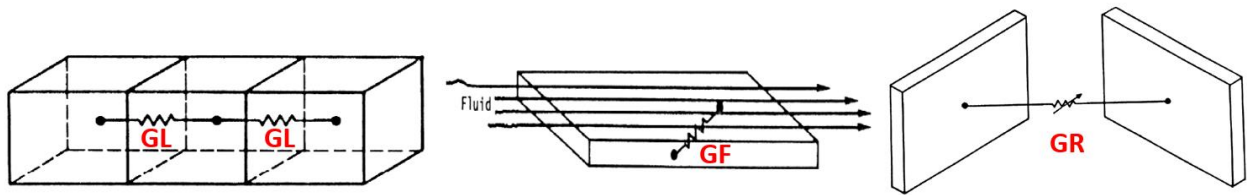


Figure 25: Three types of conductors

The first two conductors, namely GL and GF , are linear conductors. A linear conductor's heat flow is a function of the temperature difference of two nodes, where the temperature values are to the first power. The relation between the heat flow and the conduction conductor is given by equation 6.1.

$$\dot{Q} = GL_{(i,j)} \cdot (T_i - T_j) = \frac{k \cdot A}{L} \cdot (T_i - T_j) \quad (6.1)$$

With GL the linear heat transfer factor and T_i and T_j respectively the temperatures for node i and j . The conduction conductor is calculated by multiplying the thermal conductance k with the shape factor. The shape is defined by dividing the cross sectional area A through which the heat flows by the thermal path length L . The heat flows perpendicular through a plane with area A .

The relation between the heat flow and the convection conductor GF is given by equation 6.2. The heat of the fluid is assumed to enter an upstream node u at a temperature T_u and the heat leaves through a second node at temperature T_i .

$$\dot{Q} = GF_{(u,i)} \cdot (T_u - T_i) = w \cdot c_p \cdot (T_u - T_i) \quad (6.2)$$

Where w is the mass flow rate in the link and c_p is the specific heat capacity of the fluid.

The radiation conductor GR is a non-linear conductor, because the heat flow is a function of the temperature difference where the temperatures are at the fourth power. (see equation 6.3)

$$\dot{Q} = GR_{(i,j)} \cdot (T_i^4 - T_j^4) = \sigma \cdot GR_{(i,j)} \cdot (T_i^4 - T_j^4) = \sigma \cdot \epsilon_i \cdot \alpha_i \cdot A_i \cdot F_{ij} \cdot (T_i^4 - T_j^4) \quad (6.3)$$

The heat is emitted from plate i with a surface A_i and an emittance factor ϵ_i . The emitted heat is received by plate j and radiated back to plate i with an absorbance factor α_i . F_{ij} is the viewfactor.

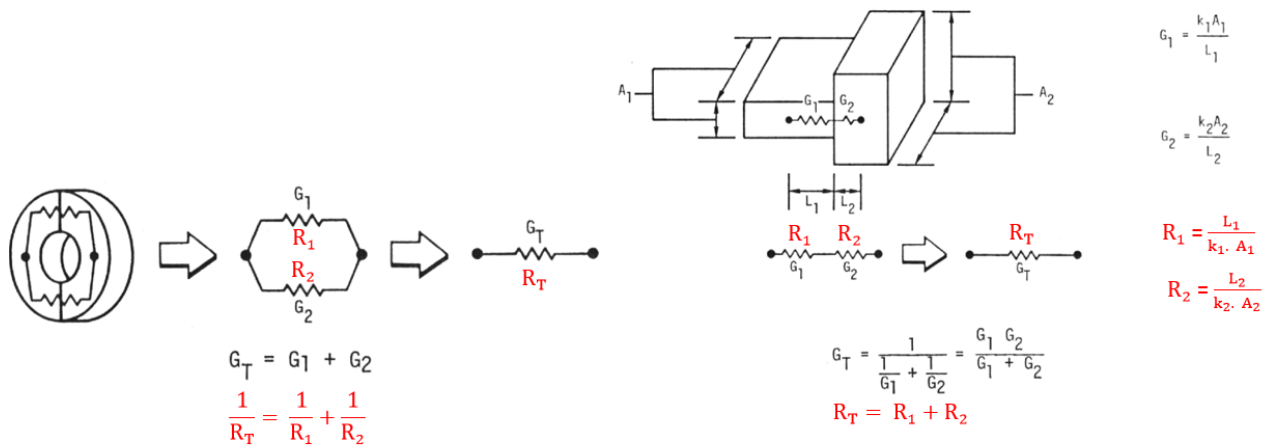


Figure 26: Thermal conductors (black) and thermal resistances (red) in parallel and series

Two or more conductors in series are combined to one conductor, where the inverse of the equivalent conductance is equal to the algebraic sum of the inverse individual conductance values. The equivalent value for two or more conductors in parallel is equal to the algebraic sum of the individual conductance values. Laws for electrical networks are also applicable for thermal networks, where equivalent conductance values are calculated by using the electrical series and parallel conductor equations. For thermal resistances are the same equations applicable as the ones used to calculate equivalent electrical resistances.

6.1 Contact zone

The thermal contact conductance h_c values are necessary to define the contact zones within ESATAN-TMS. The choice to elaborate out some more detailed calculations for the h_c values is based on the fact that within literature there are for example no tables available where the thermal engineer can look up h_c values for the contact between 2 different materials. There is also no indication given about the roughness of the materials. First, the different parameters are explained which influence the thermal contact resistance. A second part of this part 6.1 contact zone shows the two applicable methods to calculate the h_c values.

6.1.1 Parameters influencing contact resistance

The thermal contact resistance is a complex problem. This paragraph gives an overview of the different factors that affects the real contact area. Two solids in contact with each other have only

intimate contact at discrete points, called the asperities. The asperities form the thermal path for the heat flux.

The contact conductance is the actual algebraic sum of 3 heat conductors in series, namely:

- Conductance through contacting points,
- Radiation through gaps between both surfaces,
- Gas conduction through gas that fills the gaps.

For space applications are surfaces in contact with each other in a vacuum environment, therefore is the gas present in gaps negligible and is radiation in a vacuum environment neglected.

The factors influencing the thermal contact conductance are: applied joint pressure, surface roughness, surface flatness, surface hardness, E-modulus of the surface, thermal conductivity of the two plates in contact with each other and thermal interface material. A thermal interface material fills the natural gaps between the rough plates, whereby the contact area increases and the thermal contact conductance also increases. There are no thermal interface materials used for the QARMAN-TMS satellite, so the influence of the filler on the h_c values is not discussed in detail.

Contact pressure

One of the main factors which affects the contact conductance is the contact pressure. The asperities are microscopic peaks and valleys in the material surfaces. Asperities penetrate each other when the pressure between the two bodies increases and create a path where the heat flux can pass through the material. The ratio of the real contact area to the nominal contact area is usually much less than 2%. The following figure 27 shows more elastic and plastic deformation of the asperities when the contact pressure increases. If the contact pressure is so high that yield strength is exceeded, elastic deformation transits to a plastic deformation. A higher contact pressure means more deformation and a higher contact conductance.

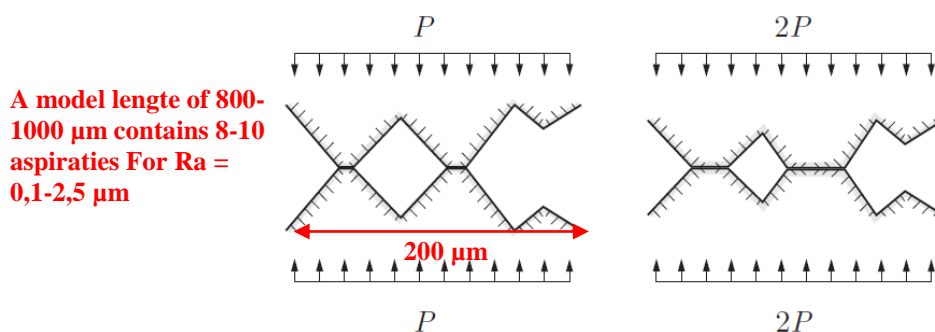


Figure 27: Effect of increased contact pressure

The contact pressure which can be selected in the conductive interface calculator are categorized in soft, medium and hard, where the contact pressure is respectively equal to 0,1 MPa, 5 MPa and 10 MPa. Those contact pressures are chosen because most of the tables in literature present contact

conductance values for those pressures. But the conductance interface calculator can also calculate with own defined contact pressures.

Surface roughness and flatness

Materials get rough after a cutting process, an extrusion process, a grinding process, a machining process,... Two rough surfaces have microcontacts. The mean plane separation Y and the amplitude of the asperities is reduced when the roughness decreases. This previous reduces the gap between both contacting plates and therefor increases the contact conductance. A lower roughness means also that a smaller fraction of the contact area constricts the heat flow.

Vibrations, gaps in machining equipment or heat treatments cause macrocontacts. A flatter surface increases the contact areas, which increases at his turn the contact conductance. Where FD is the Flatness Deviation in figure 28. FD is equal to the squared half chord length of a corrugated surface divided by the radius of the curvature.

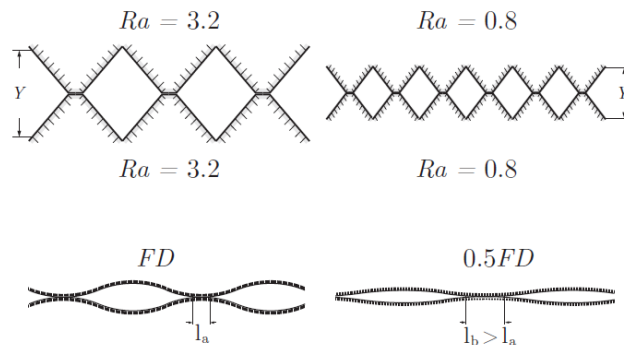


Figure 28: Effect of reduced surface roughness (Above) and flatter surface (Below)

A default value of $0,4 \mu\text{m}$ has been selected for the Conductive Interface Calculator, because most contacting interfaces of the QARMAN satellite have a finished surface. A roughness of $0,4 \mu\text{m}$ is an averaged roughness value for abrasive processed surfaces. Nevertheless can a user specify an own defined roughness value for the contact zone calculation into the Conductive Interface Calculator.

Surface hardness and E-modulus

A lower E-modulus means a softer material. Softer materials tent to deform more easily when the same compressive loads are applied on a harder surface. The asperities deform plastically against each other, which increase the contact surface and the contact conductance value.

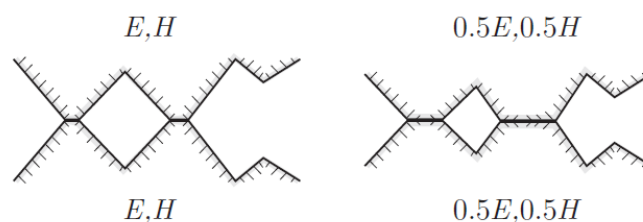


Figure 29: Influence of increased hardness and elasticity

Material conductivity

A higher material conductivity means that the heat flow through the contacting asperities flows more easily. Higher material conductivities increase the contact conductance.

The following sub-chapter explains the two different models used for the conductive interface calculator.

6.1.2 Contact conductance models

The contact resistance depends on the actual contact between the two solids and the radiation heat transfer across the open spaces in a vacuum environment. There deformation of the asperities can be either assumed elastic or plastic. The asperities have a Gaussian distribution over the apparent area. The following assumptions are made:

- Contacting solids are isotropic, which means that thermal conductivities and physical parameters are constant within the material,
- Contacting solids are thick in comparison with the roughness and waviness of their surfaces,
- No vibration effects are considered, only static contacts,
- Radiation is negligible,
- Heat flux through asperities is constant and not too large ($< 10^7$ W/m²)
- Contact for space applications is in vacuum.

Real surfaces are never perfectly smooth but have microscopic valleys and peaks. The real joint contact is characterized by several important factors [23]. The contact occurs at discrete parts of the contact area, namely microcontacts where peaks touch the underlying material. The heat transferred across the interfaces takes place by conduction through the real contacting areas and by radiation through the interstitial fluid. The heat transfer by radiation will be neglected, like mentioned before.

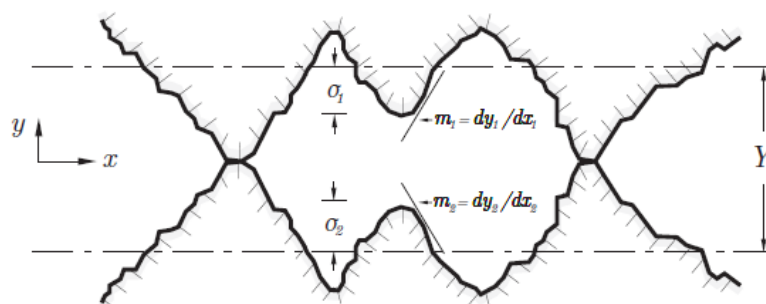


Figure 30: The root-mean-square roughness σ and the root-mean-square material asperity slope m of two contacting materials [23]

The thermal contact conductance h_c depends on the plates surface roughness, asperity slope and waviness geometrical parameters. The plastic contact conductance model of *Cooper, Mikic* and *Yovanovich* is used to calculate the thermal contact conductance. The presented model is based on 3 fundamental models: (1) the metrology model (surface roughness and asperity slope), (2) the contact mechanics model (deformation of the asperities of the softer material) and (3) the thermal

constriction resistance of the microcontact areas. The theoretical dimensionless contact conductance C_c can be expressed with following equation 6.4.

$$C_c = \frac{\sigma}{m} \frac{h_c}{k_s} \quad (6.4)$$

Where σ is the root-mean-square roughness (rms), defined as $\sigma = \sqrt{\sigma_1^2 + \sigma_2^2}$; m is the root-mean-square material asperity slope; defined as $m = \sqrt{m_1^2 + m_2^2}$, h_c is the thermal contact conductance and k_s is the harmonic mean thermal conductivity, defined as $k_s = \frac{2k_1k_2}{k_1+k_2}$.

The asperity slope m of different materials isn't commonly defined in literature, therefore a correlation equation proposed by *Antonetti et al.* (see equation 6.5) will be used for the calculation of m [23].

$$m = 0,125 \cdot (\sigma \cdot 10^6)^{0,402} \quad (6.5)$$

This equation 4.10 is developed for surface roughness ranging from 0,216 μm to 9,6 μm .

In literature several conforming rough surface models are presented, namely the elastic, plastic and elastoplastic contact models. This model differs from each other by the mode of the asperities deformation. The plastic contact model is used when the softer contacting asperities deform plastically, the elastic contact model is used when all contacting asperities deform elastically and the elastic-plastic model is used when the softer contacting asperities deform elastic-plastic. The elastic-plastic model isn't presented in this work, because some parameters have to be determined by experimental testing. This last means that the elastic-plastic model has no significant meaning for the general and practical applicable calculation of the thermal resistance of a bolted joint. Only the elastic and plastic contact models are presented in the following paragraphs.

Elastic contact model

The elastic contact model, proposed by *Mikic 1974*, for contacting rough surfaces is summarized below. This contact is predominantly elastic if the following ratio of $H_e/(E'm)$ is larger than 3.0 [19]. Here is H_e the elastic microhardness, E' the effective Young's modulus of the contacting asperities (see eqn. 6.6) and m asperity slope of the material (see eqn. 6.5).

The theoretical dimensionless contact conductance C_c can be calculated with *Mikic*, see proposed correlation 6.4.

$$C_c = 1,54 \cdot \left(\frac{P}{H_e}\right)^{0,95} \quad (6.6)$$

The ratio $\frac{P}{H_e}$ is the relative contact pressure, which can be easily calculated by *Sridhar and Yovanovich* expression (see equation 6.6). The contact pressure P and the elastic microhardness H_e of the softer material of the two surfaces. The elastic microhardness H_e depends on the material root-mean-square asperity slope m , the modulus of elasticity E and poisson's ratio ν .

$$H_e = C \cdot m \cdot E' \quad (6.7)$$

Where C is the constant 0,7071 ($= \frac{1}{\sqrt{2}}$) and E' (see eqn. 6.8) the effective Young's modulus of the contacting asperities.

$$\frac{1}{E'} = \frac{1 - \nu_1^2}{E_1} + \frac{1 - \nu_2^2}{E_2} \quad (6.8)$$

The contact conductance h_c is calculated by combining equation 6.4 and 6.6. These correlation equation has an uncertainty of about $\pm 2\%$ for relative contact pressures range $10^{-5} \leq \frac{P}{H_e} \leq 0.2$.

$$h_c = \frac{1,54 \cdot \left(\frac{P}{H_e}\right)^{0,95} \cdot m \cdot k_s}{\sigma} = \frac{1,54 \cdot \left(\frac{P \cdot \sqrt{2}}{E' \cdot m}\right)^{0,95} \cdot m \cdot k_s}{\sigma} \quad (6.9)$$

The elastic contact model is applicable for very hard surfaces of tool steel. A more general contact model which can be used for a wide range of surface roughness σ/m , a range of metal types (Ni200, SS304, Zr alloys, etc.) and a range of relative contact pressures $\frac{P}{H_p}$ is explained in the next section. [23]

The equation 6.9 is weakly influenced by the material root-mean-square asperity slope m . *Mikic* proposed a further simplification by stating that $m = 0,1$ [24], which is an average of the root-mean-square asperity slopes for blasted materials. This adapted equation 6.10 is presented below. In this new equation, only the contact pressure, RMS roughness and the effective Young's modulus of the contacting asperities must be known.

$$h_c = \frac{1,908 \cdot \left(\frac{P}{E'}\right)^{0,95} \cdot k_s}{\sigma} \quad (6.10)$$

Plastic contact model

The plastic contact model, proposed by *Cooper et al. 1969* and *Yovanovich 1982*, for contacting asperities is summarized below. The theoretical dimensionless contact conductance C_c can be calculated with the proposed correlation 6.11. The contact is predominantly plastic if the following ratio of $H_p/(E'm)$ is less than 0,33 [19]. Here is H_p is the plastic microhardness, E' the effective Young's modulus of the contacting asperities (see eqn. 6.8) and m asperity slope of the material (see eqn. 6.5).

$$C_c = 1,25 \cdot \left(\frac{P}{H_p}\right)^{0,95} \quad (6.11)$$

With the ratio P/H_p is the relative contact pressure. The contact pressure P and the microhardness H_p is converted from the Brinell hardness number BHN. The relative contact pressure P/H_p can be calculated with the explicit relationship presented in equation 6.12.

$$\frac{P}{H_p} = \left[\frac{P}{c_1 \left(1,62 \cdot \frac{\sigma}{m}\right)^{c_2}} \right]^{1/(1+0,071 \cdot c_2)} \quad (6.12)$$

With the coefficients c_1 and c_2 obtained from the Vickers microhardness tests. These Vickers microhardness correlation coefficients are related to the Brinell hardness test and can be calculated with the correlation equations 6.13, 6.14 and 6.15, developed by *Sridhar and Yovanovich 1996*.

$$c_1 = 3178 (4,0 - 5,77 \cdot H_B^* + 4,0 (H_B^*)^2 - 0,61 (H_B^*)^3) \quad (6.13)$$

$$c_2 = -0,370 + 0,442 \left(\frac{H_B}{c_1} \right) \quad (6.14)$$

$$\text{With } H_B^* = \frac{H_B}{3178} \quad (6.15)$$

With H_B the Brinell hardness expressed in MPa. The Brinell hardness is mostly expressed with a Brinell hardness number HBN in material properties charts. One unit HB is equal to a hardness of 1 kgf/mm² or 9,81 N/mm² (=9,81 Mpa). [25]

The contact conductance h_c is calculated by combining equation 6.4 and 6.11. These correlation equation has an uncertainty of about $\pm 1,5\%$ for the range $2 \leq \lambda \leq 4,75$.

$$h_c = \frac{1,25 \cdot \left(\frac{P}{HP} \right)^{0,95} \cdot m \cdot k_s}{\sigma} \quad (6.16)$$

The parameter λ is the relative mean plane separation, calculated with equation 6.17. The mean plane separation Y and the effective surface roughness σ are illustrated in figure 30.

$$\lambda = \frac{Y}{\sigma} = 0,2591 - 0,5446 \cdot \left(\ln \frac{P}{HP} \right) - 0,02320 \cdot \left(\ln \frac{P}{HP} \right)^2 - 0,0005308 \cdot \left(\ln \frac{P}{HP} \right)^3 \quad (6.17)$$

The models presented in order to calculate the contact conductance, presented in this sub-chapter, are also used for the calculation of the thermal network for bolted joints and spacers.

6.1.3 Validation of results

The results for two different cases are checked with literature [26].

Table 5: Contact conductance for representative Solid-Solid interfaces

Interface	Contact	Interfacial	h_c [W/m ² K]	h_c [W/m ² K]
	Pressure [MPa]	Fluid	Literature [26]	Calculated
Copper to copper	0,1	Vacuum	1000-10000	1368 (0,4 μ m)
Aluminium to aluminium	0,1	Vacuum	2000-6600	3892 (0,4 μ m)

The calculated values were calculated with the contact conductance calculator. It can be concluded that the results of the calculated contact conductances are within the limits of the contact conductance for comparable cases found in literature. The h_c values were calculated for a contact between two plates with a default roughness of 1,27 μ m, in literature was no roughness of the plates mentioned. So the contact conductance calculator has the advantage to calculate contact conductance for two different contacting materials, where in literature only the combination of two of the same materials are mentioned. A user can define its own materials, contact pressure or

material roughness. The value of the least rough material should be defined in the contact conductance calculator if two contacting materials have a different roughness, because the least rough materials has an dominant influence on the contact conductance value h_c . The contact conductance calculator is also able to select the correct model, namely plastic contact model or the elastic contact model, according to the following statements:

- The contact is predominantly plastic if the following ratio of $H_p/(E'm)$ is less than 0,33 [19]. Even, when $H_p/(E'm)$ is less than 1 is the plastic model selected, because there is elastoplastic deformation with predominantly plastic deformation. There is no clear transition between elastic of plastic deformation.
- The contact is predominantly elastic if the following ratio of $H_e/(E'm)$ is greater than 3.0 [19].

6.2 Bolted joint

The heat transfer inside the QARMAN satellite is comes from and goes to a various amount of different components, mostly driven by conduction and radiation heat transfer processes. This makes it even more difficult to calculate the thermal resistance of joint interfaces, because some analytical models make use of an approximated solution for a plate where the entire area is insulated except for one surface of the heat source and the interfacial contact. The analytical model, presented in this work, is based on a simplified QARMAN satellite bold (see figure 32). Figure 31 gives an overview of the parameters which influence the thermal contact of two plates jointed together, namely: geometrical, thermal and mechanical properties.

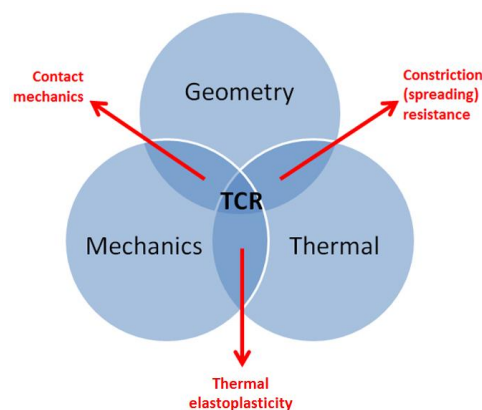


Figure 31: Thermal contact influenced by geometrical, thermal and mechanical properties

The geometry of two materials in contact is determined by the surface roughness, asperity slope, waviness, dimensions (surface and thickness) of a plate and gap thickness between both plates in contact. The mechanics of the contact is influenced by pressure which presses both plates together and deforms the asperities. This asperity deformation depends besides the contact pressure also on the material hardness of both plates. The thermal properties which influence the thermal contact resistance are thermal conductivities and the environmental temperatures which affect the physical properties of the materials. The relationships between the 3 properties, namely the constriction

resistance, the thermal elasto-plasticity and contact mechanics determine the total contact resistance between two materials in contact.

A bolted joint thermal resistance network depends on:

- The mechanical-geometrical relationship, which influences the contact conductance.
- The geometrical-thermal relationship, which influences the constriction (spreading) resistance.
- The geometry with surface and thickness dimensions, which influences the material resistance.
- The geometrical-thermal-mechanical relationship, which influences the contact resistances

6.2.1 Bolted joint resistance network [23]

It is very important to have a good knowledge of the resistance network and the different heat transfer mechanisms for the thermal control of electronic equipment and mountings for space applications. The bolted thermal resistance network is a complex network consisting of contact, material, constriction and radiation thermal resistances. In current literature, most of the correlation for the thermal resistance of a bolted joint network is based on contact resistance. In this work, a general approach for the calculations of the thermal resistance of a bolted joint will be explained, which could be easily adapted for other configurations, such as spacers. Bodies in low orbits interact only with a small number of atoms and molecules, there is a vacuum environment assumed and therefore is heat transfer by convection negligible. The radiation resistance is important for external surfaces which face sun or space. The radiation resistance is the ratio between the temperature difference between the two surfaces radiating to each other and the net transfer heat. The temperature differences between the bolt shaft and the core of the bolt or between the two plates in contact with each other is not large. The heat transferred by radiation is small in comparison with the heat transferred by conduction, therefore the radiation thermal resistances are neglected.

The heat resistance of a bolted joint has analogies with an electrical resistance network. The heat flow inside the satellite is conducted through the frame and mounting structures, namely plate 1 and 2 in figure 32. The bolt presented in figure 32 consists of a bolt head h , a bolt shaft b , a nut n , an upper plate P_1 and a lower plate P_2 . The resistances in the network of the bolted joint (see figure 33) are denoted $R_{C_{x,y}}$ for contact resistance between material x and y , R_{m_x} for material resistance of material x and R_{ct_x} for constriction resistance of material x . There are no washers considered in order to simplify the model.

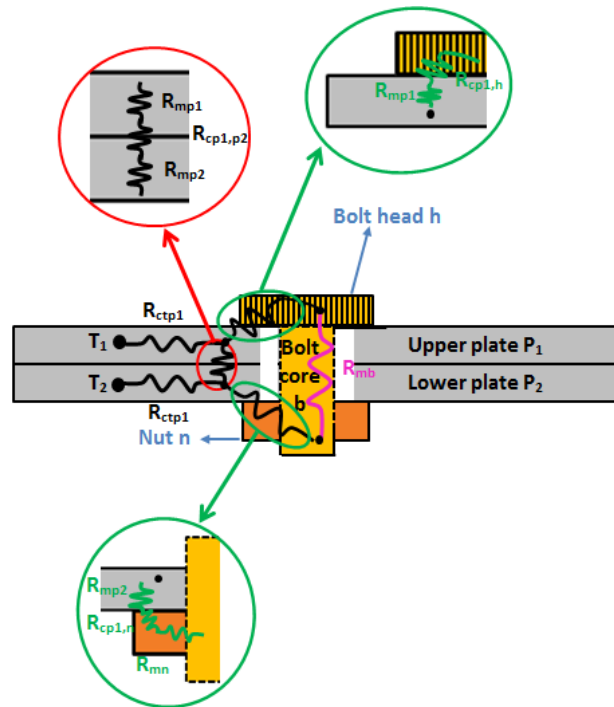


Figure 32: Typical satellite bolted joint with thermal resistance

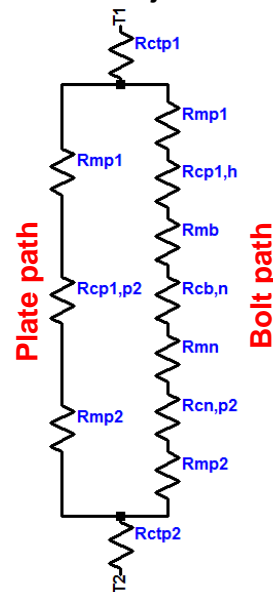


Figure 33: Complete thermal resistance circuit

The plate resistance network consists of the following resistances in series: upper plate material resistance R_{mp1} , contact resistance between the upper plate and the lower plate $R_{Cp1,p2}$ and the material resistance R_{mp2} . The bolt resistance network consists of the following resistances in series: upper plate material resistance R_{mp1} , contact resistance between the upper plate and the bolts head $R_{Cp1,b}$, the material resistance of the bolt R_{mb} , contact resistance between the bolt and the nut $R_{Cb,n}$, the material resistance of the nut R_{mn} , the contact resistance between the nut and the upper plate $R_{Cn,p2}$ and the material resistance R_{mp2} . The plate resistance network and the bolt resistance network are thermally connected in parallel and the equivalent parallel network resistance is in series with the constriction resistances of the upper R_{ctp1} and the lower plate constriction resistance R_{ctp2} . The total thermal network resistance of figure 33 is calculated with the following equation 6.18.

$$R_{tot} = R_{ctp1} + R_{ctp2} + \left[\frac{1}{R_{mp1} + R_{cp1,p2} + R_{mp2}} + \frac{1}{R_{mp1} + R_{cp1,h} + R_{mb} + R_{cb,n} + R_{mn} + R_{cn,p2} + R_{mp2}} \right]^{-1} \quad (6.18)$$

An example of the calculation of the thermal resistance of a bolted joint is given in Appendix B.

6.2.2 Contact resistance

The contact resistances between bolt and plate 1 denoted as $RC_{p1,h}$, between plate 2 and the nut $RC_{n,p2}$ and between both plates $R_{cp1,p2}$ depends:

- Pressure underneath the bolted head or nut,
- Material hardness,
- Thermal conductivity of the materials in contact,
- Roughness of the materials in contact,
- Modulus of elasticity of the contacting materials,
- Material asperity slope.

The pressure underneath the bolted head or the nut and between the plates is needed for the further calculations of the contact conductance. The contact conductance h_c indicates the ability of a bolted joint conducting heat between the two bolted plates.

Fontemot [27] observed the stress between the inside of a bolt head and plates can be considered uniform over the contact area. The pressure distribution underneath the bolted head and nut is considered to be uniformly distributed (see equation 6.19). Where the axial force, caused by the torque moment, is calculated with equation 6.20.

$$P = \frac{F}{\pi \cdot ((d_n/2)^2 - (D_H/2)^2)} \quad (6.19)$$

With D_H is the bearing surface inside diameter and d_n the pitch diameter of the bearing surface.

The standard torque T applied on the bolt can be translated to an axial tension F . This formula is applicable for bolt/nut assemblies with an ISO metric thread according to ISO 5855-1. [28]

$$F = \frac{T}{\left\{ \frac{d_2}{2} \left(\frac{\mu}{\cos \alpha} + \tan \beta \right) + \mu_n \cdot \frac{d_{n1}}{2} \right\}} \quad (6.20)$$

With d_2 is the pitch diameter, μ the friction coefficient of the bearing surface, μ_n the friction coefficient of the bearing portion, α the half angle of the screw thread, β the lead angle and d_{n1} the pitch diameter of the bearing surface (see figure 34).

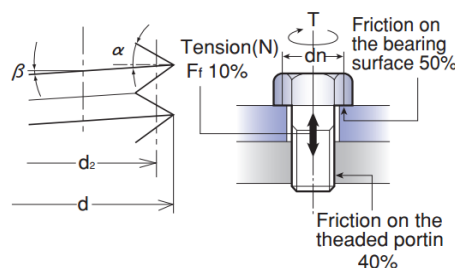


Figure 34: Detailed drawing for bolt dimensions used in eqn. 4.2 [29]

The pressure P distribution is considered to be uniform for the calculation of the h_c values. An uniformly distributed pressure can be easily calculated for the pressure between the plate and the bolts head or nut, because the contact surface is known. But what is the contact surface between both plates? The contact pressure between the two plates which are bolted together is calculated with the analytical model presented by *Fernlund*. The stress under the bolted head has a conical distribution (see figure 35) with a radius x , see equation 6.21. [30]

$$x = \frac{d_n}{2} + z \tan(\alpha) \quad (6.21)$$

With the outside radius of the stress zone, d_n the pitch diameter of the bearing surface, z the axial distance measured from the surface under the bolts head and α is the angle of the stress cone equal to 40° .

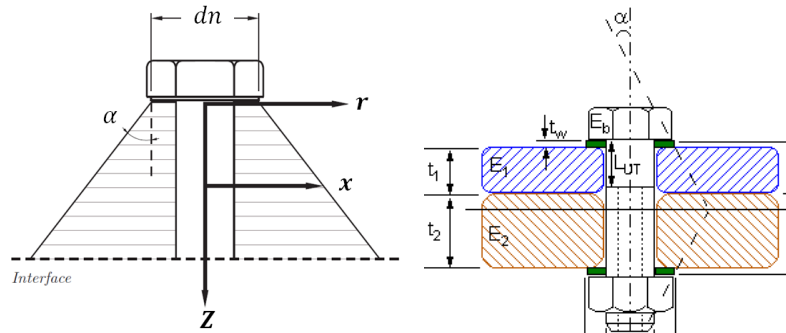


Figure 35: Conical pressure distribution between two bolted plates

The stress cone with radius x at the vertical position z equal to the plate thickness of the thinnest plate, determines the contact area between both plates. The maximum radius of the stress cone is situated about the midplane of the joint. The two stress cones with the same angle α are symmetrical about the midplane. Where P is the pressure between both plates at a vertical position z and a horizontal position r , see equation. 6.22. Outside the stress cone is the stress assumed to be zero.

$$P(r, z) = A \cdot r^4 + B \cdot r^3 + C \cdot r^2 + D \cdot r + E \quad (6.22)$$

The variables A , B , C , D and E are expressed in the following equations 6.23 to 6.27.

$$A(z) = \frac{\frac{15}{\pi} \left(\frac{z}{d_n}\right)^6 F}{-\left(\frac{2x}{d_n}\right)^6 + 2 \left(\frac{2x}{d_n}\right)^5 + 5 \left(\frac{2x}{d_n}\right)^4 - 20 \left(\frac{2x}{d_n}\right)^3 + 25 \left(\frac{2x}{d_n}\right)^2 - 14 \left(\frac{2x}{d_n}\right) + 3} \quad (6.23)$$

$$B(z) = -\frac{4}{3} \left(\frac{4x}{d_n} + 1\right) \frac{d_n}{2} A(z) \quad (6.24)$$

$$C(z) = \frac{4x}{d} \left(\frac{2x}{d_n} + 2\right) \left(\frac{d_n}{2}\right)^2 \quad (6.25)$$

$$D(z) = -2x^2 d_n A(z) \quad (6.26)$$

$$E(z) = -\frac{1}{3} \left(\frac{2x}{d_n}\right)^3 \left(\frac{2x}{d} - 4\right) \left(\frac{d_n}{2}\right)^4 A(z) \quad (6.27)$$

With F the axial force as calculated with equation 6.20.

The contact pressure between the two bolted plates is considered to be uniform for the following calculations of the contact conductance h_c . Figure 36 shows a graph with the pressure distribution, at the right side of the bolts shaft, between the two plates. The following input values were used to construct the graph, namely two plates with both a thickness of 2mm torqued together with the standard torque value for a M3 bolt. The blue graph shows with *Fernlunds* analytical method calculated pressure distribution. The surface underneath the blue graph is equal to the surface under the red graph that indicates a uniform pressure of 10,11 MPa. Uniform pressure values are used to calculate the contact conductance h_c . The calculation for the h_c contact conductance value is explained in more details in the previous chapter.

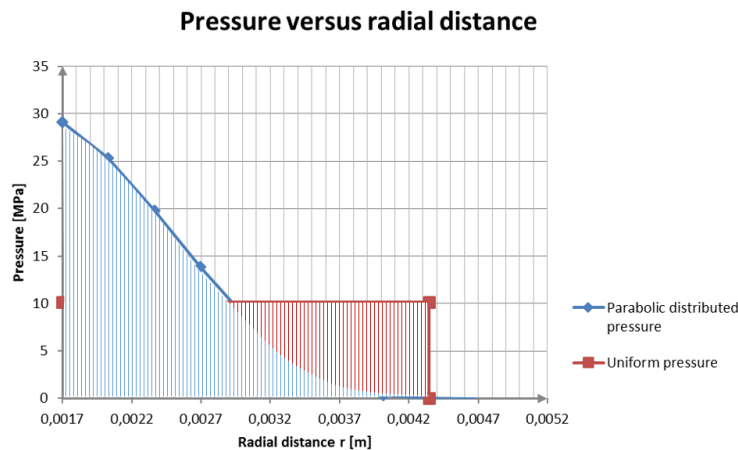


Figure 36: Parabolic and uniform under head pressure

The contact resistance can be calculated with the following equation 6.28.

$$R_c = \frac{1}{h_c \cdot S} \quad (6.28)$$

Where thermal contact conductance h_c (see following calculations) and S is the body contact surface. The calculation of the contact conductance is explained in sub-chapter “6.1 Contact zone”.

6.2.3 Material resistance

The material resistances are calculated by using the electrical-thermal analogy. In Fouriers law, equation 2.1, is the rate of conductive heat transfer through a material been presented as $\dot{Q} = -k \cdot S \cdot \frac{\partial T}{\partial x}$. There is a relationship between the material resistance and the heat transfer \dot{Q} , namely $\dot{Q} = dT/R_m$. Therefore a general equation 6.29 can be formulated for the material resistance.

$$R_m = \frac{L}{k \cdot S} \quad (6.29)$$

Where L is the body thickness, k the material thermal conductivity and S is the body surface.

6.2.4 Constriction resistance

The constriction of the heat flow spreading, occurs when the heat is forced through a very small area, the heat flux is constricted and the resistance is called constriction resistance R_{ct} . This spreading resistance occurs whenever heat leaves a heat source at temperature T_2 and enters into a larger region (see figure 37), the opposite is also true. When heat enters a finite region at a temperature T_1 , it also experience a restriction of the heat flow. This explains why there are 2 constriction resistances included in the thermal network of figure 33.

The heat is forced through the cross-sectional area of the plates. The incoming flux is supposed to be uniform, so the dimensionless spreading resistances for an isoflux rectangular area can be used for the calculation of R_{ct} (see table 6). The constriction resistance depends on the aspect ratio of the cross-sectional rectangular area, namely the ratio of the width a and the height h . The coordinate system is centralized.

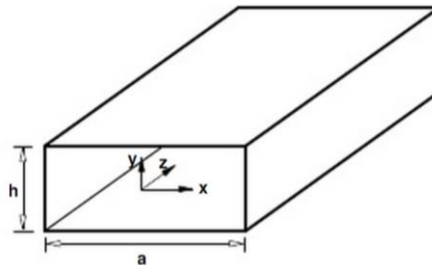


Figure 37: The aspect ratio of the cross-sectional area

Table 6: Dimensionless spreading resistance of an isoflux rectangular area

Parameter a/h	$k \cdot \sqrt{A} \cdot R_{ct}$	Parameter a/h	$k \cdot \sqrt{A} \cdot R_{ct}$
1	0,4732	6	0,3950
2	0,4598	7	0,3833
3	0,4407	8	0,3729
4	0,4234	9	0,3636
5	0,4082	10	0,3552

With k the thermal conductivity of the plates material and A the cross-sectional area.

Figure 38 shows a fitted curve trough the points given above. The regression curve shows an non-linear regression, which means that intermediate results of the parameter a/h can't be found by interpolating the values for $k \cdot \sqrt{A} \cdot R_{ct}$. There is a polynomial regression which describes the relation between the values for $k \cdot \sqrt{A} \cdot R_{ct}$ and $\frac{a}{h}$.

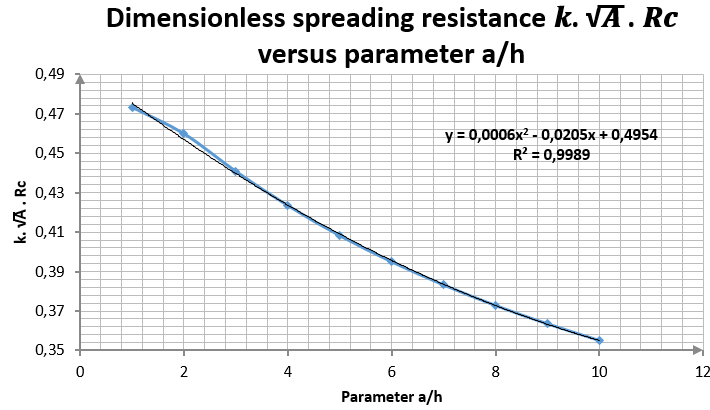


Figure 38: Fitted curve through graph dimensionless spreading resistance vs. parameter a/h

Based on the results of the curve fitting is the following equation 6.30 used to calculate the restriction resistance R_{ct} . The squared multiple correlation coefficient R^2 is equal to 0,9989. This means that 99,89 % of the total variation of the response $k \cdot \sqrt{A} \cdot R_{ct}$ is explained by the fitted model.

$$R_{ct} = \frac{0,0006 \cdot \left(\frac{a}{h}\right)^2 - 0,0205 \cdot \left(\frac{a}{h}\right) + 0,4954}{k \cdot \sqrt{A}} \quad (6.30)$$

Where a is equal to the dimension of the external plate diameter. The external plated diameter is calculated by multiplying the stress cone radius x at the vertical position z by 2, with z equal to the plate thickness (see figure 35). The height h is equal to the plate thickness. The area A is defined by multiplying the dimensions h and a .

6.2.5 Simplified thermal resistance for bolted joints [27]

Yovanovich and Mantelli developed a parametric study to find the major parameters which influence the thermal resistance of a bolted joint, in order to simplify the thermal resistance network presented in figure 33. For a bolted joint, without washers between both plates, only a total constriction resistance affects the heat flow through a bolted joint. This total constriction resistance includes the material resistance of the plates and contact resistance between the plates.

The total constriction resistance for bolted joints, by *Mantelli and Yovanovich*, is presented below (equation 6.31).

$$R_{ct} = \frac{1}{2 \cdot \pi \cdot k_p \cdot L_p} \left[\ln \left(\frac{c}{b} \right) - \frac{3}{4} + \Phi \right] \quad (6.31)$$

Where k_p is the thermal conductivity of the plate material, L_p is the plate thickness, c is the external plate radius, b is the external bolt radius ($d_{n1}/2$), a is the internal plate radius ($d_h/2$) and the non-dimensional contact parameter Φ is given by equation 6.32.

$$\Phi = \frac{\frac{K_0(\lambda)}{K_1(\lambda \cdot \frac{a}{b})} + \frac{I_0(\lambda)}{I_1(\lambda \cdot \frac{a}{b})}}{\lambda \left[\frac{I_1(\lambda)}{I_1(\lambda \cdot \frac{a}{b})} - \frac{K_1(\lambda)}{K_1(\lambda \cdot \frac{a}{b})} \right]} \quad (6.32)$$

Where $K_{0,1}$ and $I_{0,1}$ are Bessel functions from the 1st and 2nd order, D_H is the bearing surface inside diameter and λ is the Φ parameter argument (see equation 6.33).

$$\lambda = \sqrt{\frac{h_c \cdot b^2}{k_p \cdot L_p}} \quad (6.33)$$

Where h_c is the thermal contact conductance, b is the external bolt radius, L_p is the plate thickness and k_p is the thermal conductivity of the plate material.

This simplified thermal resistance model for bolted joints is only applicable for 2 plates with an equal thickness L_p bolted together. The *Mantelli and Yovanovich model* is compared with the thermal resistance model. From calculations, see Appendix B, it can be seen that the comparison between both models is excellent (around 13 %), especially if the thermal resistance model considers the system of heat transfer through bolted joints in all its complexity. This thermal resistance network model for bolted joints will be further adapted for the calculation of spacer connections, because the same logic to construct a thermal network for spacers can be applied.

6.3 Spacer

The spacer thermal resistance network is comparable with the thermal resistance network of a bolted joint, but then less complex. There is a contact resistance with the spacers head and plate one $R_{Cp1,s}$ and $R_{Cp2,s}$ between plate 2 at the bottom of the spacer. The material of the spacer forms a material resistance $R_{m,spacer}$ for the heat flow conducted through the spacer. The resistances $R_{Cp1,s}$, $R_{Cp2,s}$ and $R_{m,spacer}$ are in series and form the thermal resistance network of a spacer (see figure 39).

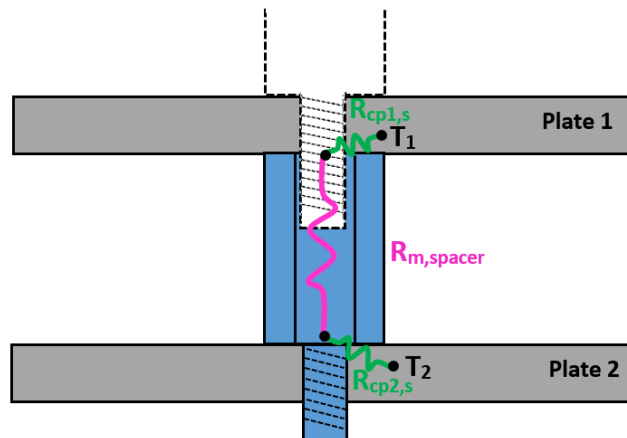


Figure 39: Thermal resistance network of a spacer

Spacers or standoffs are commonly used for stacking the PCB's. The spacers used for the QARMAN satellite are screw mounted versions. These supports are available in a wide range of different heights with metric thread dimensions.

The pressure under the spacers head is calculated with *Ferlund's* analytical method (see equation 6.21 to 6.27). This analytical method is originally been developed to calculate pressure distributions in a bolted joint, but is also applicable for spacers. Spacers are also a sort of bolts, were the thickness of the "head" is equal to the spacers length. The pressure distribution is calculated for a vertical z position equal to zero (see figure 35). This calculated pressure distribution is converted to a uniform pressure distribution, which is applied on the contacting

surface between the plates and the spacer. The contact conductance value h_c is needed to calculate the thermal contact resistance with equations presented in the sub-chapter “6.1 Contact zone”. PCBs have etched copper washers where the spacers are in contact with the PCB (see figure 50). Therefore is a hardness Brinell number of 78 of the softer material copper used for the contact conductance calculations. Asperities of the spacer penetrate the copper material on the PCB and create a path where the heat flux can pass through the material. The softest material deforms more. Where the deformed copper asperities increase the heat conductance.

The material resistance is calculated by dividing the length of the thermal path by the product of the spacer’s material conductivity and the surface perpendicular to the direction of the heat flux.

6.4 Soldering electronic component

The calculations for the thermal resistance of the conductive interface between an electronic component and the PCB is based on the design of a “medium power” component. Medium power components have exposed pad packages, where the IC die is sitting on a copper pad. Today are the ICs with the surface mounted power pads become one integral part for heat removing. The copper pad is soldered to the PCB and is also in contact with via holes into the PCB. The pins of the electronic component are placed in the copper plated via holes in order to connect the electronic component with the inner copper layers of the PCB, where the PCB acts as a spreading plane for the heat flux. This plane conducts the heat from a smaller area to a larger area in the PCB. It has to be remarked that every PCB and IC is constructed different, so also their thermal networks, where the task of deriving the thermal network of all those different PCBs and ICs is beyond the task of this thesis. However, a general thermal network of resistances will be proposed.

The component’s dissipated heat is spread out of the contact area by conduction, where a good thermal path demands a low thermal resistance. A low thermal resistance means that there will be a small temperature rise per watt dissipated heat. The following figure 40 shows a higher local temperature of the component in comparison with the surrounding materials, where the vertical axis shows the temperatures of a point with an x- and y-coordinate. For case 1 and case 2 are the heat flux respectively equal to 0,0016 W/mm² and 0,01 W/mm². The heat fluxes are chosen in such a way that the total heat flow equals to 1W for both cases with a different heat source size. In the first case, the properties of the heat sink are: 125×125 mm, t= 3mm and Al6061 with a heat source placed in the middle of the heat sink with an area of 25×25 mm. In case 2, the properties of the heat sink are the same as the ones mentioned for case 1, but with a smaller heat source placed in the middle of the heat sink with an area of 10×10 mm. The presented SiemensNX simulation results of figure 40 indicates clearly that the centre temperature increases when the heat source becomes smaller. The temperature at the edges decreases when the centre temperature rises. In literature are spreading resistances for the heat flow from an electronic component to a heat sink described. Those described spreading resistances are only applicable for electronics applied on ground for conventional air-cooled heat sinks. In space applications is the dissipated heat of the electronics only rejected and spread by means of conductions. The heat sink forms a thermal mass that delays the heating of the PCB. There is no pressurized air available in space, so no dissipating

pins can be used to reject the heat by convection. So there is no extra spreading resistance, which could act as a correction factor, added after the junction at temperature T_2 in the thermal resistance network shown in figure 41. The spreading of the dissipated heat is restricted by the material resistance of the surrounding materials, which is automatically taken in account when the material and thermal properties of the surface or the multi-layered surface is defined within ESATAN-TMS. Following proposed thermal network is used to calculate the total thermal resistance between the heat dissipating component and the node within the PCB to which the component is connected.

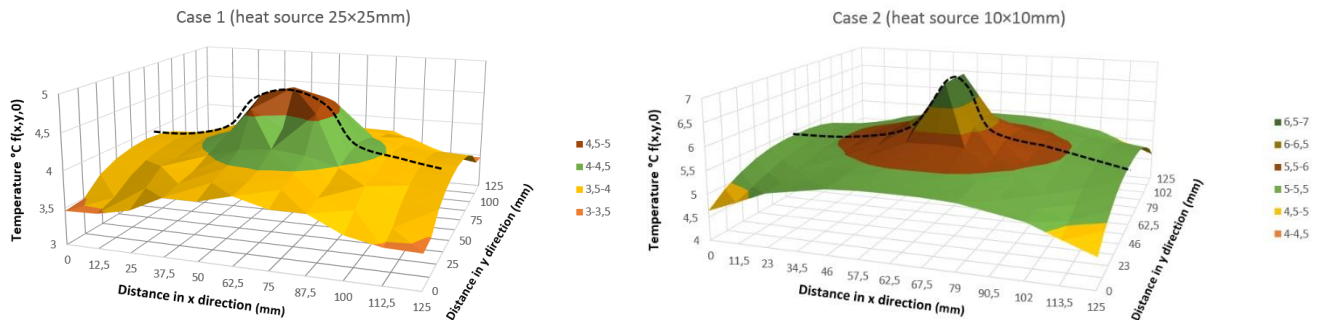


Figure 40: Temperature distribution in a flat heat sink (no fins) for different heat source areas

Following paragraphs present the thermal model which is used within the conductive interface calculator. Heat flow flows from one point at temperature T_1 to another point at temperature T_2 through different materials, where the different materials form material resistances for the conducted heat. The thermal resistance network, presented in figure 41, consists of the following thermal resistances in series and parallel:

- Thermal resistance of the copper pad of the components package R_{Cu} ,
- Thermal resistance of the soldering R_{PbSn} ,
- Thermal resistance of the copper plated via holes R_{viaCu} ,
- Thermal resistance of the soldering filling the via holes $R_{viaSnPb}$,
- Thermal resistance of the PCB R_{PCB} .

Figure 41 shows an electronic component with one via hole, but in an actual circuit are there multiple via holes. Nevertheless are the numbers of vias taken in account for the following calculations.

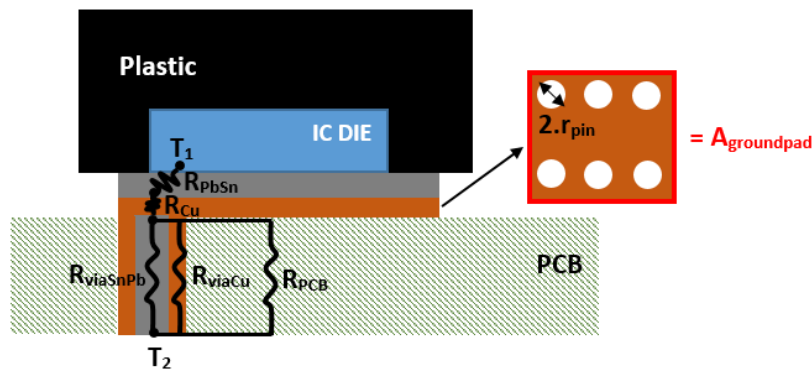


Figure 41: Electronic component thermal resistance network

Constriction resistances are not included in the thermal resistance network of contact interface between the electronic component and the PCB. However, those constriction resistance are present in real electronic packaging. Figure 42 shows typical locations where constriction takes place in the mounted electronic component on a heat sink, namely: across solder, through thermal vias and from the IC die to the PCB and heat sink. Those 3 previous mentioned constriction resistances are in parallel with their associated material resistances, for example the constriction resistance of the heat flux through the vias is in parallel with the vias material resistances R_{viaCu} and $R_{viaSnPb}$. *Naraghi and Antonetti* computed constriction resistances of single heat sources with various shapes, see figure 43. It can be concluded from this graph that at low area ratios the constriction resistance R_c increases to infinite. Therefore are constriction resistances neglected in the thermal network of figure 41, because the heat flow is constricted from the small source area A_s to the larger sink area A_p . A high constriction resistance value R_c has an insignificant effect on the total resistance of a parallel network consisting of a low material resistance and a high constriction resistance.

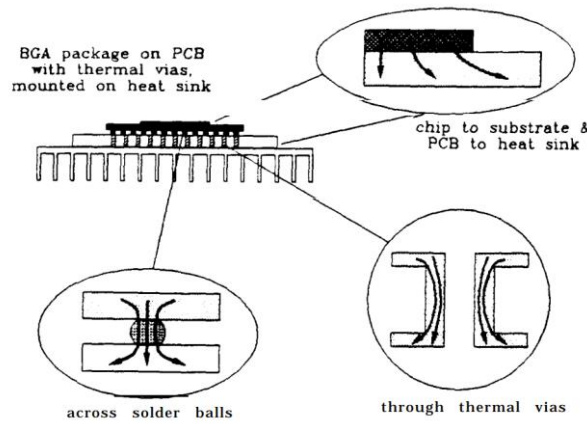


Figure 42: Constriction resistance in electronics packaging [31]

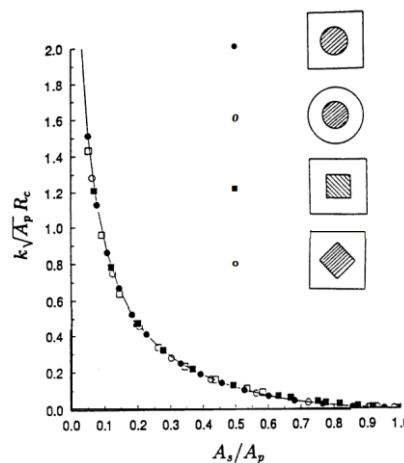


Figure 43: Dimensionless constriction resistance versus dimensionless source area A_s [31]

The total thermal resistance of the network presented in figure 41 is given by equation 6.34.

$$R_{tot} = R_{Cu} + R_{PbSn} + \left[\frac{1}{R_{viaCu}} + \frac{1}{R_{viaSnPb}} + \frac{1}{R_{PCB}} \right]^{-1} \quad (6.34)$$

Typical dimensions for the thickness of the solder joint, diameter of IC's pins, thickness of the copper pad, etc. found in literature [32] are also mentioned throughout the following explanation.

The soldering used for space applications are lead-tin PbSn solders with a minimum of 3% lead alloy. Lead-free solder alloys (<Pb03) shall not be used for the manufacturing of spaceflight hardware [33]. Therefore are the solder resistance specifically indicated index PbSn. Equation 6.35 shows the calculation for material resistance of the solder layer between the copper pad and the IC die.

$$R_{PbSn} = \frac{t_{solder-layer}}{A_{groundpad} \cdot k_{PbSn}} \quad (6.35)$$

Where the thickness of the solder joint $t_{solder-layer}$ is approximately 0,508μm.

The copper pad forms a material resistance R_{Cu} (see equation 6.34).

$$R_{Cu} = \frac{t_{Cu-layer}}{A_{Cu} \cdot k_{Cu}} = \frac{t_{Cu-layer}}{(A_{groundpad} - \frac{1}{4} \cdot \#pins \cdot d_{pins}^2 \cdot \pi) \cdot k_{Cu}} \quad (6.36)$$

With a typical 35,6μm thickness of the copper pad $t_{Cu-layer}$ and the area of the copper pad is equal to the outer copper pad dimension $A_{groundpad}$ subtracted by the total area of removed copper ($\#pins \cdot r_{pins}^2 \cdot \pi$) where the pins are sticking through the PCB (see Figure 41), with $\#pins$ the total number of pins with a typical diameter d_{pins} of 305 μm.

The material resistance caused by the copper plating in the via holes (see eqn. 6.37) depends on the mantle area A_{viaCu} , thermal conductivity k_{Cu} and the length of the via. The length of the via is equal to the PCB thickness t_{PCB} .

$$R_{viaCu} = \frac{t_{PCB}}{A_{viaCu} \cdot k_{Cu} \cdot \#pin} = \frac{t_{PCB}}{(r_o^2 - r_i^2) \cdot \pi \cdot k_{Cu} \cdot \#pin} \quad (6.37)$$

Outer radius r_o and inner radius r_i have respectively 152 μm and 135 μm as typical dimensions. The length of the via is equal to the board thickness t_{PCB} . Since there are total number of pins ($= \#pin$) placed in parallel, the material resistance for one solder filled via is divided by $\#pin$.

This following equation 6.38 gives the thermal resistance of the solder filled vias.

$$R_{viaPbSn} = \frac{t_{PCB}}{A_{viaPbSn} \cdot k_{PbSn} \cdot \#pins} = \frac{t_{PCB}}{r_i^2 \cdot \pi \cdot k_{PbSn} \cdot \#pins} \quad (6.38)$$

Again, since there are a total number of pins ($= \#pin$) placed in parallel is the material resistance for one solder filled via divided by the number of pins.

The material resistance of the PCB board is calculated for the PCB material under the groundpad. This can be explained as following. The conductive interface calculation is done to know the thermal resistance between two nodes, namely a thermal node with the properties of the studied electronic component and a node within the meshed PCB to which the thermal node is connected. The different nodes in the meshed PCB have reciprocally also thermal resistances, but these

resistances are calculated automatically after defining the thickness, the dimension and the thermal conductivity of the PCB within ESATAN-TMS. Therefore applies this material calculation of the PCB only for the PCB material under the copper groundpad. The PCB thermal properties are assumed to be isotropic and are obtained assuming that the PCB consists of two 35 μ m thick Cu-layers 100% filled and 4 Cu-layers 20% filled. The materials of the PCB itself have the following approximate composition: Glass-reinforced polymer standard FR4 material 70 % , Copper 16 % , Solder 5 % , Iron, ferrite 5 % , Nickel 1 % , Silver 0.1 % , Gold 0.025 % , Palladium 0.01 % and other (bismuth, antimony, tantalum, etc.). An averaged material thermal conductivity value of 0,25 W/mK is for the PCB laminate. A same approach as the previous mentioned equations is used to calculate R_{PCB} (see equation 6.39).

$$R_{PCB} = \frac{t_{PCB}}{A_{groundpad} \cdot k_{PCB}} \quad (6.39)$$

All the calculations 6.35 to 6.39 are merged in equation 6.34 in order to calculate the thermal resistance of the electronics component solder joint. The area of the groundpad, the number of pins and the length of via are chosen to be input parameters for the conductive interface calculator. It can be concluded that a larger groundpad, a higher number of pins and a thinner PCB board decreases the thermal resistance of the solder joint of an electronic component. A larger groundpad increases the cross-sectional area for thermal heat conduction, which means a cooler IC. More pins means that heat is better spread. A thinner PCB, means a shorter thermal path and also increases the total thermal resistance of the joint between the IC and the PCB.

6.5 Electrical wiring

The electrical harnessing of the satellite consists of bundles of different types of wires. A total conductance GL-value can be calculated with the Conductive Interface Calculator for a bundle consisting of 2 different sorts of cables and 1 sort of coaxial cable, which is sufficient to determine the conductive interface between 2 points connected by electrical harnessing in the QARMAN satellite.

The thermal resistance calculation for a coax cable is based on the Fourier's law of heat conduction (see equation 6.40). Consider the cylinder A in figure 44 with a thickness $dr (= r_2 - r_1)$ at a distance r_1 from the centre of a coax cable with a length L . The mantle area of a cylinder is equal to $A = 2\pi rL$.

$$\dot{Q} = -k_A \cdot (2\pi rL) \cdot \frac{dT}{dr} \quad (6.40)$$

$$\Leftrightarrow \int_{r_1}^{r_2} \frac{\dot{Q}}{k_A \cdot (2\pi L)} \cdot \frac{dr}{r} = - \int_{T_1}^{T_2} dT$$

$$\Leftrightarrow \frac{\dot{Q}}{k_A \cdot (2\pi L)} \cdot \ln\left(\frac{r_2}{r_1}\right) = (T_1 - T_2)$$

$$\Leftrightarrow R_A = \frac{\Delta T}{\dot{Q}} = \frac{1}{2 \cdot \pi \cdot L \cdot k_A} \cdot \ln\left(\frac{r_2}{r_1}\right) \quad (6.41)$$

This above presented equation is applicable for the cylinder A with an inner radius r_1 , an outer radius r_2 and a material conductivity k_A . Equation 6.41 can also be adapted for cylinders B and C

of figure 44. The thermal resistance of the core of the coax cable is calculated by applying the general formula $L/k.A$ for a material resistance. Equation 6.42 shows the total resistance of a coax cable consisting of the following series resistance (in this order): centre conductor, inner dielectric, braided shields and jacket. There is no optional metallic foil between the inner dielectric and braided shield considered for the Conductor Interface Calculator calculation for the thermal network of a coax cable.

$$R_{tot} = \frac{L}{k \cdot \pi \cdot r_1^2} + \frac{1}{2 \cdot \pi \cdot L \cdot k_A} \cdot \ln\left(\frac{r_2}{r_1}\right) + \frac{1}{2 \cdot \pi \cdot L \cdot k_B} \cdot \ln\left(\frac{r_3}{r_2}\right) + \frac{1}{2 \cdot \pi \cdot L \cdot k_C} \cdot \ln\left(\frac{r_4}{r_3}\right) \quad (6.42)$$

Where a copper tinned braid matrix has a thermal conductivity k_B equal to 67 W/mK [34].

The total resistance of a wire can also be calculated with the same principle of equation 6.42, but only the first 2 terms remain. The thermal resistance of a bundle of different types of cables is calculated by calculating the equivalent resistance for the different parallel cable resistance. The inverse of the equivalent resistance is equal to the algebraic sum of the inverse individual cable resistance values.

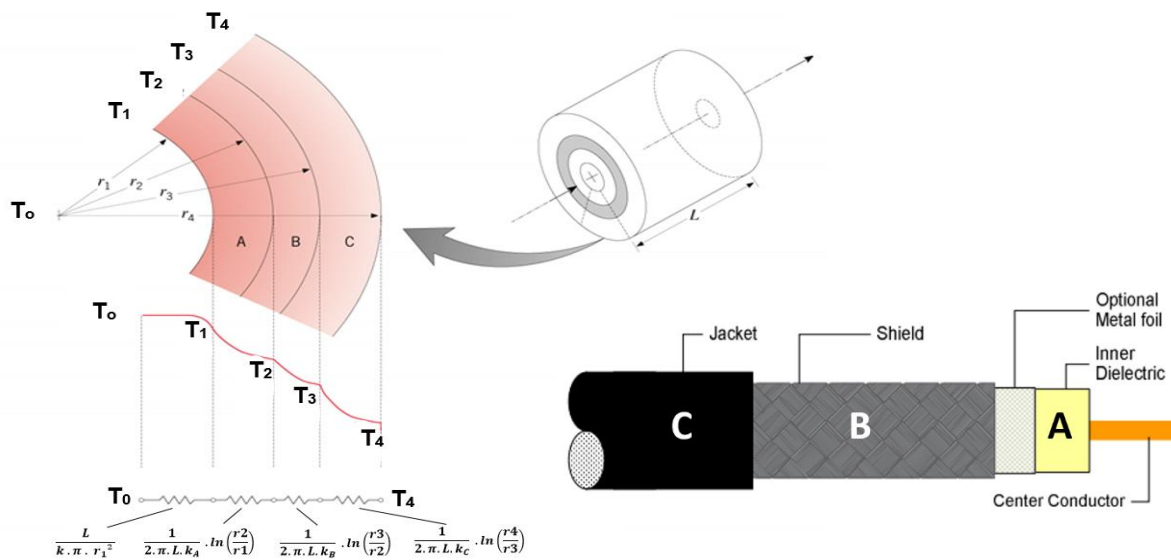


Figure 44: Coax cable thermal resistance network

7 QARMAN's thermal design

The European Space Agency Thermal Analysis Network-Thermal Modelling Suite (ESATAN-TMS) is the standard software used for the thermal analysis of the QARMAN satellite. The QARMAN satellite consists of passive thermal control systems in order to maintain the temperature of the satellite's components within their temperature margins throughout the entire mission. The thermal design was driven by these temperature limits. Figure 45 shows a previous concept of the QARMAN satellite. As it can be seen from figure 45, there are many PCB's stacked on top of each other, the concept of a survival unit was not yet been used,... Throughout this thesis has the thermal design of the QARMAN satellite been developed, according to findings or design changes. This chapter gives an overview of the current state of the thermal design of the QARMAN satellite. The following paragraphs are the different steps, in chronological order, which are needed to perform a thermal analysis, namely: the thermal model and the post processed simulation data.

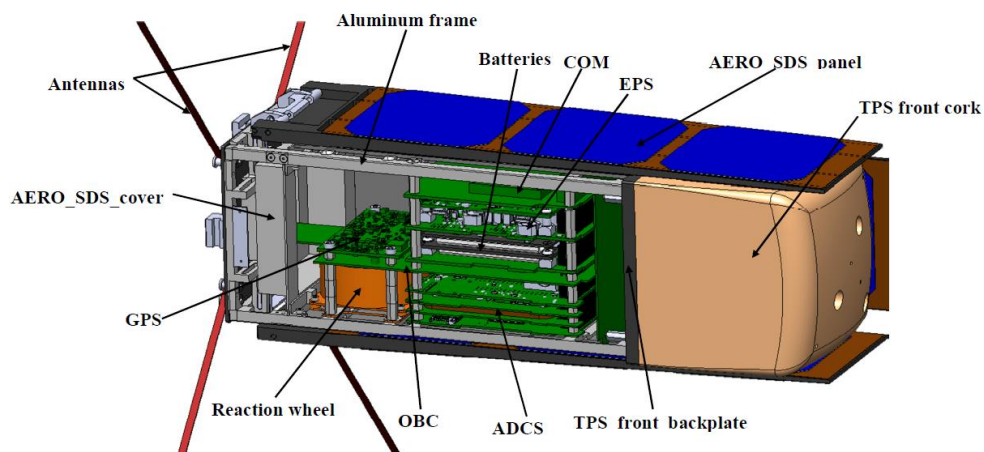


Figure 45: Previous concept QARMAN stowed configuration and internal parts view

7.1 ESATAN-TMS model description

The GMM (Geometrical mathematical model) defines the geometry of the QARMAN satellite. This mathematical model is used for the calculation of the following parameters, namely: the radiative couplings between the surfaces in the model, the conductive couplings between different components and the heat rates of each surface exposed to the external heat fluxes coming from the solar, earth IR and albedo radiation [19].

The entire QARMAN satellite has been modelled, using the ESATAN-TMS software. The external geometry consists of a 3-unit cubesat with four deployable solar cell panels. Therefore are the thermal simulations performed for two different satellite configurations, namely with the solar panels in a stowed and a deployed configuration. The internal components and structures have various complex forms, therefore have some approximations been made during modelling.

The thermal model is built in such a way that the geometrical, thermal and structural properties of the QARMAN satellite are represented in a realistic way.

Each defined geometry is divided in several nodes. The numbers of the nodes are manually defined, which is carefully done to prevent overlapping node numbers. Two components with the same node number behave thermally in the same way, although they are made from different materials, exposed to different heat fluxes... The defined thermal nodes are used for the lumped parameter method, which is used in the thermal mathematical model to calculate the different temperature profiles of the different components.

The density, specific heat and conductivity of bulk materials and the thermo-optical parameters of foils, such as IR emissivity and solar absorptivity, are defined to characterize different materials. There is a possibility to define the activity of the inner and outer surfaces of different components. The activity of the components can only be a combination of radiative and conductive (non)-active or only conductive (non)-active.

Some more detailed information about the current thermal design for the QARMAN satellite is given in the following paragraphs. The current QARMAN design is shown in figure 46 underneath.

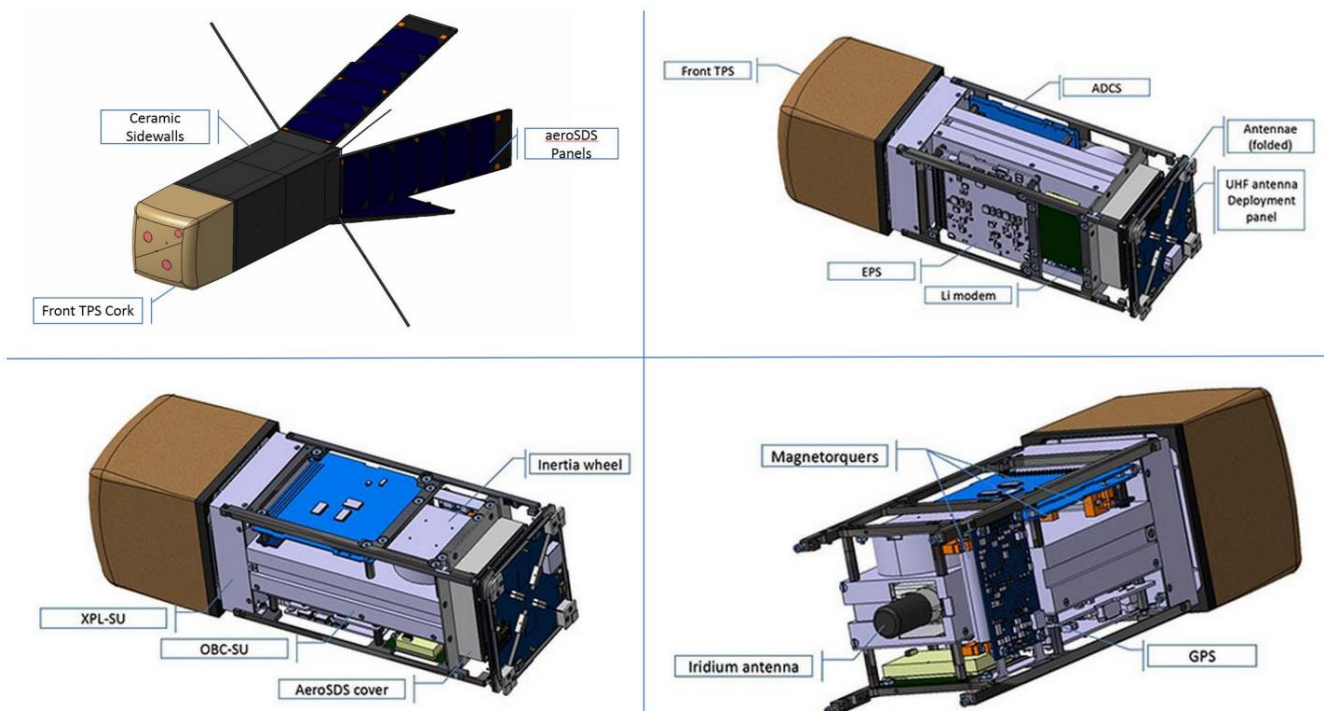


Figure 46: Current QARMAN satellite concept [35]

7.1.1 External geometry

The outer walls of the satellite consist of a composition of a 2 mm thick silicon carbide layer and a fiberfrax layer of 3 mm thickness. This outer wall can be seen as a reradiative wall, because a portion of the absorbed heat is disposed again by reradiation. For the reradiation is a surface with

a high emissivity and a low thermal conductivity needed. If the surface tolerates to work at high environmental temperatures close by the radiation equilibrium, the surface's temperature increases due to the high emissive surface and therefore increases the reradiation. The silicon carbide layer and the fiberfrax forms the thermal protection system for the sidepanels. An advantage of the SiC-surface is that the SiC is resistant against the atomic oxygen erosion, because there is a silicate-type (glass-like) protective layer formed during an atomic oxygen-attack [19]. The atomic oxygen exists in the LEO space environment and forms a reactive chemical because there is an unpaired electron in the valence shell of the atom. The fiberfrax is a ceramic paper which forms the insulation layer of the TPS for the sidepanels. The outer satellite TPS panels are conductive insulated from the satellites titanium frame. This assumption is realistic since the walls are only clamped by 4 M2.5 screws [20], see figure 47.

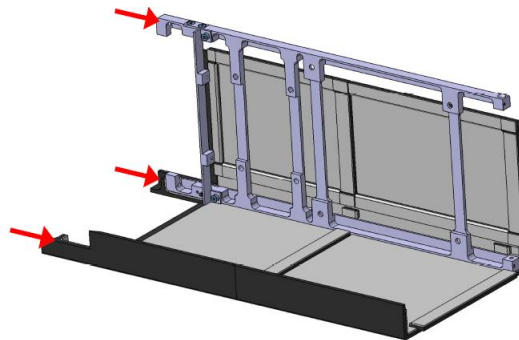


Figure 47: TPS sidewall's connections

The cork in the front forms also a part of the TPS. The P50 cork has been chosen after a material selection campaign at the VKI. This cork is an ablator material, which means that the material consumes itself during re-entry when the surface reaches its sublimation temperature. The surface is cooled by the latent heat of the sublimation heat change, where the hot gas is discharged along with the plasma flow.

The back plate where the antennas are mounted consists of 1mm thick PCB material on a 1mm thick SiC-layer, where the PCB material is facing outwards.

The aeroSDS-panels consists of a 2 mm thick SiC-panel covered with a glass-reinforced laminate FR4 and solar cells.

A general overview of the applied materials for the external structure is given in Figure 48.

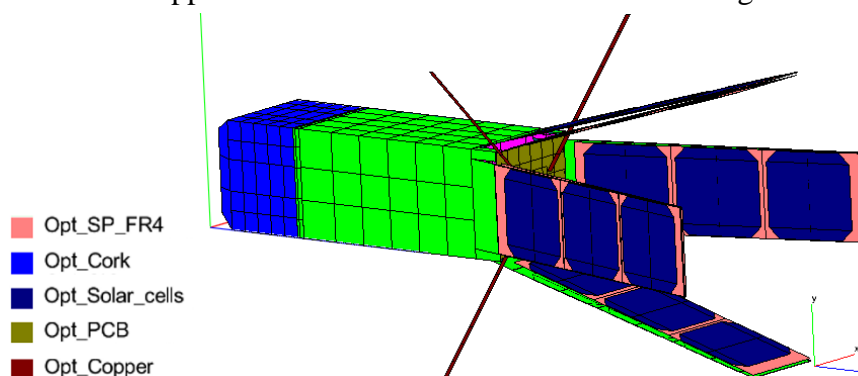


Figure 48: Materials external structure

The cork is insulated from the front-back plate, because heat-fluxes are entering the satellite via the side surfaces of the ceramic front-back plate. In the previous thermal designs for QARMAN, there was no heat-flow conducted through the sidewalls of the front-back plate. This previous mentioned problem has been resolved according to the findings explained in paragraph “5.2 TMM”. The front-back plate is fused with the side walls of the satellite. The material in the corners has a thickness of 5 mm instead of 2 mm for the rest of the TPS front back-plate. This thickening provided an extra structural strength.

All 4 antennas have an equal length of 270 mm. The antennas are connected with a defined conductive interface to the back-antenna plate. The antennas are considered to be linked with an amplifier through a coaxial wire, with a corresponding conductance of a 5 cm long copper wire with a diameter of 1 mm.

7.1.2 Internal geometry

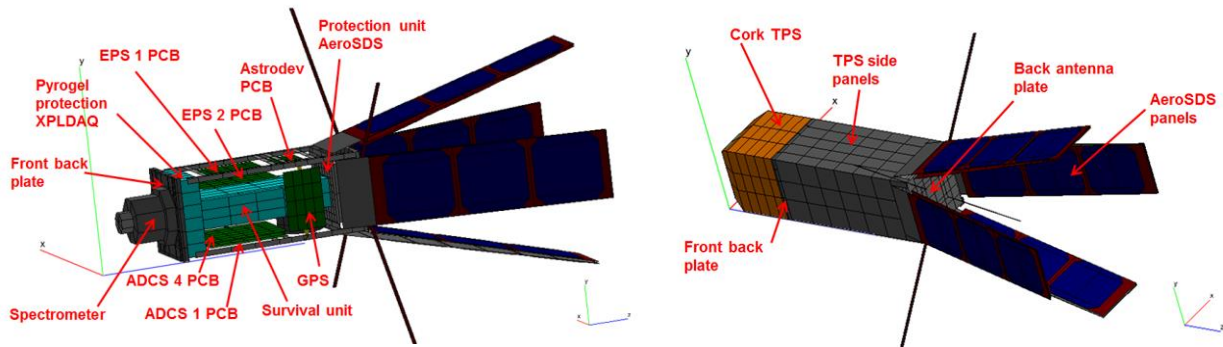


Figure 49: QARMAN geometry

The titanium frame forms the main internal structure to which PCB stacks and other systems are connected with spacers and bolted joints. There are bolted joints for the mounting of the AEROSDS cover, the GPS to the Ti-frame, the spectrometer, front SU and the reaction wheel to the frame. The GL-conductance values are calculated with the Conductive Interface Calculator, where the calculations have been explained in „Chapter 6 detailed design of conductive interfaces“. The titanium rails are not connected with the front part of the satellite, but they are connected with the front SU. So there is no direct conductive connection between the front-back plate and the internal structure of the satellite, which slows down the internal satellite’s temperature increase due to external fluxes and radiation.

There is a 4 mm air-gap between the front protection unit and the front-back plate, again to thermally decouple both surfaces. Eight titanium bolts connect the front protection unit to the front-back plate. The spectrometer is connected with 2 titanium bolts to the front-back plate. The front-back plate consists of silicon carbide with a thickness of 2 mm.

Both survival units, namely the SU for the XPLDAQ and the SU for the OBC, have a groove in there outer surface at the side where both SU’s are facing to each other. This groove has been made in order to make it possible to connect the electrical wires between the electronics inside both SU boxes. Therefore is a contact zone been defined inside ESATAN-TMS, with contact conductance

values of 500 W/m²K for the Pyrogel contact and 1960 W/m²K for the titanium contact zone. Both previous mentioned values were calculated with the Contact Interface Calculator, with the used equations explained in paragraph “6.1 Contact zone”.

Other components and their thermal design such as the survival units and the PCB's with their electronics are explained in the following paragraphs.

7.1.3 PCBs and electronic components

The PCB boards are 1,6 mm thick and consist of two 35 µm thick Cu layers 100 % filled and 4 layers 20 % filled. The rest of the PCB's material consists of fibre reinforced polymers.

The different PCB boards are connected to each other with titanium or stainless steel spacers. The PCB board inside the middle survival unit is connected with Teflon spacers to a titanium box. Teflon is less conductive than titanium and therefore is it possible to insulate the PCB inside the middle SU from the extreme hot external environment during re-entry. The thermal conductance GL-value for spacer and bolted joint connection within the thermal model are calculated with the Conductive Interface Calculator.

The PCB inside the box is glued to an aluminium (Al6061) plate with a nominal thickness of 3 mm, which acts as a heat sink. This plate has been redesigned to a heat sink that follows the contours of the batteries (see Figure 69). The thickness of the plates is calculated in such a way that the original heat sink volume of 24000 mm³ remained the same in comparison with the old version of the thermal design with a flat aluminium plate glued to the PCB. The heat sink forms a heat capacity for the PCB inside the middle SU. This heat capacity is needed, because the SU is so well insulated that there is just a small amount of heat conducted to the outside during a hot orbital case or during re-entry. If the heat dissipated by the electronic components remains inside, thermal hot spots are formed. The heat sink ensures a more equal distributed heat inside the SU and acts as a thermal accumulator. This means that the heat can release its captured heat during a cold orbital case, in order to heat up the components inside the SU.

Some PCBs in the stack are mutually connected with a PC104 power bus connectors, where the connector of a PC104 bus is shown in figure 50. The PC104 connector bus used for the QARMAN satellite has 20 pins. The material of the pins is phosphor bronze. The conductive interfaces of the pins run through the PC104 designed housing. The housing is made of Teflon and is divided in 10 nodes for the ESATAN thermal model. The conductive interface connecting two opposite nodes has a value of 1/10 of the total GL for the PC104 pin connection. Each pin is also soldered to its corresponding PCB board. The pink lines (such as indicate in figure 50) indicate the defined conductive interfaces. The GL conductance values specified for the conductive interfaces determine how well heat is conducted through these conductive interfaces.

The most of the electronic components are designed as thermal nodes with a specified volume and PCB material. Most of the electronic components are rather small, so detailed geometrical design can be neglected, except for the electronic iridium component. The thermal nodes are connected with the PCB through a conductive interface connection with a GL-factor for the soldered joint. The iridium antenna is also defined as a thermal node, but here is the GL-factor defining the thermal conductance of a coax cable. The GL-factors for the soldering is calculated with the Conductive Interface Calculator, according the area of the ground path and the number of pins.

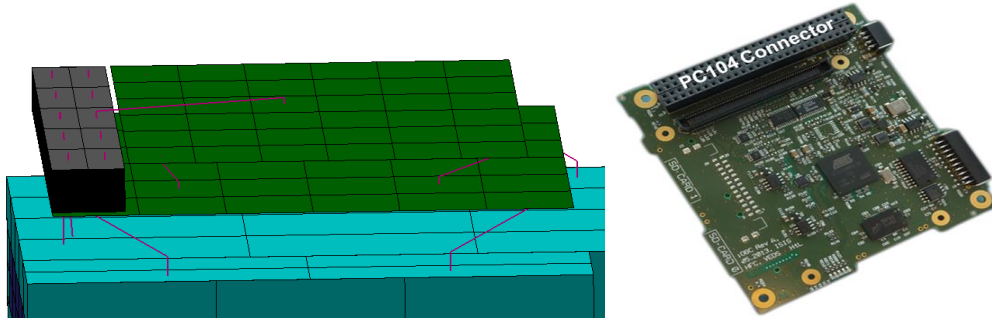


Figure 50: Thermal design PC104 connection (see black)

The IRID has its own PCB, with an air gap of 0,95 mm between the PCB of the survival unit and the PCB of the iridium. The thermal connection of the PCB of the IRID and the PCB of the SU consists of a metallic grounding (see grey bars, see Figure 51: Thermal design iridium component) and a 4 screwed connection of M1.6 screws. So the PCB of the iridium is in contact with the grounding and the grounding at his turn is in contact with the PCB of the survival unit. The PCB of the IRID is 1,2 mm thick PCB material and the box at the top is made of 1 mm thick aluminium 6061. The aluminium box has non-active faces at the inside.

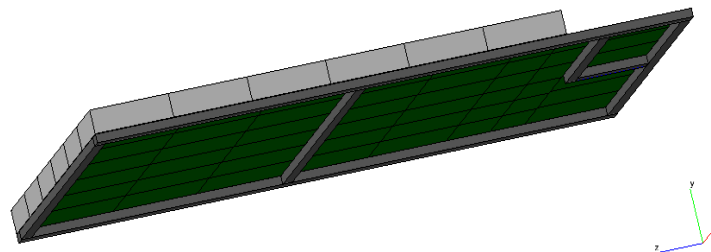


Figure 51: Thermal design iridium component

7.1.4 Protection units

It has been concluded from previous simulations that the primary heat shield formed by the TPS, namely the cork and the multi-layered surface of SiC and fiberfrax, doesn't guarantee that the electronic components survive until the end of the re-entry mission. Therefore, it has been chosen to house the electronics, which need to survive up to the end of re-entry mission, inside a SU. A survival unit is formed by a titanium box filled with Pyrogel insulation. The Pyrogel is a lightweight and low-conductance material. The titanium box has two functions: the first function of the survival unit is to spread the heat in order to reduce hot spots; another function of the titanium box is to house the insulation, which has no mechanical properties to withstand any loads which act on the SU. The QARMAN satellite has 3 survival units, namely a survival unit for the XPLDAQ PCB, a survival unit for the OBC also called the middle SU and a survival unit for the AeroSDS PCBs.

- The first survival unit is placed in the front, housing the XPLDAQ PCB. The XPLDAQ PCB is protected by a titanium box filled with a Pyrogel layer. The Pyrogel layer in this front doesn't have a uniformly distributed thickness, but has a thickness of 7,5 mm at the side walls and a thickness of 12,5 mm at the front and back plates of the box. A part of the spectrometer sticks inside the XPLDAQ protection unit and this part is covered with a 3 mm thick Pyrogel layer.

- The mean survival unit protects the OBC (On Board Computer), the Iridium modem, the batteries, the IMU and all the needed regulators. The survival unit has also a titanium box. The Pyrogel layer has a thickness of 7,5 mm at the walls and at the top and bottom of the box, all the other walls have a 12,5 mm layer thickness.

The first and mean survival unit have a low emissivity outer surface with an emissivity value equal to 0,08. Highly titanium polished surface could have emissivities ranging from 0,08 to 0,19, where the lowest value of 0,08 has been chosen. [51]

- The survival unit for the AeroSDS (see Figure 52) consists of a titanium-silicon carbide (SiC) box. The box has in the front a titanium plate with a thickness of 1 mm and a Pyrogel layer thickness of 7,5 mm. The side walls of the box consist of titanium and silicon carbide with a thickness of 1 mm and covered with Pyrogel layer of 10 mm. There is no low emissivity and low absorptivity foil applied for this box. The SiC is used in the part of the protection unit which surrounds the Iridium Antenna, in order to reduce the EMI (electromagnetic interference).

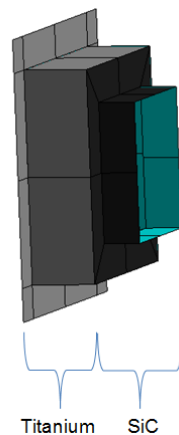


Figure 52: AeroSDS protection unit

The components which need to function to end of re-entry mission are: the OBC, the Iridium modem, both batteries, the IMU, all the needed regulators. All this components are placed on a unique PCB, which is connected with the aluminium heat sink. The XPL DAQ board, which is placed in the front survival unit, shall keep on functioning up to an altitude of 45-50 km.

7.1.5 Cabling

The cabling is defined between two nodes, corresponding to two components which need to be

<i>OBC</i>	-20	+85	-55	+105
<i>Iridium Modem</i>	-30	+70	-40	+85
<i>ADCS Stack</i>	-10	+60	-10	+60
<i>Spectrometer</i>	0	50 (10 degree/hour ramp)	-30	+70
<i>AeroSDS and XPL DAQ</i>	-20	+85	-40	+85
<i>GPS</i>	-20	+85		
<i>Astrodev</i> [37]	-30	+70	-30	+70
<i>Iridium antenna</i> [38]	-40	+85	-40	+85
<i>Reaction wheel</i> [39]	-20	+50	-30	+60

7.2.2 Boundary conditions

The boundary conditions which are needed to be defined within ESATAN-TMS are concerning the dissipated heat loads, the initial temperatures and the temperature profiles of the outer surfaces.

The dissipated heat loads of the different components depend on what for thermal case is tested. A detailed overview of the heat dissipation by the electronic components is given in Table 8.

Table 8: Heat dissipation of electronic components

Component	Dissipated power [W]				Re-entry -
	Hot Case		Cold Case		
	<i>Folded</i>	<i>Deployed</i>	<i>Folded</i>	<i>Deployed</i>	
<i>EPS1</i>	0.0625	0.0625	0.0625	0.0625	0.0
<i>EPS2</i>	0.0187	0.0187	0.0187	0.0187	0.0
<i>OBC+Regulators</i>	0.3	0.3	0.3	0.3	0.4
<i>COMM V/UHF RX</i>	0.3	0.3	0.3	0.3	
<i>COMM V/UHF TX</i>	3.0 (55 s, once per orbit)	3.0 (55 s, once per orbit)	3.0 (55 s, once per orbit)	3.0 (55 s, once per orbit)	0.0
<i>COMM V/UHF BEACON</i>	0.15 (orbit average)	0.15 (orbit average)	0.15 (orbit average)	0.15 (orbit average)	0.0
<i>GPS</i>	1.0	1.0	0.0	0.0	0.0
<i>XPL DAQ</i>	0.0	0.0	0.0	0.0	0.25
<i>AeroSDS</i>	0.25	0.25	0.0	0.25	0.25
<i>ADCS1</i>	0.454	0.454	0.454	0.454	0.0
<i>ADCS3</i>	0.336	0.336	0.336	0.336	0.0
<i>Magnetorquer</i>	0.172 (each, averaged value)	0.172 (each, averaged value)	0.0	0.0	0.0
<i>Reaction Wheel</i>	0.125	0.125	0.0	0.0	0.0
<i>Iridium Spectrometer</i>	0.0	0.0	0.0	0.0	2.9
	0.0	0.0	0.0	0.0	1.11 (peak)

The boundary conditions of the re-entry case are defined by initial temperatures and temperature profiles for the outer surfaces of the satellite. These conditions for the outer surface temperatures are derived from CFD computations, performed by another QARMAN member Thorston Sholz. The results of this CFD analyses, performed for a satellite with a weight of 4 kg, are summarized in Figure 54. From these graph can be clearly seen that the QARMAN satellite has to withstand high temperatures. Therefore is the thermal design of the QARMAN satellite triggered to withstand these enormous heat loads. The re-entry is considered as the mean part of QARMAN's mission. The QARMAN satellite enters with a supersonic speed of Mach 27. Where during this re-entry trajectory, the satellite is exposed to gas temperatures which exceeds 1000 K [35]. Once again, these results show the difference in environmental conditions between the re-entry phase and the orbital phases where outer surfaces have temperatures ranging from -65 to 91 °C.

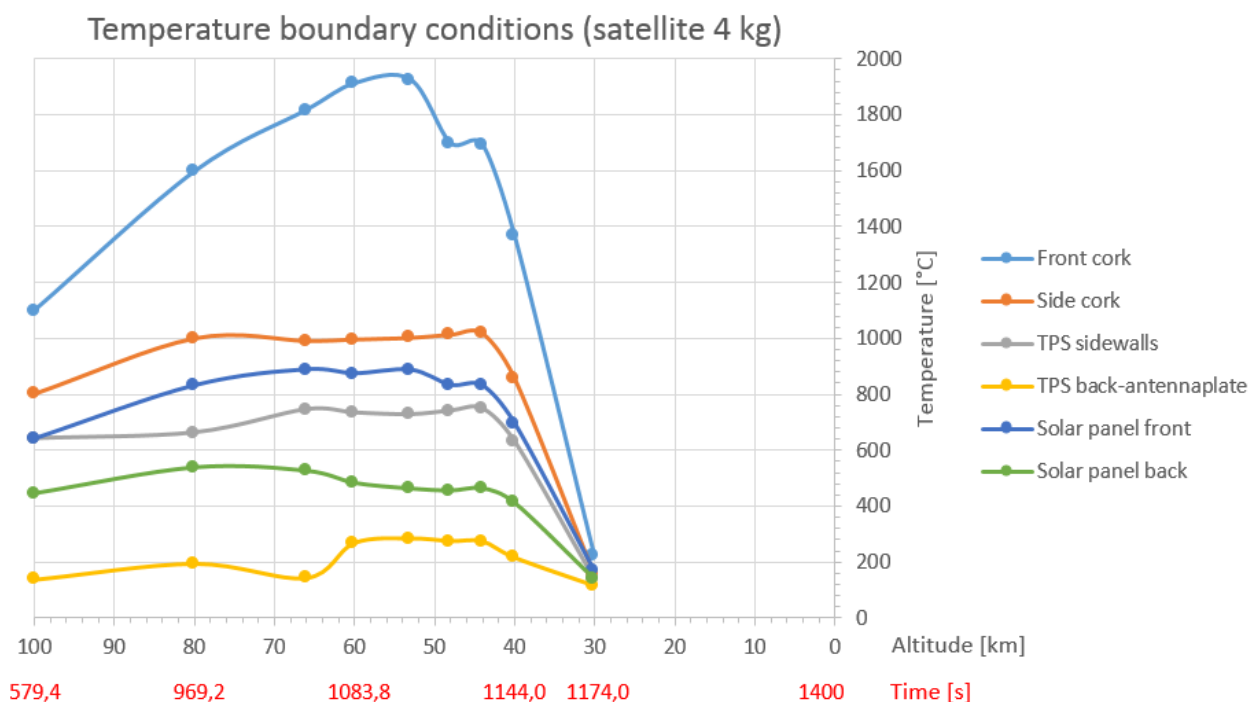


Figure 54: Temperature boundary conditions during re-entry vs. altitude and time, for a satellite weighing 4 kg

The initial temperatures, used to define the temperatures of the structures and components at an altitude of 120 km with re-entry time equal to 0 s, were established with a steady-state cold orbital case. The electronic components are at “low-power mode” in order to save battery power. The satellite is supposed to spin around its longitudinal axis with an angular rate of 10 deg/s, in order to have a more uniform and averaged temperature distribution.

7.2.3 Simulation cases

The hot and cold orbital cases are both a conservative worst case scenario. The hot and cold cases are chosen in such a way, that surfaces, structures and components face the largest temperature gradients and the highest or lowest temperatures, depending on the selected case.

The eclipse ratio or the ratio between the sunlit and eclipse phases for one orbit depends on the orbital plane. The QARMAN satellite's orbit is circular with a fixed inclination of 98° . Other parameters to determine the eclipse timer per orbit, found in the Astronomical Almanac for the 1st January 2016 winter solstice, are the declination and right ascension of the sun relative to an observer on earth. The obtained values are $-78,6^\circ$ for the sun inclination and -23.45° for the right ascension of the sun relative to an observer on earth. The LTAN specified numbers, specified to be used for by QB50, are 8AM and 12AM. Both LTAN numbers specify worst case scenarios for the eclipse time. 8AM is used for the hot case, with a maximum duration of the eclipse of 35,44% of the orbit time. 12 AM is used for the cold case, with a maximum duration of the eclipse of 39,3% of the orbit time [5].

The following table 9 presents the boundary conditions considered for the different orbital cases.

Table 9: Orbital parameters and satellite's attitude for orbital simulations

Parameter	Hot Case		Cold Case	
	Folded	Deployed	Folded	Deployed
<i>Pointing</i>	-Z Axis aligned to velocity direction	-Z Axis aligned to velocity direction	Sun-pointing S axis	Sun-pointing S axis
<i>Spin motion</i>	10 deg/sec on rotation on Z	N/A	85 deg/sec rotation on S; 10 deg/sec rotation on Z	10 deg/sec rotation on Z
<i>Orbit altitude</i>	Circular, 380 km	Circular, 350 km	Circular, 380 km	Circular, 350 km
<i>Orbit inclination</i>	98°	98°	98°	98°
<i>Earth albedo</i>	0.4	0.4	0.2	0.2
<i>LTAN</i>	8AM	8AM	12AM	12AM

The attitude for the hot case is established in order to have the maximum area exposed to the sun. The most conservative cold case would be with the front of the cork continuously pointing to the sun. This means that the batteries aren't charged when the front of the cork points continuously to the sun, which causes a compromised mission caused by reasons different than the thermal design. Therefore, is a new S axis defined for the purpose of the satellite's attitude definition for the cold case. The S axis is formed by the ZY plain of the satellite with an angle of 30° relative to the $-Z$ axis. The $-Z$ -axis is the longitudinal axis of the satellite, which is pointing to the front of the satellite. The primary pointing vector, formed by the new defined S-axis, is defined by the following Cartesian system $[0.0; \sin(30\text{deg}); -\cos(30\text{deg})]$. The pointing vector with a small projected area, mainly composed by the front cork and a small part of the solar cells, allows the satellite to recharge its batteries and leaving the satellite operative. On this axis is also a spin motion of 85 deg/s applied for the folded satellites configuration, which is the maximum residual angular velocity possible, due to orbital injection from the QB50 deployer. The rotation of 10 deg/s

around the longitudinal Z-axis is chosen, because one of the requirements of the satellite is to have a residual angular velocity lower than 10 deg/s after orbital injection.

7.3 Post-processed results

7.3.1 Re-entry

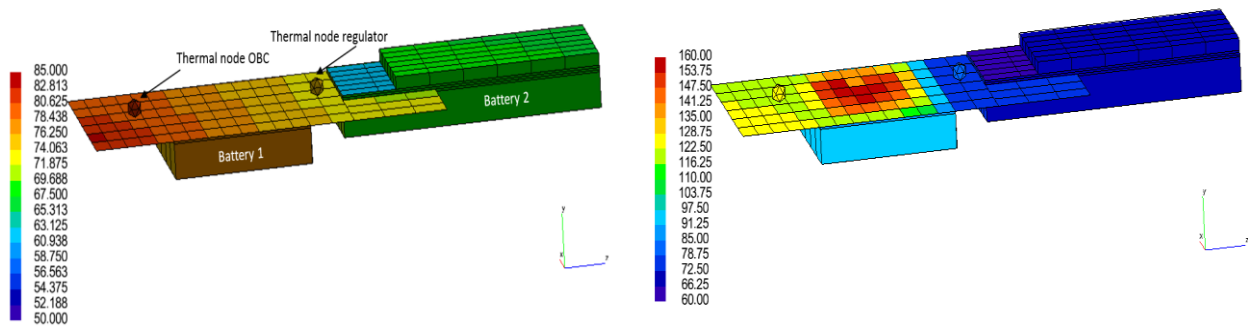


Figure 55: Temperature of components inside SU at the end of re-entry (1400s) (Right: with adapted heat sink and left: without adapted heat sink)

Figure 55 shows the thermal results of the components inside the main survival unit at the end of the re-entry mission, with time equal to 1400s. The left picture of figure 56 shows the results for an adapted heat sink, where an extra aluminium 6061 layer of 1,7 mm thick was placed between the batteries and PCB. When there is no adapted heat sink used, see right picture of figure 56 where the maximum temperature rises up to 160 °C. This extra layer of aluminium extends the life time of the batteries during re-entry. The new heat sink design used for the following simulations is schematically shown from its side-view in figure 56.

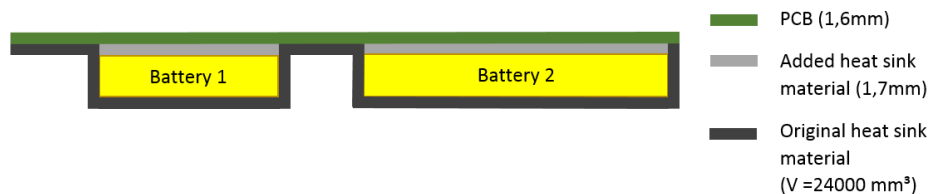


Figure 56: Schematic representation of the new heat sink

The following graph show that the thermal protection system and the survival units are performing very well. The internal components are insulated from their extreme thermal environment. Despite the good insulation from those materials, there is still a heat flux conducted to the inside of the QARMAN satellite and the side panels are also radiating heat inside the satellite. As stated before, all the components which need to function until the end of the re-entry mission, namely the OBC, the Iridium modem, both batteries, the IMU, all the needed regulators, are placed in one main survival unit in the middle of the satellite. The XPL DAQ board, which is placed in the front survival unit, shall keep on functioning up to an altitude of 45-50 km. Figure 57 shows that all the components, except for the batteries, survive up to the end of the re-entry phase. Battery 1 and 2 respectively reach their temperature limit of 50 °C after 1150 s and 1200s, which is more or less 3 minutes before the satellite crashes. Nevertheless, the batteries are not been charged anymore during the re-entry phase and the operational temperatures are valid for long term operation. If the lithium polymer batteries continue their operations after their temperature limits for long term

operations are exceeded, they will remain operating but with decreasing capacity. The XPLDAQ component, placed in the front survival unit, survives up to 1080 s (which corresponds with an altitude of about 80km). The XPLDAQ survives less long than the results found in previous simulations, because there was a bug found in the thermal design of the front-back plate (see paragraph “5.2 TMM”). There is now a heat flow coming in from the outside of the ceramic front-back plate to the inside of the satellite. The front-back plate gets a maximum temperature of 630 °C at 1080 s, the moment when the XPLDAQ component reaches its limit temperature. A hotter ceramic front-back-plate, means more heat radiated to the survival unit of the XPLDAQ component and causes the high temperatures of the XPLDAQ component.

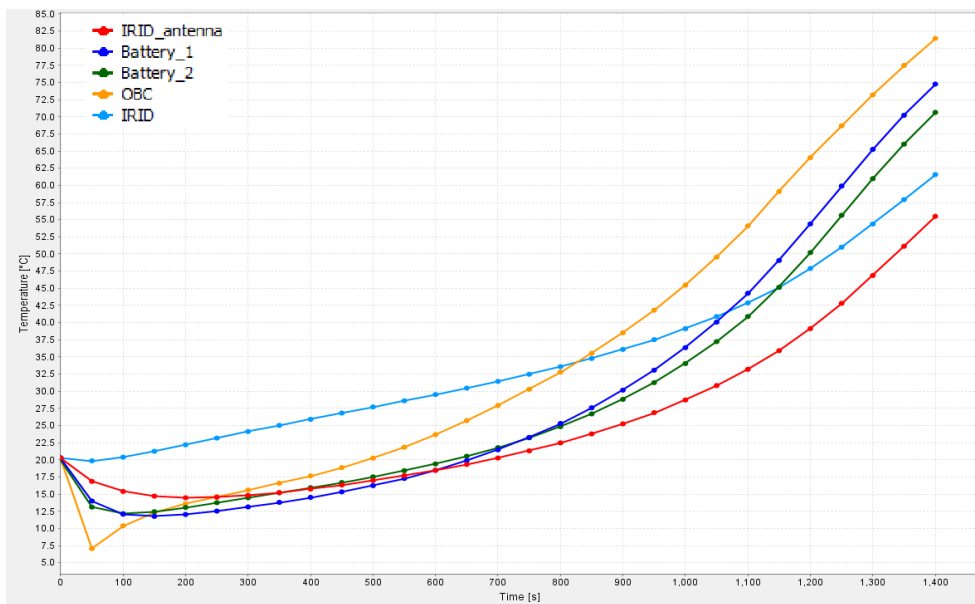


Figure 57: Temperature of main SU electronic components

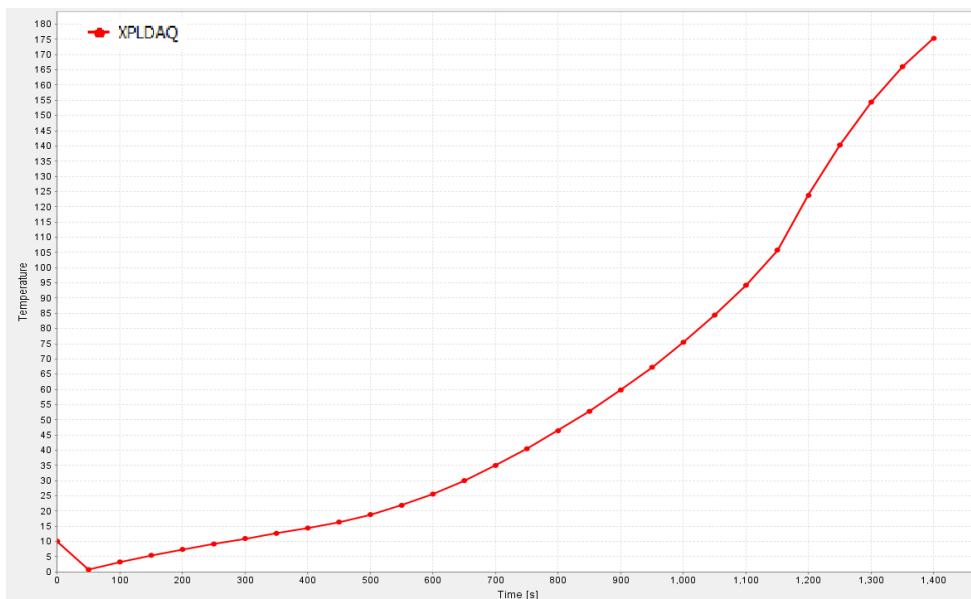


Figure 58: XPLDAQ board temperature variation

The following graph, shown in figure 59, indicates the temperature of the spectrometer versus the re-entry time. These presented results show large improvements in comparison with the results obtained from previous simulations, where the spectrometer easily reached 270 °C at the end of

the re-entry mission. The larger temperatures of the spectrometer for the old thermal designs was caused by the fact that the thermal dissipated heat of the spectrometer was applied on the outer surfaces of the spectrometer. The thermal design of the spectrometer has now a different node numbering for the outer and inner surfaces, so the temperatures of the outer surfaces are not coupled to the inner ones. There has also been a PCB added with one single node, where now the thermal dissipated heat from the spectrometer's electronics has been applied to. The design of the spectrometer is protected, so no more details about the internal design are known. The thermal design of the spectrometer should be more detailed, in order to have more accurate temperatures for the spectrometer. The spectrometer reaches its maximum temperature of 50 °C after 950 s.

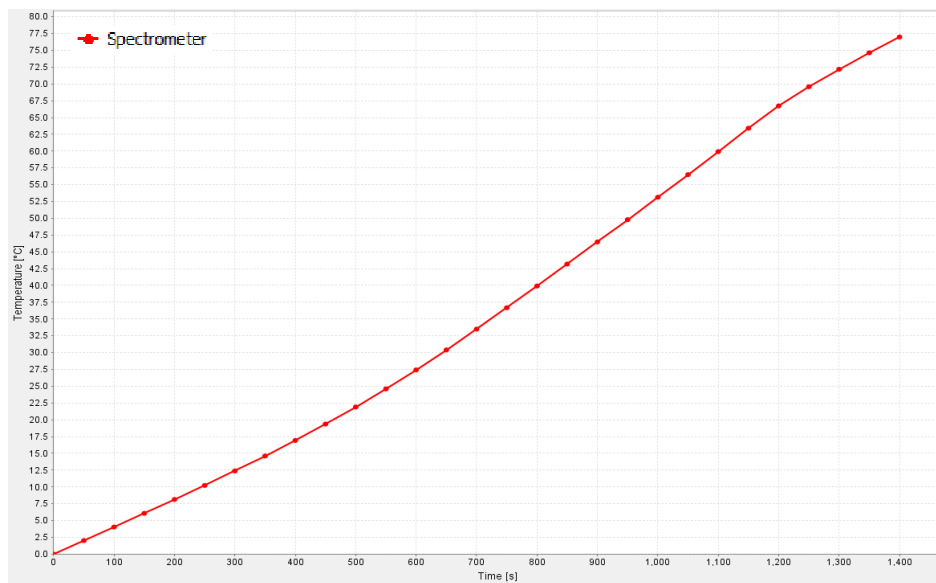


Figure 59: Spectrometer temperature variation

Another remark has to be made about the graphs shown in figure 57 and 58. It can be seen that there is no smooth transition between the data at 0 s and the other data at a time step of 50 s. This can be explained as following, the temperatures at 0 s were obtained from a simulation with the satellite at low power mode and at a steady-state cold orbital case. The next data point, namely the one calculated for 50 s after the re-entry started, comes from the defined transient re-entry case.

7.3.2 Cold orbital case

In the previous analysis of the old thermal model, the AeroSDS boards reached temperatures below the operative limit. In this improved thermal design configuration, there are no problems present for the components inside the satellite during a cold orbital phase. The minimum and maximum reached temperatures are within their temperature limits, with margins larger than 5°C. From the following figures 60 and 61, it can be clearly seen that the maximum reached temperature of the components for a configuration with folded AeroSDS panels are $\pm 5 - 10$ °C higher, except for the AeroSDS component, in comparison with the maximum reached temperatures of the components inside a satellite with deployed AeroSDS panels. This last observations about the temperatures of the AeroSDS components can be explained by the fact that the survival unit with the AeroSDS components inside, has a direct radiative link with the orbits environment.

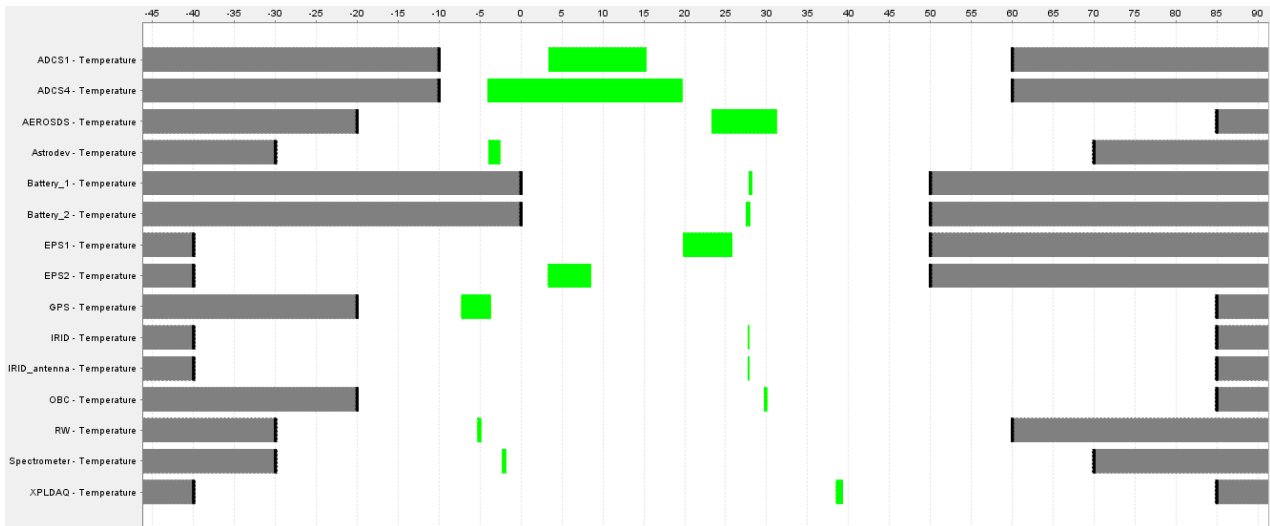


Figure 60: Limits report cold orbital case with AeroSDS panels in deployed configuration

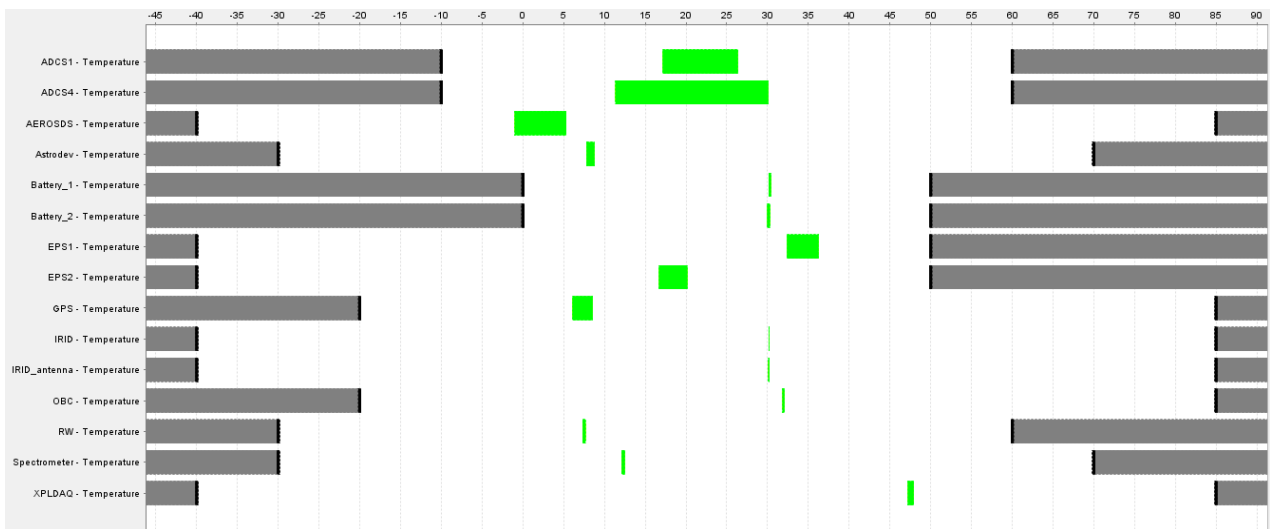


Figure 61: Limits report cold orbital case with AeroSDS panels in deployed configuration

7.3.3 Hot orbital case

The results of the analyses performed for the hot orbital cases are showed in the limits reports of figure 62 and 63. The simulation case with the AeroSDS panels folded shows again higher maximum temperatures for the components. It can be seen that the batteries reach their maximum operative limit temperature for both AeroSDS configurations. All the other components are working within their operative temperatures. These figures 62 and 63 show the results of extreme conservative hot cases, because the temperatures were obtained by a thermal simulation were first a steady-state analysis and then a transient analysis was defined. This means that the initial temperatures for the transient analysis were derived from the steady-state analysis. In order to reach the steady-state condition, the satellite shall orbit for long time in this same hot orbital case conditions. Therefore another simulation is performed with only transient iterations.

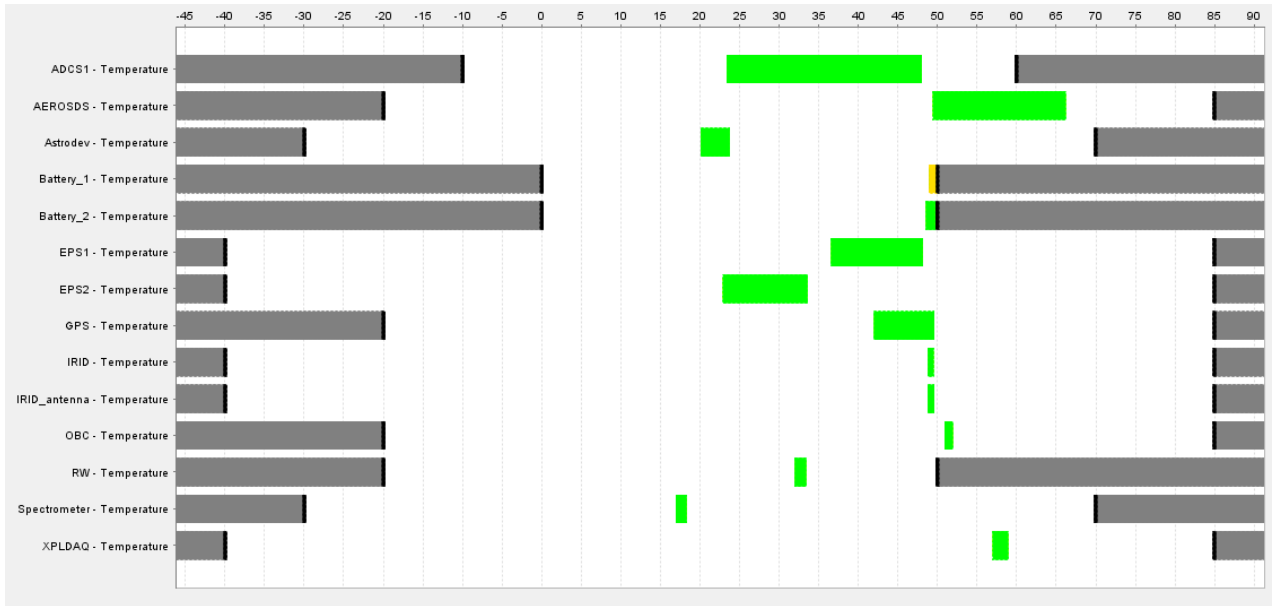


Figure 62: Limits report hot orbital case with AeroSDS panels in deployed configuration

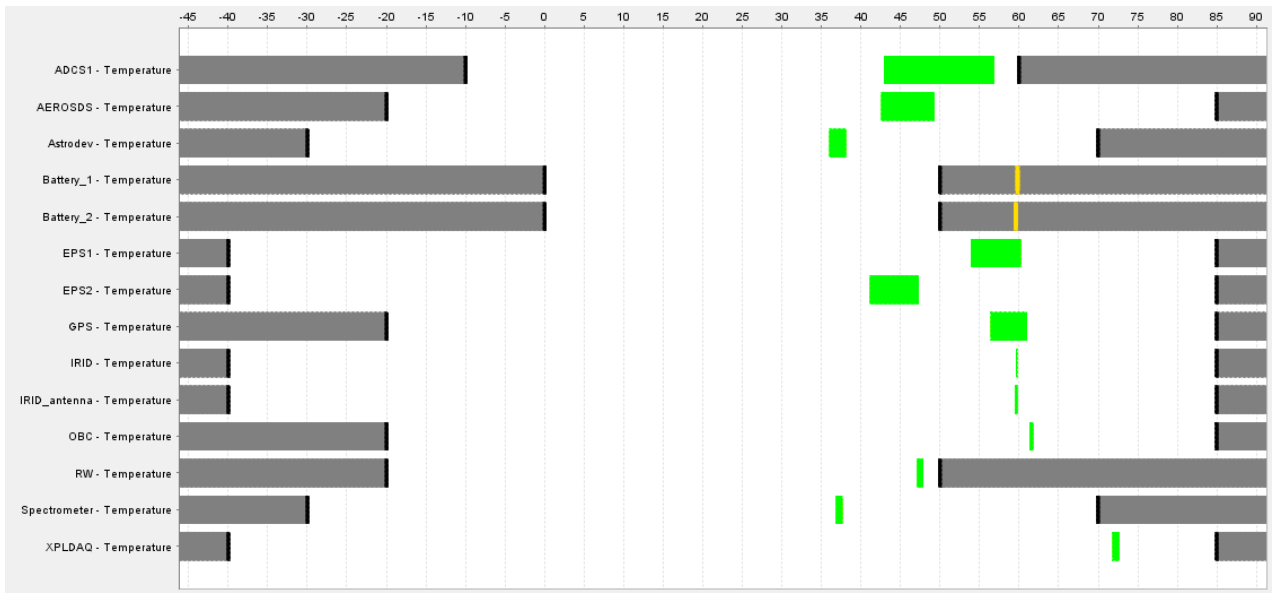


Figure 63: Limits report hot orbital case with AeroSDS panels in folded configuration

Figure 64 shows the results of the simulation case with only transient iterations for the configuration with the AeroSDS panels deployed. The results shown here correspond with the 19th and 20th orbital cycle. Battery 1 and 2 have reached respectively a maximum temperature of 45 °C and 44,5 °C after 110 000 seconds, or the 20th orbit. The problem of batteries getting overheated could be resolved by applying a very low emissivity surface on the insulation material inside the survival unit. It should be avoided that this coating is electrical conductive. The Pyrogel has a negative shape where the PCB and its components can fit in. If a negatively shaped Pyrogel coated with an electrical conductive material, touches the PCB, it forms an electrical path.

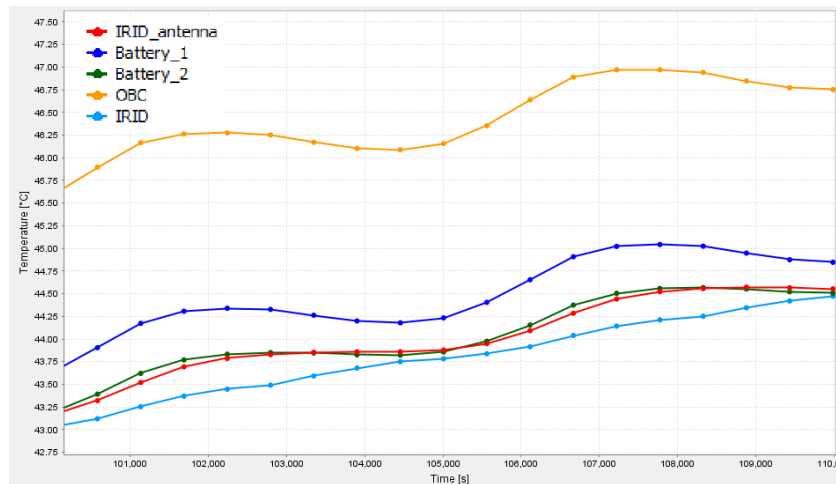


Figure 64: Transient analysis results for the temperatures of the components inside the main SU for a hot orbital case with AeroSDS panels in deployed configuration

The simulations where a emissivity of 0,09 at the in- and outside of the survival unit is used, show a temperature reduction of 6-7 °C for both batteries for the AeroSDS panels in a folded configuration. An extra coating reduces the internal temperature during a hot orbital case, but the batteries still remain to have a temperature which exceeds the 50 °C.

7.3.4 General conclusion

The QARMAN satellite provides a thermally controlled environment that ensures a reliable performance of the components and on-board systems of the satellite. The thermal control systems are designed in such a way that the on-board systems operate within their temperature limits during all phases of the QARMAN mission. The satellite is insulated as well as possible from its outer environment, therefore are internal components less sensitive for external radiation during the hot orbital cases and the enormous heat fluxes during re-entry. The insulation also prevents that the components get too cold during the cold orbital cases, so heat is kept inside the survival units and the satellite. The following chapter will indicate the mean and significant parameters which influence the thermal design of the QARMAN satellite.

Globally, it can be seen from the results of the hot and cold thermal cases that the internal components have smaller temperature gradients during the orbital cycling.

The thermal design for the QARMAN satellite has been largely improved for the re-entry case, where in for the old model most of the components were out of their operating temperatures after 2-3 minutes.

The temperatures of the batteries never drop below zero degrees Celsius, which is absolutely not allowable because a lithium polymer gives problems with lithium plating at negative temperatures. So no extra measures are needed to heat up the batteries with heaters. At the other hand, the thermal simulations confirmed the sensitivity of the batteries. Therefore it is strongly advised to measure the properties of the batteries at higher temperatures.

8 Uncertainty analysis re-entry

The purpose of the following simulations is to screen which design elements affect significantly the temperature of the survival unit (SU) electronic components. This identifies the parameters which are important to focus on for further investigations. Interactions between factors aren't indicated in this screening analysis. The effects of the identified significant parameters are afterwards further investigated with a design of experiments (DOE). This analysis gives also the possibility to check the robustness of the thermal design of the QARMAN satellite.

The following analyses are only performed for the re-entry case, because the thermal design is tuned to survive the re-entry which is the main mission of the QARMAN design. It is also much easier to see the influence of sudden parameters on the thermal design due to the extreme heat fluxes during re-entry which causes large temperature gradients.

8.1 Screening analysis

The first step of the uncertainty analysis is to select the critical design parameters that need some more research. This screening analysis can also be seen as a sensitivity analysis. The response of the thermal model is explored in order to test the accuracy of the model and the validity of the assumptions made. This analysis gives an indication of the rate of change or also called the main effect on the output parameter, namely the temperature of the electronic components inside the survival unit, when an input parameter is changed. A main effect parameter calculated with the following equation 8.1.

$$E_f = \overline{F_{(+1)}} - \overline{F_{(-1)}} \quad (8.1)$$

With $\overline{F_{(+1)}}$ the temperature of a component with the screened parameter at a high level (see cases 2 of the data presented in table 10) and $\overline{F_{(-1)}}$ is the temperature of a component with the screened parameter at a low level (see cases 3 of the data presented in table 10). The influences of the parameters are tested one fact at the time.

8.1.1 Test parameters

The thermal model of the QARMAN satellite is the input for thermal simulations. The observable temperature responses of the several QARMAN subsystems are the output of the thermal simulations. Some of the process variables, namely: emissivity ε , absorptivity α , specific heat C_p , conductivity k , material density ρ , conductive interfaces CI and heat dissipated by the electronic components Q are controllable whereas other variables, such as the space environmental conditions aren't controllable. The space environmental conditions are kept constant for the thermal simulations, because there are treated as the boundary conditions of the thermal simulations.

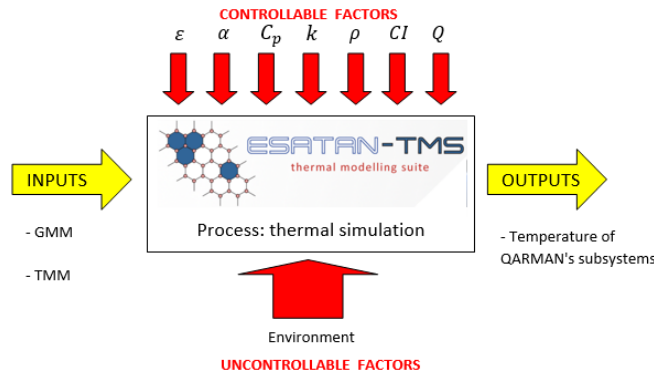


Figure 65: Thermal control system

The underneath listed parameters (see table 10) have uncertainties about material properties, because innovative materials such as Pyrogel and sintered titanium aren't extensively tested by companies. The influence of the thickness of materials which form the thermal barrier against the enormous heat fluxes during re-entry for the components inside the SU are also tested. A mistake during manufacturing can always happen and therefore it is important to know the influence of the thickness of materials on the components temperatures inside the SU. The length of electrical wiring is also selected as a parameter, because the current lengths are based on the 3D model. It is likely that the routing of the cabling in practise will differ due to practical reasons, more bends and no straight cabling. Emissivity of the foil around the survival units is also a test parameter, because IR emissivity values of materials are the input values for ESATAN-TMS to define the optical properties of materials. However it is more intuitively that the material's absorptivity determines how well a material heats up, because emissivity specifies only how well a real body radiates energy as compared with a black body. As explained in Chapter 2, paragraph 2.2.4 "Algebraic solution of multi-surface enclosure problems of grey bodies", yields Kirchoff's law $\alpha_{T,\lambda} = \epsilon_{T,\lambda}$ for ESATAN-TMS simulations. So the specified emissivity value for IR wavelengths in ESATAN-TMS is equal to the absorptivity at the IR spectrum of the defined optical properties of a certain material. There are 12 different parameters screened for this analysis (see table 10).

Table 10: 12 test parameters for the sensitivity analysis

Parameter	Initial value	Input value				Source
		Case 1	Case 2	Case 3	Case 4	
Pyrogel emissivity [-]	0,15	0,12 (-20%)	0,135 (-10%)	0,12 (+10%)	0,12 (+20%)	[40]
Pyrogel density [kg/m ³]	200	160 (-20%)	180 (-10%)	220 (+10%)	240 (+20%)	[40]
Pyrogel specific heat [J/kg.K]	1046,7	837,36 (-20%)	942,03 (-10%)	1151,37 (+10%)	1465,38 (+20%)	[41]
Pyrogel conductivity [W/m.K]	0,02 (T = 0°C)	0,016 (-20%)	0,018 (-10%)	0,022 (+10%)	0,024 (+20%)	[40]
	0,023 (T = 100°C)	0,018	0,021	0,025	0,028	
	0,028 (T = 200°C)	0,022	0,025	0,031	0,034	
	0,035 (T = 300°C)	0,028	0,032	0,039	0,042	
	0,046 (T = 400°C)	0,037	0,041	0,051	0,055	
	0,064 (T = 500°C)	0,051	0,058	0,070	0,077	
0,089 (T = 600°C)	0,071	0,080	0,098	0,117		
Low emissivity foil coated SU [-]	Low 0,05 ε foil in- and outside (High polished Al-foil)		Low 0,05 ε foil in- and outside SU	No low 0,05 ε foil in- and outside SU		[42]

<i>Titanium (sintered) specific heat [J/kg.K]</i>	580,3	464,2 (-20%)	522,3 (-10%)	638,3 (+10%)	696,4 (+20%)	[43]
<i>Titanium conductivity (3D-printed) [W/m.K]</i>	16	12,8 (-20%)	14,4 (-10%)	17,6 (+10%)	19,2 (+20%)	[44]
<i>Thickness of pyrogel [mm]</i>	Front/ back 7,5 Side 12,5	-2mm	-1mm	+1mm	+2mm	
<i>Thickness of fiberfrax [mm]</i>	3	2,4 (-20%)	2,7 (-10%)	3,3 (+10%)	3,6 (+20%)	
<i>Thickness of the ceramics sidepanels [mm]</i>	2	1,6 (-20%)	1,8 (-10%)	2,2 (+10%)	2,4 (+20%)	
<i>Length of the wiring [m]</i>	l_{initial}	$l_{\text{initial}} -40\%$	$l_{\text{initial}} -20\%$	$l_{\text{initial}} +20\%$	$l_{\text{initial}} +40\%$	
<i>Soldering conductivity [W/K]</i>	GL_{initial}	$GL_{\text{initial}} -20\%$	$GL_{\text{initial}} -10\%$	$GL_{\text{initial}} +10\%$	$GL_{\text{initial}} +20\%$	

Cases 2 and 3 are respectively the low (-) and high (+) levels for a certain screened parameter. Most parameters also have a case 1 and 4, which are respectively the extra low (--) and extra high (++) test levels. The property variations due to temperature changes, manufacturing tolerances, imperfections,... all affect the input value of the 12 listed design parameters. In order to account for these effects, is the input variable changed by $\pm 10\%$ of its nominal value for the case 2 and 3. It is found in literature [45] that for sensitivity analyses the input variable usually varies with a small amount of $\pm 5\%$ of the nominal value. For the conducted sensitivity analysis is a 5% higher variation selected, namely a variation of $\pm 10\%$, in order to take in account a larger safety margin. A larger uncertainty margin is taken in account for the lengths of the electrical wiring, because the current lengths are estimated with the help of the 3D model of the QARMAN satellite. The lengths of the electrical wiring is changed by $\pm 20\%$ to account for other possible routing paths. The thickness of the Pyrogel isn't deviated by some percent of the nominal value for the different test cases. For this test parameter it has been chosen to make the thickness of the Pyrogel vary with 1 to 2 mm, because Pyrogel is a fabric that needs to be cut in the right shapes to fit in the SU. This cutting process is less accurate than the normal applied 10 or 20% variation for the sensitivity analysis.

The results of the temperatures of the electronic components tested at a case 1 or 4 setting of a certain parameter aren't used for the statistical analysis of the simulation results. Case 1 and 4 settings are used to identify the thermal behaviour of an electronic component inside the main survival unit when the assumed normal parameter limit [*Parameter value for case 2 ; Parameter value for case 3*] is exceeded. The results for case 1 and 4 are used to construct the dotted line in the main effect plot (see figure 67).

8.1.2 Pareto analyse

A pareto plot identifies the design parameters that have a significance influence on the temperature of the components inside the main survival unit. The absolute values of the calculated main effects are displayed in the pareto plot (see figure 66).

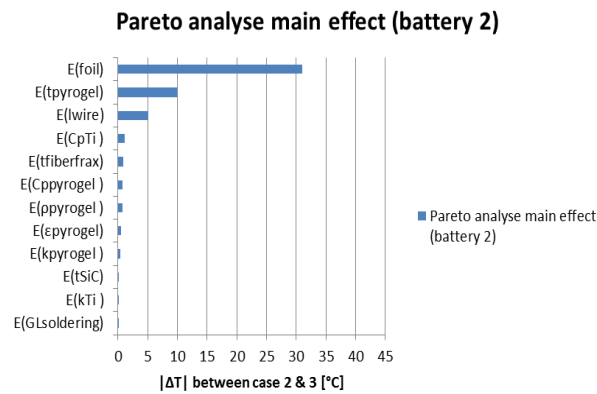


Figure 66: Pareto analysis of the main effects on battery 2

Figure 66 shows only the results for the pareto analysis of the main effects on battery 2, because the DOE of the selected critical parameters focuses on battery 2. Battery 2 has been selected for further DOE investigation due to the fact that the batteries are the most sensitive elements to the heat flux inside the main survival unit. The batteries have the tightest temperature limit, namely [0 °C ; 50 °C], in comparison with all the other electronic components. This implicates that when the thermal design of the QARMAN satellite is improved to have the temperature of battery 2 between its temperature limits, it also has a positive influence on the thermal behaviour of the other electronic components. The following presented screening analysis is performed with ESATAN-TMS for temperatures of the different electronic components at 1400 s after the start of the re-entry phase. After 1400 s is the QARMAN satellite crashed on the earth's surface and is the QARMAN mission over, at least the special segment of the mission.

The top 3 of main effects which influence the temperatures of the electronic components at the most are low emissivity foil, the lengths of the electric wiring and the thickness of Pyrogel. The plots shown in appendix C.1 show that “no use of a low emissivity foil” has a large impact on the temperatures of the electronic components inside the survival unit. The temperature impact on the electronic components inside the SU, when no low emissivity foil is used, is about 100 °C for IMU and 40 °C for all the other components. The length of the electric wiring also shows to have an impact on the components temperatures, because a longer wiring means a higher thermal resistance and a lower heat flux which is conducted from the hotter regions outside the survival unit to the inside of the survival unit. The thickness of the Pyrogel, which forms the last thermal barrier for heat coming inside the SU, has also an influence on the components temperatures.

The decision limits (DL) for identifying the significant effects are calculated with the *Lenth's method* [46]. These decision limits give an idea of the computed effects which are significantly different from zero. The following used method is used to determine the decision limits.

- 1) Order the absolute values of the main effects $|E_{f,j}|$ in increasing order.
- 2) Find the median of the ordered absolute values of the main effects and compute the first preliminary estimate, namely $s_o = 1,5 \cdot \text{median}_j |E_{f,j}|$.
- 3) Take out the main effects which are $|E_{f,j}| \geq 2,5 \cdot s_o$ and find the new median of the remaining $|E_{f,j}|$.

- 4) The PSE, pseudo standard error, which is Lenth's estimate for σ_{effect} , is calculated as following: $PSE = 1,5 \cdot median \{ |E_{f,j}| : |E_{f,j}| < 2,5 \cdot s_o \}$
- 5) The degrees of freedom used for the Lenth's method is $m/3$, with m the initial number of effects in the algoritm. The effects are significant when $|E_{f,j}| > t_{\alpha/2, m/3} \cdot PSE$

The hypotheses test make use of the student's T-distribution, because a standard deviation of a sample is used for the T-distribution instead of the standard deviation of a population, which is used in a normal distribution. The zero hypotheses states that an effect is neglected if $H_0: \mu_{effect} = 0$ and the alternative hypotheses state that an effect is significant when $H_1: \mu_{effect} \neq 0$. The alternative hypotheses is tested by the Lenth's as following: $|E_{f,j}| > t_{\alpha/2, m/3} \cdot PSE$. The $t_{\alpha/2, m/3}$ is the T-value for a test with a confidence level of α for a two-tailed T-distribution and $m/3$ degrees of freedom. There are 12 effects tested for the performed screening analysis and there is a confidence level of 90% is selected to make sure that there isn't an import parameter neglected for the screening analysis, therefore is $t_{0,95,4} = 2,132$. The red marked effects in the following table 11 show the significant parameters, for each component inside the survival unit and the IRID-antenna in the back.

The length of the electrical wiring and foil have a significant influence on the temperatures of the components. Therefore, the correct cabling lengths, which will be known after QARMANs implementation tests are preformed, should be implemented in the ESATAN thermal design of QARMAN. A low emissivity foil, for example an aluminium foil, should be used to insulate the SU from the radiative environment. Also the thickness of Pyrogel has a significant effect on the temperature of battery 2. The emissivity of the applied foil will be investigated in some more detail.

Table 11: Calculated decision levels (DL) and significant effects (red marked)

Component Battery 1	E(GLsoldering)	0,01	Component Battery 2	E(GLsoldering)	0,01	Component IMU	E(GLsoldering)	0,01	Component IRID	E(k _{Ti})	0,02
	E(k _{Ti})	0,03		E(k _{Ti})	0,02		E(t _{sic})	0,09		E(t _{sic})	0,02
	E(t _{sic})	0,04		E(t _{sic})	0,03		E(k _{Ti})	0,16		E(GLsoldering)	0,02
	E(k _{p_{pyrogel}})	0,61		E(k _{p_{pyrogel}})	0,42		E(ε _{pyrogel})	0,44		E(k _{p_{pyrogel}})	0,27
	E(ε _{pyrogel})	0,65		E(ε _{pyrogel})	0,54		E(k _{p_{pyrogel}})	1,93		E(ε _{pyrogel})	0,32
	E(ρ _{pyrogel})	1,01		E(ρ _{pyrogel})	0,71		E(t _{fiberfrax})	2,24		E(C _{p_{pyrogel}})	0,59
	E(C _{p_{pyrogel}})	1,01		E(C _{p_{pyrogel}})	0,71		E(ρ _{pyrogel})	3,29		E(t _{fiberfrax})	0,68
	E(t _{fiberfrax})	1,01		E(t _{fiberfrax})	0,86		E(C _{p_{pyrogel}})	3,29		E(ρ _{pyrogel})	0,69
	E(C _{p_{Ti}})	1,53		E(C _{p_{Ti}})	1,13		E(C _{p_{Ti}})	4,42		E(C _{p_{Ti}})	0,90
	E(t _{pyrogel})	1,96		E(l _{wire})	5,12		E(l _{wire})	6,08		E(t _{pyrogel})	1,19
	E(l _{wire})	6,10		E(t _{pyrogel})	10,00		E(t _{pyrogel})	6,48		E(l _{wire})	3,09
	E(foil)	40,11		E(foil)	30,99		E(foil)	99,97		E(foil)	25,83
Median	1,01	Median	0,71	Median	2,77	Median	0,64				
S₀	1,52	S₀	1,07	S₀	4,15	S₀	0,95				
2,5 · S₀	3,79	2,5 · S₀	2,66	2,5 · S₀	10,37	2,5 · S₀	2,38				
Median effect < 2,5 · S₀	0,83	Median effect < 2,5 · S₀	0,54	Median effect < 2,5 · S₀	2,24	Median effect < 2,5 · S₀	0,46				
PSE	1,25	PSE	0,81	PSE	3,36	PSE	0,68				
DL	2,65	DL	1,73	DL	7,16	DL	1,46				
Component IRID-antenna	E(GLsoldering)	0,01	Component OBC	E(GLsoldering)	0,01	Component regulator	E(k _{Ti})	0,03			
	E(k _{Ti})	0,02		E(k _{Ti})	0,03		E(t _{sic})	0,04			
	E(t _{sic})	0,02		E(t _{sic})	0,05		E(GLsoldering)	0,04			
	E(k _{p_{pyrogel}})	0,38		E(k _{p_{pyrogel}})	0,72		E(k _{p_{pyrogel}})	0,73			
	E(ε _{pyrogel})	0,40		E(ε _{pyrogel})	0,72		E(ε _{pyrogel})	0,65			
	E(ρ _{pyrogel})	0,61		E(t _{fiberfrax})	1,06		E(t _{fiberfrax})	1,07			
	E(C _{p_{pyrogel}})	0,61		E(ρ _{pyrogel})	1,26		E(ρ _{pyrogel})	1,15			
	E(t _{fiberfrax})	0,73		E(C _{p_{pyrogel}})	1,26		E(C _{p_{pyrogel}})	1,15			
	E(C _{p_{Ti}})	0,94		E(C _{p_{Ti}})	1,82		E(C _{p_{Ti}})	1,70			
	E(t _{pyrogel})	1,23		E(t _{pyrogel})	2,37		E(t _{pyrogel})	2,23			
	E(l _{wire})	2,09		E(l _{wire})	6,68		E(l _{wire})	6,18			
	E(foil)	26,38		E(foil)	44,97		E(foil)	43,12			
Median	0,61	Median	1,16	Median	1,11						
S₀	0,91	S₀	1,74	S₀	1,67						
2,5 · S₀	2,29	2,5 · S₀	4,35	2,5 · S₀	4,16						
Median effect < 2,5 · S₀	0,61	Median effect < 2,5 · S₀	0,89	Median effect < 2,5 · S₀	0,90						
PSE	0,91	PSE	1,34	PSE	1,35						
DL	1,95	DL	2,85	DL	2,88						

8.1.3 Main effect plots

The main effect plot shows the response values of one design parameter at different input values. The red dotted line shows the level of the nominal thermal case setting of the QARMAN satellite. The full blue line shows the mean response values of the selected design parameter at a high- and a low-level setting, $F(+1)$ and $F(-1)$. The blue dotted line of figure 67 gives an indication of the direction of the component temperature when the value of the design parameter is reduced to a value lower than the low-level setting ($=$ case 1) and increased to a value higher than the selected high-level setting ($=$ case 4). The red dotted line of figure 67 shows the temperature of the component when all the 12 different parameters, which are varied one-at-the-time for this sensitivity analyses, are set on their nominal values.

The sign of the main effect gives an indication of the direction of the effect. A positive sign means that the temperature response of a subsystem is higher at a high level parameter setting in comparison with the temperature of a subsystem at a low level setting. A negative sign means that a component's temperature response at a low level is higher in comparison with the temperature response at a high level setting. The magnitude of the effect gives an indication about the strength and influence of the screened parameter on the components temperature.

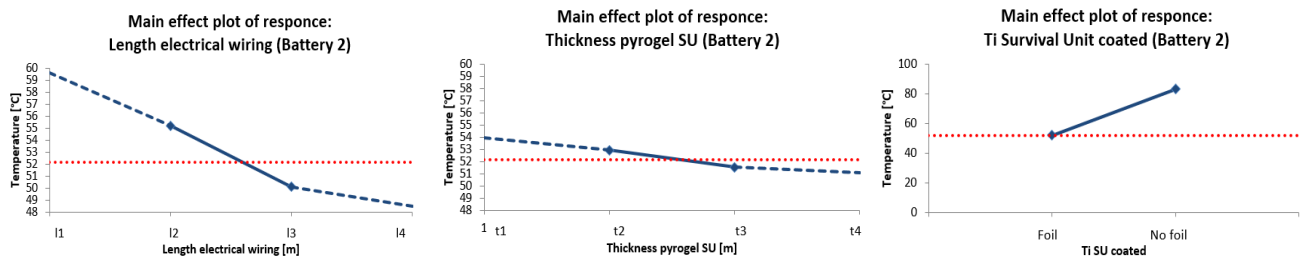


Figure 67: Main effect plot for the 3 most significant parameters which influence battery 2

The notations l_1 , l_2 , l_3 and l_4 of the left figure 67 refer to the input values for case 1, 2, 3 and 4, as presented in table 10. The same applies for the notations t_1 , t_2 , t_3 and t_4 of the middle figure 67.

Figure 67 shows only the results of the main effect plot of the 3 most significant parameters that influence the second battery's temperature, because the DOE of the selected critical parameters focuses on battery 2. The left figure 67 shows a decrease in temperature of battery 2 when the length of the wires increases. Longer electrical wiring means a higher thermal resistance, so less heat will be conducted through the wires inside the Survival unit. The middle figure 67 shows a decrease of temperature of battery 2 when the thickness of the Pyrogel increases. A thicker layer of Pyrogel forms a better thermal barrier against the enormous heat flux coming from outside of the SU.

All the other main effect plots shown in appendix C.2 give a clear indication that Pyrogel emissivity, Ti conductivity and SiC thickness aren't influencing the temperatures of the components inside the SU, even when the values of those mentioned parameters are increased or decreased with 20 % in comparison with the initial value. The temperatures of the components change only with some degrees Celsius (max. 4 °C) when the values of the Pyrogel density, Pyrogel specific heat, Pyrogel conductivity, Ti specific heat, thickness of Pyrogel in the SU and

fiberfrax thickness at the sidepanels are changed with 20 %. This means that even when some material parameters are uncertain, due to small information which is available, it won't reduce the thermal performance of the QARMAN satellite to keep the temperatures of the SU components within their limits during re-entry. Also a tolerance of 20 % on the thickness of the SiC and the fiberfrax of the sidepanels and the thickness of the Pyrogel won't affect the thermal behaviour of the components inside SU.

8.1.4 Reached temperature limit during re-entry

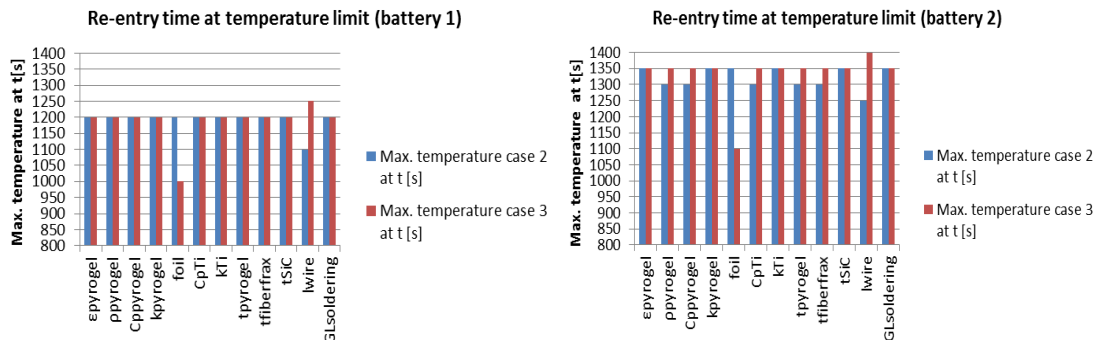


Figure 68: Re-entry time when max. temperatures for case 2 and 3 are reached for battery 1 & 2

The graphs above (see figure 68) gives a good indication that batteries are overheating before the end of the re-entry, namely at $t = 1200$ s for battery 1 and at 1300 s for battery 2. The time difference between battery 1 and 2 is caused by the fact that battery 1 is placed more in the front of the SU (corkside) in comparison with battery 2.

Appendix C.3 gives the results of the re-entry times when the maximum temperature is reached for setted case 2 and 3 for all the other components. The enormous heat fluxes during re-entry are situated in the front and simulation clearly shows that there is a temperature difference between the front nodes and the back nodes of the SU. All the other components are surviving until the end, except for the cases when there is no low emissivity foil used (see red bar foil). Also a reduction of 10 % in the thickness of pyrogel (see bleu bar t_{pyrogel}) reduces the survival time with 100 s for the IMU. The IMU is effected by the thickness of pyrogel, due to its location and design. The IMU is designed as a separate PCB connected to the PCB inside the survival unit. All the other components which are small in comparison with the IRID and the IMU are designed as thermal nodes. Also the wiring length has an influence. If the wires are shorter, in comparison with the initial defined lengths, the thermal resistance reduces and there is more heat conducted inside the SU. Therefore, is the survival time for the batteries reduced. The batteries are more sensitive to changes of the tested parameters, because the batteries have stronger temperature limitations in comparison with the other components inside the SU, namely a max. allowable temperature of 50 °C in comparison with the 70 °C to 85 °C for other components.

The general conclusions drawn from the above described sensitivity analysis are listed below:

- A low emissivity foil should be used at the in- and outside of the survival unit. See the following paragraph 8.1.5

- Correct cabling lengths, which will be known after the QARMAN's implementation tests are preformed, should be implemented in the ESATAN thermal design of QARMAN.
- Tolerances of 10 % on the thickness of Pyrogel for the SU, SiC and fiberfrax for the sidepanels are allowed.
- The uncertainties about materials parameters changing with temperature don't effect the thermal design of the QARMAN satellite.
- The thermal design of the batteries should be updated in the next thermal model, with accurate material properties, connections and volume added. This is done for the thermal model which is used for the DOE.

8.1.5 Adapted battery design

One of the general conclusion mentioned above was about updating the batteries design. The batteries were defined as thermal node with a defined volume and averaged material properties, which were comparable with the properties of a laminated material consisting of plastic and metal. The thermal model of batteries was updated from thermal nodes to realistic designed batteries with properties for a lithium polymer Kokam SLB603870H. The material properties of the mentioned lithium polymer Kokam SLB603870H are listed below [47]:

- Density= 1890 kg/m³
- Specific heat = 1350 J/kg.K
- Conductivity= 1,11 W/m.K
- Emissivity= 0,85

The batteries are pressed against the heat sink (see figure 69) of the PCB inside the survival unit. The thickness of the plates is calculated in such a way that the "heat sink" volume of 24000 mm³ remained the same in comparison with the old version of the thermal design.

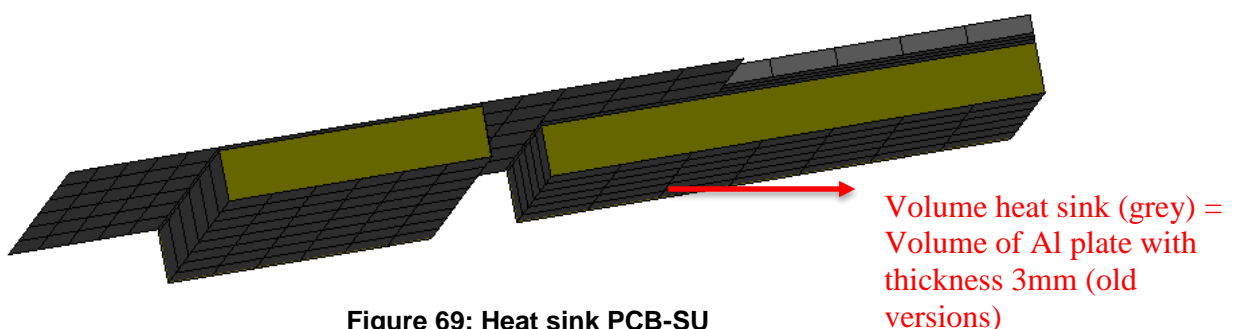


Figure 69: Heat sink PCB-SU

First there were some doubts about the high emissivity value of the outer surface of the batteries found in literature, because most batteries are wrapped in a high reflective foil. Therefore were two simulations performed to know the influence of the batteries temperatures when 2 different outer surface foils where used. The first test case has batteries with a low emissivity foil of 0,05, which is comparable with an aluminium foil. The second test case has batteries with a high emissivity of 0,85 as found in literature [47]. Table 12 presents the results of both simulations.

It can be clearly seen from the following results that the emissivity of the batteries doesn't affect the temperature of the batteries. The following table 12 shows the temperatures of the components inside the SU after 1400 s.

Table 12: Simulation results different $\epsilon_{\text{battery}}$

Component	Temperature [°C]	
	Case 1 $\epsilon_{\text{battery}} = 0.05$	Case 2 $\epsilon_{\text{battery}} = 0.85$
<i>Battery 1</i>	62,22	62,24
<i>Battery 2</i>	58,27	58,31
<i>IMU</i>	66,60	66,68
<i>IRID</i>	64,44	64,48
<i>IRID antenna</i>	53,06	53,14
<i>OBC</i>	68,64	68,65
<i>Regulator</i>	64,34	64,38

8.1.6 Different emissivities SU

Another general conclusion of the screening analysis mentioned above was about the use of low emissivity foil for the survival unit. There were two test cases set for the parameter “Low emissivity foil coated SU”, namely “Low 0,05 ϵ foil in- and outside SU” and “No low 0,05 ϵ foil in- and outside SU”. Both selected cases are rather conservative, therefore is an additional analysis performed to determine to lowest emissivity needed to have the temperatures of the electrical components of the SU within their limits. Some other remarks about the emissivity for the SU should be made, namely:

- The cross-section of a SU with emissivity foils applied on the outer and inner surfaces can be described as follows from the outside to the inside: emissivity foil – titanium SU casing – Pyrogel – emissivity foil. This means that the emissivity foil at the inside of the survival unit is glued on the Pyrogel fabric. The actual QARMAN model has the Pyrogel a negative shape, following the contours of the electronic unit inside the SU (see figure 18). So a foil applied on this Pyrogel creates an electrical path when it is in touch with the PCB. It can be concluded that it is impossible to have a low emissivity foil inside the SU.
- Another problem concerning the use of a low emissivity foil at the outside of the SU is the fact that the outer surface of the survival unit reaches a maximum of 581 °C and 335 °C during re-entry for respectively having the emissivity of the outer foil equal to 0,15 and 0,05. This means that glue which is holding the foil loosens.

The following analysis determines the maximum allowable emissivity of the outer polished surface in order to have the SU electronic components temperatures within their margins during re-entry. Different emissivity values, namely 0.05, 0.10, 0.15, 0.20, 0.25 and 0.30, were used for the outer surface of the SU. This outer surface was considered to be polished. The inner surface had a fixed emissivity value of 0,15 for Pyrogel.

Figure 70 shows that the batteries are still the first components inside the SU which are overheating. Battery 1 which is placed in the front in the direction of the cork overheats after 1100 s, when the outer surface of the titanium survival unit has an emissivity of 0,05. The plot above shows a significant influence of the emissivity of the Ti SU surface. Previous results, where a low emissivity foil of 0,05 was used on both surfaces of the SU, showed that all the components survived up to 1400 s except for battery 1 which survived up to 1200 s and battery 2 up to 1300 s. An emissivity of maximum 0,15 should be achieved, because all the other electronic components beside the batteries don't survive up to the stagnation point at 1200 s when the emissivity of the outer surface of the SU is higher than 0,15.

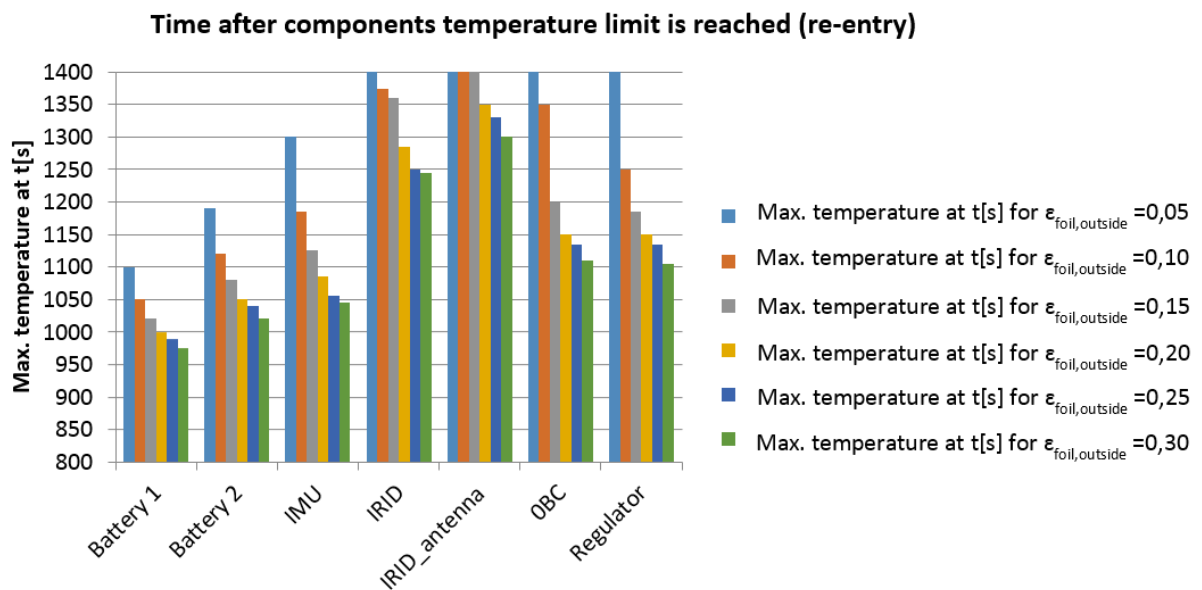


Figure 70: Time when the components inside the SU reaches there limit temperatures

The outcome of this simulation is used for the following presented design of experiments. As stated before, there are 3 significant parameters selected that influence battery 2 temperature. The three selected parameters are the length of electrical wiring, the thickness of Pyrogel used for the insulation of the SU and the emissivity of these 3 parameters are investigated in some more detail in the following DOE. The design of experiments focusses on the temperatures of battery 2, because the batteries have the tightest temperature limits. So improving the thermal design of the QARMAN satellite in order to have the second battery its temperatures within limits automatically improves the thermal design for all the other components inside the survival unit. Focussing the DOE on one component also reduces the complexity of a design of experiments.

8.2 Design of experiments

The design of experiments is based on a factorial design where the effects of two or more factors are studied. One of the problems of the previous performed sensitivity analysis was that there is no possibility to see interactions between factors. The following general explanation applies for 2³-factorial design. This means that there are 3 different factors each with two different levels studied.

8.2.1 Basic principles [48]

The general notion for a factorial design is n^k , with k the number of studied factors and n the number of considered levels for each factor. The following explained basic principles are explained for a 2^3 -factorial design, with A, B and C used as the notation for the three factors. Here are the design factors considered at two levels, namely a high “+” level and a low “-” level. The main effect of the design factor is the average response between the high level and the low level, also explained with equation 8.1. A factorial design with three variables demands a DOE consisting of 8 tests when the impact on the output variables shows a linear behaviour. A quadratic impact on the output variables demands a DOE consisting of more than n^k tests.

The different test cases are summarized in a square matrix, called the design matrix. The treatment combination always has a fixed order in the matrix with the following labels (*I*), *a*, *b*, *ab*, *c*, *ac*, *bc* and *abc*. Table 13 shows the design matrix for a 2^3 -factorial design, with the tested factors A, B and C. The columns of the design matrix are constructed as following: the first column has alternating + and – signs every 2^0 test, the second column has the + and – signs alternating each 2^1 test,... and the j^{th} column had the + and – signs alternating each 2^{j-1} test. The matrix of the factorial effects, see the blue boxed matrix in table 13, with the signs determined as following:

- The signs for the main effects A, B and C are equal to the signs of the associated data mentioned in the design matrix.
- The signs of the remaining columns obtained by multiplying the appropriate columns of the design matrix, except for column I.
- Column I, also called the identity column, contains only “+” signs.

Table 13: Design matrix (red) and matrix of the factorial effects (bleu) for a 2^3 -factorial design

Run	A	B	C	Labels	I	A	B	AB	C	AC	BC	ABC
1	-	-	-	(1)	+	-	-	+	-	+	+	-
2	+	-	-	A	+	+	-	-	-	-	+	+
3	-	+	-	B	+	-	+	-	-	+	-	+
4	+	+	-	ab	+	+	+	+	-	-	-	-
5	-	-	+	C	+	-	-	+	+	-	-	+
6	+	-	+	ac	+	+	-	-	+	+	-	-
7	-	+	+	bc	+	-	+	-	+	-	+	-
8	+	+	+	abc	+	+	+	+	+	+	+	+

The matrix, presented above, makes it possible to calculate the regression model for the 2^3 -factorial design (see equation 8.2).

$$z = \beta_0 + \beta_1 \cdot x_1 + \beta_2 \cdot x_2 + \beta_3 \cdot x_3 + \beta_{12} \cdot x_1 \cdot x_2 + \beta_{13} \cdot x_1 \cdot x_3 + \beta_{23} \cdot x_2 \cdot x_3 + \beta_{123} \cdot x_1 \cdot x_2 \cdot x_3 + \varepsilon \quad (8.2)$$

Where x_1 , x_2 and x_3 are the variables representing the tested factors A, B and C, z is the response value, β are the regression coefficients that need to be defined and ε is a random error term. For the regression coefficients is β_0 the average response in the factorial design, β_i is the regression

coefficient for the main effect x_i , $\beta_{ij(k)}$ corresponds to the interaction effect between both main parameters x_i , x_j and eventually x_k .

The coefficients β_i , β_{ij} and β_{ijk} are determined with the following equations 8.3 up to 8.6. All products of the values in the corresponding x_i , x_{ij} and x_{ijk} -columns with their associated response value are summed and divided by the total number of test combinations m . For β_0 is the same calculation performed on the I-column.

$$\beta_0 = \frac{1}{m} \cdot \sum_{t=1}^m I_t \cdot y_t \tag{8.3}$$

$$\beta_i = \frac{1}{m} \cdot \sum_{t=1}^m x_{it} \cdot y_t \tag{8.4}$$

$$\beta_{ij} = \frac{1}{m} \cdot \sum_{t=1}^m x_{it} \cdot x_{jt} \cdot y_t \tag{8.5}$$

$$\beta_{ijk} = \frac{1}{m} \cdot \sum_{t=1}^m x_{it} \cdot x_{jt} \cdot x_{kt} \cdot y_t \tag{8.6}$$

The graphical representation of the regression model presented by equation 8.2 is called a response surface plot. The eight treatment combinations are displayed in the cube presented in figure 71.

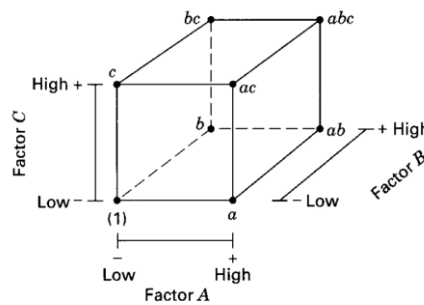


Figure 71: Geometric view of a 2³ factorial design

The left at the top of figure 72 illustrates the graphical meaning of the main effect of factor A for example. There are four points of comparison between the left and right grey face, namely the vertices. The following example explains the calculation of the main effect of factor A, where:

- The response value changes with $a - (1)$, $ab - b$, $ac - c$ and $abc - bc$, when factor A varies from -1 to +1.
- The averaged value of these previous mentioned response values is equal to $\frac{(a-(1))+(ab-b)+(ac-c)+(abc-bc)}{4}$. This averaged value is divided by 2 at its term, because the factor A varies from -1 to +1. This means that the main effect of factor A can be written as following:

$$\beta_1 = \frac{(a-(1))+(ab-b)+(ac-c)+(abc-bc)}{8} = \frac{-(1)+a-b+ab-c+ac-bc+abc}{4}$$

This last mentioned equation for the calculation of β_1 can easily be calculated with equation 8.4, where the values for variable x_{it} correspond to the yellow marked column in table 13.

The main effects for factor B and C are calculated by the same method. The same philosophy is also used to calculate the interaction effects β_{12} , β_{13} , β_{23} and β_{123} , with the only difference that the vertices are located at the intersecting grey surfaces.

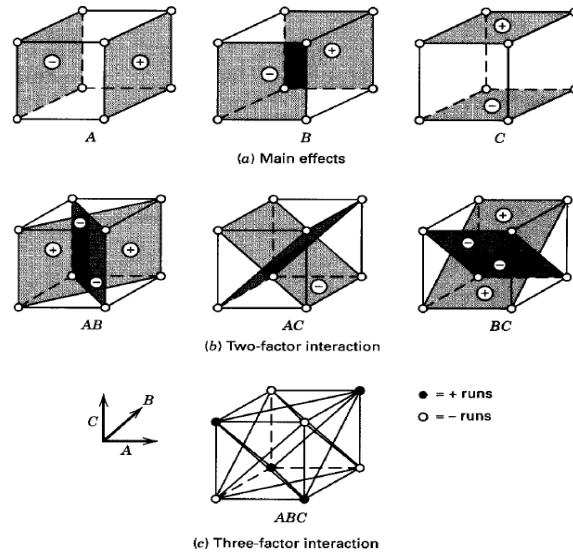


Figure 72: Geometric presentation of contrasts corresponding to the main effects and interactions in the 2^3 design

8.2.2 Analysis of experiments

In the previous paragraph 8.2.1, it was explained how to calculate the effects $\beta_0, \beta_1, \beta_2, \beta_3, \beta_{12}, \beta_{13}, \beta_{23}$ and β_{123} by means of the matrix calculation. For the performed DOE are the averaged values of the temperatures of the four sides of battery 2 used as the response value z . Table 14 shows a shortened version of the results presented in appendix C.4.

Table 14: Results DOE

Test	Test case discription			$Z_{av.}$ [°C]	S_i^2	effect i	β_i	$t_i = \beta_i/S_{effect}$	$ t_i < 2.12$	Z=
	X_1 (ϵ_{foil})	X_2 (I_{wire})	X_3 ($t_{pyrogel}$)							
1	0,15	-20%	-1mm	94,62	4,33	$\beta_0 =$	94,03	253,64	253,64	94,03
2	0,3	-20%	-1mm	113,22	6,23	$\beta_1 =$	8,59	23,18	23,18	8,59
3	0,15	+20%	-1mm	89,91	4,86	$\beta_2 =$	-2,79	-7,52	7,52	-2,79
4	0,3	+20%	-1mm	108,41	6,92	$\beta_3 =$	-7,51	-20,27	20,27	-7,51
5	0,15	-20%	+1mm	82,50	2,41	$\beta_{12} =$	0,34	0,91	0,91	
6	0,3	-20%	+1mm	96,92	3,92	$\beta_{13} =$	-0,68	-1,84	1,84	
7	0,15	+20%	+1mm	74,71	2,24	$\beta_{23} =$	-0,41	-1,10	1,10	
8	0,3	+20%	+1mm	91,93	4,27	$\beta_{123} =$	0,36	0,98	0,98	

$$\Sigma = 35,18$$

The parameter estimates β_i are calculated, but which of these should be retained to construct the regression model for the 2^3 -factorial design (see equation 8.2)? To answer this previous question, a null hypothesis should be performed. The sample variance S_i^2 is calculated for each test combination i . For the estimation of the variance (see equation 8.7) are two assumptions made, namely that the variance of each test combination is constant and all observations are independent from each other.

$$S_i^2 = \frac{(z_{j1}-\bar{z}_j)^2 + (z_{j2}-\bar{z}_j)^2 + \dots + (z_{jn}-\bar{z}_j)^2}{n-1} \quad (j = 1, 2, \dots, m) \quad (8.7)$$

With \bar{z}_j the averaged value of the j^{th} test combination, Z_{jk} the response value for the experiment of the j^{th} test combination, n is the number of times that a certain test combination is repeated (here $n=4$, because the temperatures of the four sides of battery 2 is measured) and m the number of test combinations (here $m=8$). For each test combination is a sample variance S_i^2 calculated.

There has been assumed that the variances on each response value is constant and that the test combinations were independent from each other. Therefore are the observed variances for all 8 test combinations independent estimated for the variance of the error term. The best estimate to calculate the variance of the error is averaging the observed variances (see table 14). The following equation 8.8 gives the value for the variance of the error term.

$$S^2 = \frac{1}{m} \sum_{i=1}^m S_i^2 = \frac{1}{8} (4,33 + 6,23 + 4,86 + \dots + 4,27) = 4,40 \quad (8.8)$$

The variance on the calculated effects β_i is calculated with equation 8.9.

$$S_{effect}^2 = \frac{S^2}{m.n} = \frac{4,40^2}{8.4} = 0,14 \quad (8.9)$$

It is possible to perform a statistical hypothesis test, when the previous calculated number for S_{effect}^2 and the values for the effects β_i are known. The hypothesis test gives an indication if the effect is significant different from zero. The null hypothesis states that a certain effect is negligible when:

$$H_0: \mu_{effect} = 0$$

When this previous mentioned null hypothesis is rejected, is the following alternative hypothesis valid:

$$H_0: \mu_{effect} \neq 0$$

It is important to know the distribution of the estimators of the effect, in order to carry out such a hypothesis test. A normal distribution with a mean value μ_{effect} equal to zero and a standard deviation of σ_{effect} is assumed. The assumption of the normal distribution is acceptable, because the estimates are a linear combination of the observations which are according to the central limit theorem approximately normally distributed. The probability that a particular effects β_i is significantly different from zero is calculated by the transformation to the standard normal distribution (see equation 8.10).

$$Z_i = \frac{\beta_i - \mu_{effect}}{\sigma_{effect}} = \frac{\beta_i}{\sigma_{effect}} \quad (8.10)$$

The real value for σ_{effect} is usually not known and therefore is S_{effect} used to estimate the value of σ_{effect} .

The t-distribution is used instead of the normal distribution, because the standard deviation of the samples S_{effect} is used instead of the standard deviation of de population σ_{effect} for the following calculations. The t-distribution is symmetrically around the mean, with its spreading depends on

the degrees of freedom. A t-distribution has a larger spreading in comparison with the spreading around the mean value for a normal distribution. The t-distribution approaches a normal distribution as the sample size n goes to infinity. The null hypothesis is tested with the t-distribution. For example, the main effect β_1 is tested if the effect is significantly different from zero by using equation 8.10.

$$t_1 = \frac{\beta_1 - \mu_{effect}}{S_{effect}} = \frac{94,03}{\sqrt{0,14}} = 253,64$$

This previous calculated t-value is compared with the critical t-value. The critical t-value depends on the significance level α and the degrees of freedom. For 8 test combinations, with each test repeated 4 times, is the degrees of freedom equal to $m(n - 1) = 8 \cdot 3 = 24$.

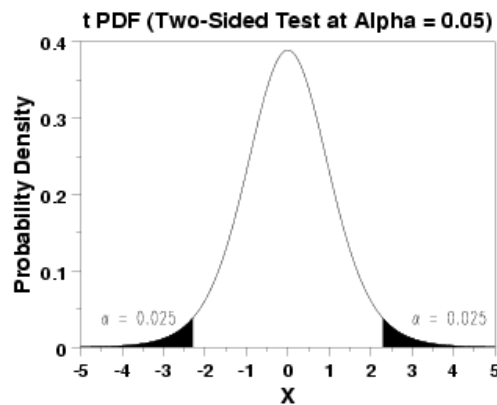


Figure 73: Two-sided T-test with significance level $\alpha=0,05$ [49]

A significance level of 0,05 has been chosen. For a two-side T-test, as illustrated in figure 73, is $1 - \alpha/2 = 1 - 0,05/2 = 0,025$. If the absolute value for the T-test statistic t_i is greater than the critical t-value 2,064 for t-distribution with a 0,975 (=1-0,025) significance level and 24 degrees of freedom, then is the null hypothesis rejected. The rejection of the null-hypothesis practically means that an effect is significant different from zero, which also implies for the mean effect β_1 . After performing the T-test for the 8 effects β_i , are only the effects β_0 , β_1 , β_2 and β_3 withheld. This makes it possible to calculate the regression model for the 2^3 -factorial design (see equation 8.11).

$$z = 94,03 + 8,59 \cdot x_1 - 2,79 \cdot x_2 - 7,51 \cdot x_3 + \varepsilon \quad (8.11)$$

Where the variables x_1 , x_2 and x_3 are respectively the variables representing the tested factors ε_{foil} , I_{wire} and $t_{pyrogel}$. z is equal to the temperature response of battery 2.

The uncertainty on the response value z , also called the error term ε , is estimated with the variance of the error term S^2 . The response value z is normally distributed with a standard deviation $S = \sqrt{4,40} = 2,10$. It can be stated that with a certainty of 95%, that the response value z is within the following interval (see equation 8.12).

$$Z \pm 2 \cdot S = Z \pm 2 \cdot 2,10^\circ C = Z \pm 4,20^\circ C \quad (8.12)$$

8.2.3 Results

The contour plot shows the response surface as a two-dimensional view, where all the points with the same temperature response are connected to form a contour line. The surface plot is shown in a three-dimensional view. Equation 8.11 shows the regression model for the elaborated design of experiments, where different input parameters were studied the influence the satellites SU temperature during re-entry. The regression model is a first order model which contains only main effects and no interaction effects, therefore will be the fitted surface plot a plane and the contour plot will have straight lines.

Figure 74 shows the relationship between the length of the electrical wires, the thickness of Pyrogel and the temperature response for a survival unit with an emissivity value of 0,15 for the outer surfaces.

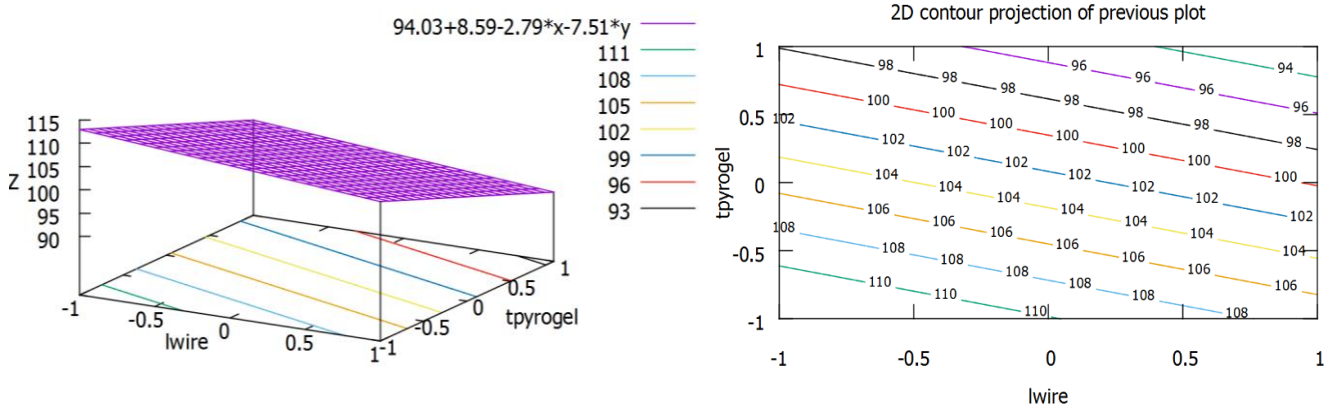


Figure 74: Surface plot (left) and contour plot (right) for Z = temperature response of battery 2 [°C], x = x₂ = l_{wire}, y = x₃ = t_{pyrogel} and SU with emissivity of 0,15 for the outer surfaces (=x₁)

Figure 75 shows the relationship between the length of the electrical wires, the thickness of Pyrogel and the temperature response for a survival unit with an emissivity value of 0,05 for the outer surfaces.

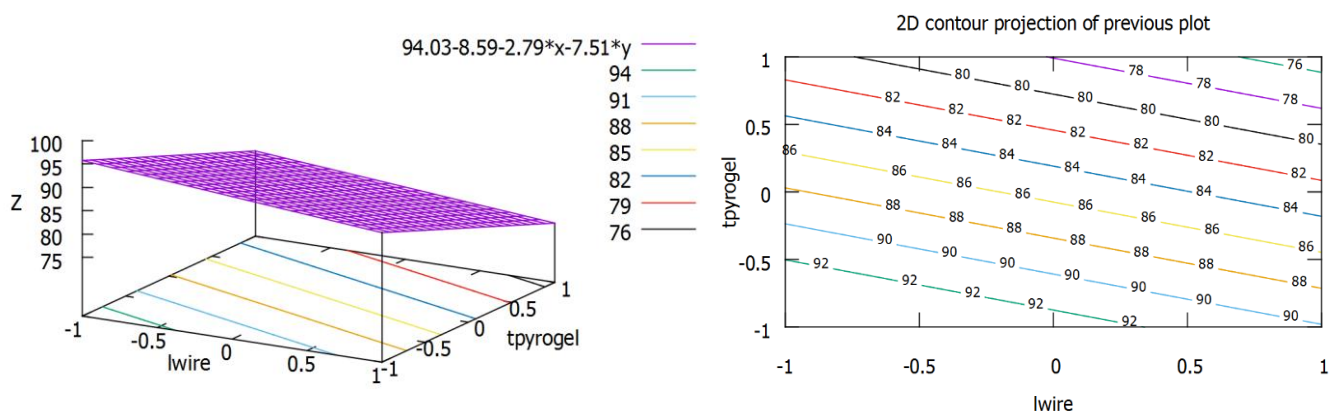


Figure 75: Surface plot (left) and contour plot (right) for Z = temperature response of battery 2 [°C], x = x₂ = l_{wire}, y = x₃ = t_{pyrogel} and SU with emissivity of 0,05 for the outer surfaces (=x₁)

Both presented surface and contour plots (see figures 74 and 75) are the results of a design of experiments, conducted for a QARMAN-satellite re-entry case where the temperatures of battery 2 were registered 1400s after the re-entry started. The x- and y-axis of figure 74 and 75 are

respectively the input variables length of the electrical wires and thickness of Pyrogel, where the input variables have coded values. The coded values of -1 and 1 for the length of the electrical wires are respectively equal to $l_{\text{initial}} - 20\%$ and $l_{\text{initial}} + 20\%$, where the variable l_{initial} refers to the nominal lengths of the wires estimated with the help of the 3D model of the QARMAN satellite. The coded values of -1 and 1 for the thickness of Pyrogel are respectively equal to the thickness of the Pyrogel varying with -1 and +1 mm.

Both graphs, shown in figures 74 and 75, clearly show a temperature reduction when the length of the electrical wires increase. This means that the real length of the electrical wires, which are most likely longer than the estimated wire lengths of the straight connection in the 3D model, influences the battery temperature in a positive way. An increase of the electrical wire lengths cause a temperature increase of $2,79\text{ }^{\circ}\text{C}$, which is also the less influencing parameter of the 3 studied parameters ϵ_{foil} , l_{wire} and t_{pyrogel} in this 2^3 -factorial design of experiments.

A reduction of 1mm of the thickness of pyrogel causes a temperature increase of $7,51\text{ }^{\circ}\text{C}$. This increase in temperature by $7,51\text{ }^{\circ}\text{C}$ is larger than the uncertainty (see equation 8.12) of $4,20\text{ }^{\circ}\text{C}$ on the temperature response of battery 2. A reduction in the thickness of Pyrogel causes a visible influence on the battery's temperature and therefore it is recommended to check the thickness of the Pyrogel with the CAD drawings after the negative shape (see figure 18) of the Pyrogel insulation is manufactured. Pyrogel has been chosen as an insulation material for the survival units for the QARMAN satellite. This Pyrogel insulating material is an Aspen Aerogels product, formed by reinforcing the aerogel with non-woven glass fibre batting. The Aspen Aerogels Pyrogel blanket can be easily shaped by using scissors and knives. Aspen Pyrogels are friable and therefore are those materials causing dust by shaping, which could contaminate the electronics inside the survival units. The negative shape of the SU insulation is formed by gluing different layers of Pyrogel. Pyrogel blankets come only in thicknesses of 5 and 10 mm, therefore it will be difficult to have an accurate shaped insulation. A better accuracy of the negative shape for the SU insulation can be obtained by machining instead of manual cutting. Therefore another type of aerogel is proposed, namely Microtherm®. Microtherm® has comparable thermal and materials properties in comparison with Pyrogel®, because both materials are silica based aerogels. The Microtherm® board can be machined with tolerances ranging from 0,75 to 1 mm [50].



Figure 76: Aerogels (left: machined Microtherm® and right: Pyrogel®)

Battery 2 has a temperature of $102,62 \pm 4,20\text{ }^{\circ}\text{C}$ at the end of the re-entry when the outer surface of the survival unit has an emissivity of 0,15. The length of the electrical wires and thickness of

Pyrogel are considered to be nominal. This value of $102,62\text{ }^{\circ}\text{C}$ can be found by reading the contour plot of figure 74 for l_{wire} and t_{pyrogel} equal to 0 or using equation 8.11. The temperature for battery 2 at the end of re-entry is equal to $85,44 \pm 4,20\text{ }^{\circ}\text{C}$ for a case with the outer surface of the survival unit having an emissivity of 0,05. Again, this temperature of $85,44\text{ }^{\circ}\text{C}$ can be found by reading the contour plot of figure 75 for l_{wire} and t_{pyrogel} equal to 0 or using equation 8.11. This means that an emissivity increase of 0,10 for the outer surface, increases the temperature of battery by $17,18 \pm 4,20\text{ }^{\circ}\text{C}$. Therefore a highly titanium polished surface is recommended, in literature it has been found that emissivities of 0,08-0,19 for polished titanium are possible [51]. A machined titanium piece has no air gaps in comparison with a 3D-printed titanium piece for the survival units, no air gaps mean that a lower emissivity can be achieved by polishing the piece. Therefore is a machined titanium piece more preferable than a 3D-printed one. There has also been considered to use an aluminized Kapton® film or an aluminium film to coat the outer surface of the survival unit, in order to approximate the low emissivity of 0,05 for a highly polished aluminium. These two previous mentioned coatings won't withstand the re-entry temperatures. Therefore it should be understand what the effects are when a coating of the survival unit burns away, because there is a possibility that the surface becomes black with an increased emissivity of the outer surface. It better to take no risk, because the longer the survival units survives during re-entry, the more scientific data can be captured. Therefore a highly polished titanium is a safer engineering choice.

Conclusion and recommendations

In this presented thesis, the thermal design of the QARMAN satellite has been developed in detail. A Conductor Interface Calculator was developed to determine the thermal resistance of frequently used conductive interfaces, such as contact zones, bolted joints, spacers, soldering of electronic components and bundles of electrical wiring, in a systematic way. The new added heat paths, defined by the previous mentioned conductive interfaces, make the thermal ESATAN-TMS more realistic. But it also means that there is more heat conducted through the subsystems and components. It has been presented that the 3 different thermal cases, namely the re-entry case, the thermal hot and cold cases, have a strong impact on the thermal design of the QARMAN satellite. In the old models were more PCBs stacked on top of each other, the PCBs were highly packed together and the component's heat dissipation caused high temperatures in the stack. The components which need to survive until the end of the re-entry phase are now also placed inside titanium survival units filled with Pyrogel. The Pyrogel is a lightweight and low conductive material.

In the cold case, simulations showed that all the components were within their temperature limits. The re-entry phase and the hot orbital phase caused nearly all the issues: involving components heating up too fast and reaching their maximum temperature limits.

The components which need to function until the end of the re-entry mission, namely the OBC, the Iridium modem, both batteries, the IMU, all the needed regulators, are placed in one main survival unit in the middle of the satellite. All these previous mentioned components, except for the batteries, survive until the satellite crashes. Battery 1 and 2 respectively reach their temperature limit of 50 °C after 1150 s and 1200s, before the satellite crashes. Nevertheless is this already a big achievement in comparison with old results where the components only survived for 2 – 4 minutes during the re-entry. The XPLDAQ component, placed in the front survival unit, survives up to 1080 s after re-entry (which corresponds with an altitude of about 80km). The spectrometer reaches its maximum temperature of 50 °C after 950 s, where a few minutes are sufficient to achieve the tasks.

Again, all the components inside the satellite except for the batteries remain within their defined temperature limits for the hot orbital cases.

A screening analysis and a design of experiments (DOE) indicated 3 main factors which significantly effect the components' temperatures inside the SU, namely the outer surface SU emissivity, the SU insulation thickness and the length of electrical wiring. The influence of the effects were ordered from large to small. An emissivity increase of 0,10 for the outer surface, increases the temperature of battery 2 by $17,18 \pm 4,20$ °C. Therefore a highly polished surface with an emissivity factor close to 0,08 is recommended. A machined titanium piece has no air gaps in comparison with a 3D-printed titanium piece for the survival units, no air gaps mean that a lower emissivity can be achieved by polishing the piece. No low emissivity coating applied on the inside of the insulation material of the survival unit was considered for the thermal design of the

QARMAN satellite used for the DOE. On the other hand simulations with low emissive coatings used on those inner surfaces, showed to have positive influence on the batteries temperatures. Instead of polishing the titanium surfaces of the survival unit, low emissive foils or an aluminized Kapton® film could be used. So it is recommended to research the use of a low emissivity coating for the in- and external surfaces of the survival unit. The behaviour of those coatings at high temperatures should be tested. Because losing a coating and have a high emissive surface remaining is no option.

Another significant effect on the temperatures of the components inside the survival unit is caused by the thickness of Pyrogel. Pyrogel is the insulation material used for survival units. A reduction of 1mm of the thickness of pyrogel causes a temperature increase of 7,51 °C. Therefore it is recommended to check the thickness of the Pyrogel with the CAD drawings after the negative shape is manufactured. Another measure could be taken by using Microtherm®. Microtherm® has comparable thermal and materials properties in comparison with Pyrogel®, but has the advantage that it can be machined with an accuracy of 0,75 to 1mm. Those accuracies are higher, in comparison with a manually cut Pyrogel.

The third significant parameter which has been defined, is the length of electrical wires.

It is recommended to validate the model by performing a large scale test in a vacuum oven. This large scale test could provide important data for the validation of the thermal model made with ESATAN-TMS. By closer investigation of the material properties, especially for high-end materials such as the SiC, the used Pyrogel, 3D printed titanium,... the thermal model should be updated and re-iterated. Some more investigation should be done about the emissivity for the surfaces of the survival unit. In an ideal case, when low emissivity surface could be applied on the insulation material of the survival units, the temperatures of the components inside the survival units could be further reduced and the temperatures of the batteries during the hot orbital cases could be reduced. Another issue which could be investigated some more, is to have fiberfrax insulation paper between the front survival unit housing the XPLDAQ and the front-back ceramics plate. The fiberfrax paper could function as a thermal barrier between the front survival unit and front-back ceramic plate.

References

- [1] QB50, “The project,” 2014. [Online]. Available: www.qb50.eu. [Accessed 23 September 2014].
- [2] C. O. Asma, “QARMAN: QB50 Qubesat for Aerothermodynamic Research and Measurement on Ablation,” Von Karman Institute, Sint-Genesius-Rode, 2013.
- [3] T. Azzarelli, “International Regulations for Nano/Pico Satellites,” in *ITU Seminar*, Cyprus, 2014.
- [4] CubeSat Kit, “3D CAD Design,” Pumpkin, Inc., 10 october 2014. [Online]. Available: <http://www.cubesatkit.com/content/design.html>. [Accessed 23 September 2014].
- [5] V. Van der Haegen, I. Sakraker, T. Scholz, G. Baillet, L. Dell'Ecle and E. Umit, “QARMAN deliverable D2AB Mission/System preliminary design,” Von Karman Institute, Sint-Genesius Rhode, 2014.
- [6] G. Baillet and J. Muylaert, “Re-entsat, an atmospheric triple unit re-entry cubesat,” in *9th annual CubeSat developer's workshop*, San Luis Obispo, 2012.
- [7] V. Van der Haegen, I. Sakraker, T. Scholz, G. Baillet, L. Dell'Ecle and E. Umit, “QARMAN Deliverable D1AB Mission/System Objectives and Requirements,” von Karman Institute for Fluid Dynamics, Rhode Saint Genèse, 2014.
- [8] V. Van der Haegen, I. Sakraker, T. Scholz, G. Baillet, L. Dell'Ecle and E. Umit, “QARMAN Deliverable D2AB Mission/System Preliminary design,” von Karman Institute for Fluid Dynamics, Rhode Saint Genèse, 2014.
- [9] W. M. Rohsenow and J. P. Hartnett, *Handbook of heat transfer*, New York: McGraw-Hill book company, 1973.
- [10] W. M. Rohsenow, J. P. Hartnett and Y. I. Cho, *Handbook of heat transfer*, Boston: Mc Graw Hill, 1998.
- [11] J. H. Lienhard IV and J. H. Lienhard IV, *A heat transfer textbook*, Cambridge: Phlogiston Press, 2008.
- [12] R. Tanghe, “Warmteoverdracht deel I - Tekst,” Acco, Leuven, 2014.
- [13] V. Van der Haegen and J.-M. Buchlin, “An introduction to infrared thermography,” in *Lecture series VKI: Introduction to measurement techniques*, Rhode Saint Genèse, 2014.
- [14] H. J. Allen and A. J. Eggers, “A study of the motion and aerodynamic heating of missiles entering the earth's atmosphere at high supersonic speeds,” National Advisory Committee For Aeronautics, Washington, 1953.
- [15] J. D. Anderson, “Chapter 1 Aerodynamics: Some introductory thoughts,” in *Fundamentals of aerodynamics*, Singapore, MC Graw Hill, 2011, p. 11.
- [16] Federal Aviation Administration, “4.1.7 Returning from space: Re-entry,” 2014. [Online]. Available: https://www.faa.gov/other_visit/aviation_industry/designees_delegations/designee_types/a/me/media/Section%20III.4.1.7%20Returning%20from%20Space.pdf. [Accessed 1 December 2014].
- [17] Federal Aviation Administration, “4.1.4 Describing Orbits,” [Online]. [Accessed 1 November 2014].
- [18] M. Hackworth, “Weather & climate Ohio State University,” [Online]. [Accessed 1 November 2014].
- [19] D. G. Gilmore, *Spacecraft thermal control handbook*, vol. Volume 1: Fundamental technologies, California: The aerospace press, 2002.
- [20] L. Jacques, “QARMAN Thermal Analysis Report,” Université de Liège, Liège, 2014.

- [21] J. Menglin and L. Shunlin, "An improved land surface emissivity parameter for land surface models using global remote sensing observations," *Journal of climate*, no. Volume 19, pp. 2897-2881, 2006 June 2006.
- [22] A. Bejan and A. D. Kraus, *Heat transfer handbook*, New Jersey: John Wiley & Sons, 2003.
- [23] M. C. J. T. P. Yovanovich, "Calculating interface resistance," Microelectronics heat transfer laboratory department of mechanical engineering university of Waterloo, [Online]. Available: www.thermalengineer.com/library/calculating_interface_resistance.htm. [Accessed 4 November 2014].
- [24] B. Mikic, "Thermal contact conductance; theoretical considerations," *International Journal of Heat and Mass Transfer*, vol. 17, no. 2, pp. 205-214, 1974.
- [25] B. M. Korevaar and G. den Ouden, "3.12 Hardheid," in *Meraalkunde deel 1*, Delft, Delftse Universitaire Pers, 2005, p. 57.
- [26] D. W. Hahn and O. M. Necati, "Heat conduction fundamentals," in *Heat Conduction, 3rd Edition*, Hoboken, John Wiley & Sons, 2012, p. 23.
- [27] M. B. H. Mantelli and M. M. Yovanovich, "Compact analytical model for overall thermal resistance of bolted joints," *International Journal Heat Mass Transfer*, vol. Vol. 41, no. No. 10, pp. 1255-1266, 1998.
- [28] Secretariat DIN, "Aerospace-Determination of coefficients of friction of bolts and nuts under specific conditions-Complementary element," 2011.
- [29] Tochnici Mfg. CO., "Technical Data," 2007. [Online]. Available: <http://tohnichi.jp/english/technical/index.html>. [Accessed 23 November 2014].
- [30] A. K. J. Hasselström and U. E. Nilsson, "Thermal contact conductance in bolted joints," Chalmers University of Technology, Gothenburg, 2012.
- [31] S. Lee, S. S. Van Au and K. P. Moran, "Constriction/spreading resistance model for electronics packaging," *ASME*, vol. XL, no. 4, pp. 199-206, 1995.
- [32] Hittite, "Thermal management for surface mount components," Hittite Microwave Corporation, Chermersford, 2012.
- [33] IPC, "Joint Industry Standard, Space applications electronic hardware addendum to J-STD-001D requirements for soldered electrical and electronic assemblies," IPC Technical Activities Executive Committee, Illinois, 2006.
- [34] T. Pola, T. Häkkinen, J. Hännikäinen and J. Vanhala, "Thermal performance analysis of 13 heat sink materials suitable for wearable electronics applications," *Science and Technology*, vol. III, no. 3, pp. 67-73, 2013.
- [35] U. Ertan, V. d. H. Vincent, S. Thorsten, T. Paride and B. Gilles, "QARMAN: An atmospheric entry experiment on cubesat platform," in *8th European Symposium of Aerothermodynamics for space vehicles*, Lisbon, 2015.
- [36] P. Testani, "QARMAN Thermal Analysis Report," Von Karman Institute, Rhode-Saint-Genève, 2014.
- [37] Astrodev, "AstroDev Helium Radios," Astronautical Development LLC, Arizona, 2009.
- [38] Sarantel Ltd., "SL3105SP Overmoulded Iridium Antenna," Sarantel Ltd., Willenborough, 2012.
- [39] Clyde Space, "SmallSat Reaction Wheel," 2015. [Online]. Available: http://www.clyde-space.com/cubesat_shop/smallsat_subsystems/366_smallsat-reaction-wheel. [Accessed 14 Mai 2015].

- [40] Aspen Aerogels, “Product data sheet Pyrogel XT-E,” 2015. [Online]. Available: http://www.aerogel.com/_resources/common/userfiles/file/Data%20Sheets/Pyrogel_XT-E_DS.pdf. [Accessed 3 February 2015].
- [41] Aspen Aerogels, “Product data sheet Pyrogel 6650,” 2010. [Online]. Available: <http://www.insulationfabricators.com/downloads/data-sheets/aspen-aerogel-pyrogel-6650-ds.pdf>. [Accessed 3 February 2015].
- [42] Solar AC, “Table of absorptivity and emissivity of common materials and coatings,” 26 July 2001. [Online]. Available: <http://www.solarmirror.com/fom/fom-serve/cache/43.html>. [Accessed 2015 February 3].
- [43] READE advanced materials, “Titanium Metal & sponge / powder,” 20 July 2009. [Online]. Available: <http://www.reade.com/Products/Elements/titanium.html>. [Accessed 3 February 2015].
- [44] LayerWise, “Material data sheet: Titanium grade 1,” LayerWise, Leuven, 2015.
- [45] United States EP Agency, “Volume III- Part A, Process for conducting probabilistic risk assessment,” in *Risk assessment guidance*, Washington DC, EP Agency, 2001, pp. A-13.
- [46] B. H. Lindqvist, “Factorial experiments at two levels,” Norwegian University of Science and Technology, Trondheim, 2010.
- [47] R. Gojon, “Detailed thermal design of OUFTI-1 CubeSat,” University of Liège - Centre Spatial de Liège, Liège, 2012.
- [48] D. C. Montgomery, *Design and analysis of experiments-5th ed.*, New York: John Wiley & Sons, Inc. , 2001.
- [49] NIST/SEMATECH, *E-handbook of Statistical Methods*, Colorado: U.S. Department of Commerce, 2013.
- [50] Microthermgroup, “Standard Tolerances on measurements of products,” 17 Mai 2013. [Online]. Available: http://www.microthermgroup.com/high/EXEN/assets_db/ITEMSKEYWORDS3/items/documents/Standard_tolerances_High_temp_Microporous_EN_20141007.pdf. [Accessed 9 Mai 2015].
- [51] Mastercool, Inc., “Infrared Emissivity - Metals,” 2013. [Online]. Available: <http://www.mastercool.com/media/emissivity-metals.pdf>. [Accessed 9 Mai 2015].
- [52] G. Baillet, I. Sakraker, T. Scholz and J. Muylaert, “Qubesat for Aerothermodynamic Research and Measurement on Ablation,” von Karman Institute for Fluid Dynamics, Rhodes-Saint-Genève.

Appendix A

Calculation of the simplified thermal model of the QARMAN satellite

The calculations for the heat balance is based on the QARMAN satellite model with folded solar panels in an orbital cold case. One side of the satellite is facing the earth.

A.1. Steady state calculation

The QARMAN satellite is a 3 unit satellite, simplified illustrated in figure 77 below.

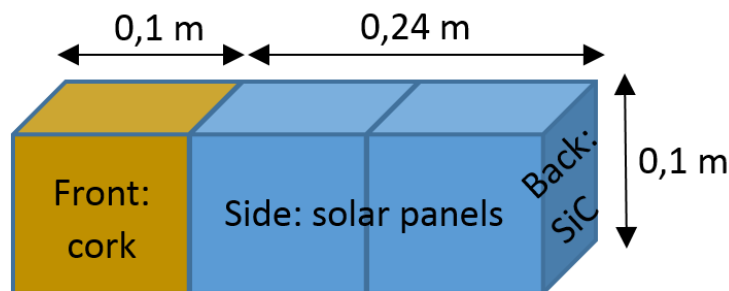


Figure 77: Simplified QARMAN model

The satellites total area $A_{sat} = 0,34m \cdot 0,1m \cdot 4 + 0,1m \cdot 0,1m \cdot 2 = 0,156m^2$.

The following parameters are given:

Table 15: Given parameters for the simplified thermal calculations

Environmental parameters			
	Max. value	Min. value*	Units
I_{sun}	1414	1368	[W/m ²]
<i>Albedo flux</i>	0,4	0,3	[-]
I_{earth}	275	246,5	[W/m ²]
T_{space}	3	3	[K]

Constants			
Mass of the earth	M_e	$5,97 \cdot 10^{24}$	[kg]
Gravity constant	γ	$6,67 \cdot 10^{-11}$	[Nm ² /kg ²]
Radius of the earth	R_e	6378	[km]

Orbital parameters			
Altitude of the satellite	H	380	[km]
Declination of the sun	δ_s	23,45	[°]
Orbit inclination	i	98	[°]
Right ascension of the ascending node	Ω	0	[°]
Right ascension of the sun	α_s	0	[°]

Material properties			
• Solar cells			
Optical properties	$\alpha_{sun,solarcell}$	0,91	[-]
	$\epsilon_{IR,solarcell}$	0,88	[-]
Bulk property	$Cp_{solarcell}$	700	[J/kg.K]
• MLI TPS sidepanels			
Optical properties	$\alpha_{sun,fiberfrax}$	0,3	[-]
	$\epsilon_{IR,fiberfrax}$	0,9	[-]
	$\alpha_{sun,SiC}$	0,775	[-]
	$\epsilon_{IR,SiC}$	0,87	[-]
Bulk properties	$Cp_{fiberfrax}$	1115	[J/kg.K]
	Cp_{SiC}	1086	[J/kg.K]
• Ablation protection (cork)			
Optical properties	$\alpha_{sun,cork}$	0,55	[-]
	$\epsilon_{IR,cork}$	0,77	[-]
Bulk property	Cp_{cork}	2100	[J/kg.K]
• Other materials			
Bulk properties	Cp_{Ti}	523	[J/kg.K]
	Cp_{PCB}	2284	[J/kg.K]

Solar panel efficiencies			
Solar panel efficiency	η_{panel}	0,3	[-]
Charging efficiency	η_{charge}	0,9	[-]

*Only the minimum environmental parameters are used for the following “cold case” calculations.

Table 16: Total dissipated power for the different orbital cases (light grey column - used for this example calculation)

Component	Dissipated power [W]			
	Hot Case		Cold Case	
	Folded	Deployed	Folded	Deployed
EPS1	0,0625	0,0625	0,0625	0,0625
EPS2	0,0187	0,0187	0,0187	0,0187
OBC	0,1	0,1	0,1	0,1
COMM V/UHF RX	0,3	0,3	0,3	0,3
COMM V/UHF TX	0,0298	0,0298	0	0
COMM V/UHF BEACON	0,15	0,15	0,15	0,15
GPS	1	1	0	0
XPL DAQ	0	0	0	0
AeroSDS	0,07	0,07	0	0
ADCS1 (CubeControl)	0,114	0,114	0,114	0,114
ADCS3 (CubeComputer)	0,336	0,336	0	0

Magnetorquer	0,172	0	0	0
Reaction Wheel	0,125	0	0	0
TOTAL [W]	2,4780	2,1810	0,7452	0,7452

The satellites temperature is calculated by solving the heat balance, namely (see equation 4.1):

$$\dot{Q}_{in} = \dot{Q}_{out}$$

$$\dot{Q}_{elect} + \dot{Q}_{albedo} + \dot{Q}_{sun} + \dot{Q}_{earth} = \dot{Q}_{sat, earth} + \dot{Q}_{sat, space}$$

With the elements used for the calculation of the heat balance listed below.

• **Heat dissipated by electronic components** $\dot{Q}_{elect} = 0,7452 \text{ W}$

• **\dot{Q}_{albedo} reflected sunlight by the earth's surface** = $\alpha_{sun} \cdot albedo_{flux} \cdot A_{sat} \cdot F_{earth-sat} \cdot I_{sun}$

Only one side of the satellite receives the solar rays reflected by the earth's surface. The solar panels folded against the TPS sidepanels of the satellite is considered to be one multi-layered surface, consisting of fiberfrax, solarcells and silicon carbide. Therefore are averaged values calculated for the solar absorptivity α_{sun} and the IR emissivity ε_{IR} of the multi-layered surface.

$$\alpha_{sun,ML \text{ sidepanels}} = \frac{2 \text{ mm}}{7 \text{ mm}} \cdot 0,91 + \frac{3 \text{ mm}}{7 \text{ mm}} \cdot 0,30 + \frac{2 \text{ mm}}{7 \text{ mm}} \cdot 0,775 = 0,610$$

$$\varepsilon_{IR,ML \text{ sidepanels}} = \frac{2 \text{ mm}}{7 \text{ mm}} \cdot 0,88 + \frac{3 \text{ mm}}{7 \text{ mm}} \cdot 0,90 + \frac{2 \text{ mm}}{7 \text{ mm}} \cdot 0,87 = 0,886$$

The solar panels absorb 88% of the earth's reflected solar energy. This solar energy is converted to chemical energy to charge the batteries. The amount of chemical energy depends on the charging efficiency η_{charge} and the efficiency of the solar panels η_{panel} .

$$\dot{Q}_{albedo} = \left(\frac{A_{sat} \cdot 2}{14} \cdot \alpha_{sun,solarcell} \cdot (1 - \eta_{panel}) + \frac{A_{sat} \cdot 2}{14} \cdot \alpha_{sun,solarcell} \cdot \eta_{panel} \cdot \eta_{charge} + \frac{A_{sat} \cdot 1}{14} \cdot \alpha_{sun,cork} + \frac{A_{sat} \cdot 2}{14} \cdot \alpha_{sun,ML \text{ sidepanels}} \right) \cdot albedo_{flux} \cdot I_{sun}$$

$$\dot{Q}_{albedo} = \left(\frac{0,156 \text{ m}^2 \cdot 2}{14} \cdot 0,91 \cdot (1 - 0,3) + \frac{0,156 \text{ m}^2 \cdot 2}{14} \cdot 0,91 \cdot 0,3 \cdot 0,9 + \frac{0,156 \text{ m}^2 \cdot 1}{14} \cdot 0,55 + \frac{0,156 \text{ m}^2 \cdot 2}{14} \cdot 0,610 \right) \cdot 0,3 \cdot 1368 \frac{\text{W}}{\text{m}^2} = 16,17 \text{ W}$$

• **\dot{Q}_{sun} heat radiated by the sun** = $\alpha_{sun} \cdot A_{sat} \cdot F_{sun-sat} \cdot I_{sun}$

One side of the satellite faces to the sun.

$$\dot{Q}_{sun} = \left(\frac{A_{sat} \cdot 2}{14} \cdot \alpha_{sun,solarcell} \cdot (1 - \eta_{panel}) + \frac{A_{sat} \cdot 2}{14} \cdot \alpha_{sun,solarcell} \cdot \eta_{panel} \cdot \eta_{charge} + \frac{A_{sat} \cdot 1}{14} \cdot \alpha_{sun,cork} + \frac{A_{sat} \cdot 2}{14} \cdot \alpha_{sun,ML \text{ sidepanels}} \right) \cdot I_{sun}$$

$$\dot{Q}_{sun} = \left(\frac{0,156 \text{ m}^2 \cdot 2}{14} \cdot 0,91 \cdot (1 - 0,3) + \frac{0,156 \text{ m}^2 \cdot 2}{14} \cdot 0,91 \cdot 0,3 \cdot 0,9 + \frac{0,156 \text{ m}^2 \cdot 1}{14} \cdot 0,55 + \frac{0,156 \text{ m}^2 \cdot 2}{14} \cdot 0,610 \right) \cdot 0,3 \cdot 1368 \frac{\text{W}}{\text{m}^2} = 53,89 \text{ W}$$

$$\bullet \dot{Q}_{earth} \text{ IR radiated by the earth's surface} = \alpha_{IR} \cdot A_{sat} \cdot F_{earth-sat} \cdot I_{earth}$$

Only one side of the satellite receives the IR rays emitted from the earth's surface. According to Kirchhoff's law is $\alpha_{IR} = \varepsilon_{IR}$. So the given ε_{IR} are used for the α_{IR} values in the formula below.

$$\dot{Q}_{earth} = \left(\frac{A_{sat} \cdot 1}{14} \cdot \alpha_{IR,cork} + \frac{A_{sat} \cdot 2}{14} \cdot \alpha_{IR,ML \text{ sidepanels}} \right) \cdot I_{earth}$$

$$\dot{Q}_{earth} = \left(\frac{0,156 \text{ m}^2 \cdot 1}{14} \cdot 0,77 + \frac{0,156 \text{ m}^2 \cdot 2}{14} \cdot 0,886 \right) \cdot 246,5 \frac{W}{\text{m}^2} = 9,100 W$$

$$\bullet \text{ The term } \varepsilon_{IR} \cdot A_{sat} \cdot F_{sat-space} \cdot \sigma$$

Every side, besides the surface which is facing the earth is "viewing" space. The back antenna panel of the satellite is considered to be one multi-layered surface, consisting of fiberfrax and silicon carbide. Therefore an averaged value is calculated for the IR emissivity $\varepsilon_{IR,ML}$ of the multi-layered surface.

$$\varepsilon_{IR,ML \text{ backpanels}} = \frac{3 \text{ mm}}{5 \text{ mm}} \cdot 0,90 + \frac{2 \text{ mm}}{5 \text{ mm}} \cdot 0,87 = 0,888$$

$$\begin{aligned} \varepsilon_{IR} \cdot A_{sat} \cdot F_{sat-space} \cdot \sigma &= \left(\frac{A_{sat} \cdot 4}{14} \cdot \varepsilon_{IR,cork} + \frac{A_{sat} \cdot 6}{14} \cdot \varepsilon_{IR,ML \text{ sidepanels}} + \right. \\ &\left. \frac{A_{sat} \cdot 1}{14} \cdot \varepsilon_{IR,ML \text{ backpanel}} \right) \cdot \sigma = \left(\frac{0,156 \text{ m}^2 \cdot 4}{14} \cdot 0,77 + \frac{0,156 \text{ m}^2 \cdot 6}{14} \cdot 0,886 + \right. \\ &\left. \frac{0,156 \text{ m}^2 \cdot 1}{14} \cdot 0,888 \right) \cdot 5,67 \cdot 10^{-8} \frac{W}{\text{m}^2 \cdot \text{K}^4} \\ &= 5,865 \cdot 10^{-9} \frac{W}{\text{K}^4} \end{aligned}$$

The calculated steady state temperature when the satellite receives sun rays (see equation 4.2).

$$T_{sat,sun} = \sqrt[4]{\frac{\frac{\dot{Q}_{elect}}{\varepsilon_{IR} \cdot A_{sat} \cdot F_{sat-space} \cdot \sigma} + \frac{\alpha_{sun} \cdot albedo \cdot flux \cdot F_{earth-sat} \cdot I_{sun}}{\varepsilon_{IR} \cdot A_{sat} \cdot F_{sat-space} \cdot \sigma}}{\frac{\alpha_{sun} \cdot F_{sun-sat} \cdot I_{sun}}{\varepsilon_{IR} \cdot A_{sat} \cdot F_{sat-space} \cdot \sigma} + \frac{\alpha_{IR} \cdot A_{sat} \cdot F_{earth-sat} \cdot I_{earth}}{\varepsilon_{IR} \cdot A_{sat} \cdot F_{sat-space} \cdot \sigma}} + T_{space}^4}$$

$$T_{sat,sun} = \sqrt[4]{\frac{0,7452 \text{ W}}{5,86 \cdot 10^{-9} \frac{W}{\text{K}^4}} + \frac{16,17 \text{ W}}{5,86 \cdot 10^{-9} \frac{W}{\text{K}^4}} + \frac{53,89 \text{ W}}{5,86 \cdot 10^{-9} \frac{W}{\text{K}^4}} + \frac{9,100 \text{ W}}{5,86 \cdot 10^{-9} \frac{W}{\text{K}^4}} + (3\text{K})^4} = 341,65\text{K} = 68,50^\circ\text{C}$$

The calculated steady state temperature of the satellite during the eclipse (see equation 4.3).

$$T_{sat,eclipse} = \sqrt[4]{\frac{\frac{\dot{Q}_{elect}}{\varepsilon_{IR} \cdot A_{sat} \cdot F_{sat-space} \cdot \sigma} + \frac{\alpha_{IR} \cdot A_{sat} \cdot F_{earth-sat} \cdot I_{earth}}{\varepsilon_{IR} \cdot A_{sat} \cdot F_{sat-space} \cdot \sigma}}{\varepsilon_{IR} \cdot A_{sat} \cdot F_{sat-space} \cdot \sigma}} + T_{space}^4}$$

$$T_{sat,eclipse} = \sqrt[4]{\frac{0,7452 \text{ W}}{5,86 \cdot 10^{-9} \frac{W}{\text{K}^4}} + \frac{9,100 \text{ W}}{5,86 \cdot 10^{-9} \frac{W}{\text{K}^4}} + (3\text{K})^4} = 202,39\text{K} = -70,76^\circ\text{C}$$

A.2. Transient calculation

The following mass budget is based on the geometry of the QARMAN satellite defined within ESATAN-TMS and [8].

Tabel 17: Mass budget used for the transient calculation

Materials	Subsystem	c_p [J/kg.K]	Mass [kg]
Cork	Heat shield	2700	0,360
Solar cells	Solar cells	700	0,336
SiC	Side TPS	1086	0,217
	AeroSDS-panels		0,500
Fiberfrax	Sider TPS	1115	0,046
Ti	Structure +SU back	523	0,263
	SU-boxes (front & middle)		0,287
Pyrogel	AeroSDS-cover + SU-boxes (front, back & middle)	1046,7	0,509
Al 6061	Reaction wheel	893.2	0,127
	Spectrometer		0,300
	Heat sink		0,066
Li-polymer	Batteries	1350	0,071
PCB	Electronics	2284	1,391

$$\sum_{i=1}^n m_i \cdot c_{p,i} = 6571,4 \text{ J/K}$$

It is important to know the duration for the sun (eqn. 4.13) and the eclipse phases (eqn. 4.12) for the transient calculation. The beta angle is calculated with equation 4.12. The orbital parameters which are needed for the following 3 equations are given in table 4.

$$\begin{aligned} \beta &= \arcsin(\cos(\delta_s) \cdot \sin(i) \cdot \sin(\alpha - \alpha_s) + \sin(\delta_s) \cdot \cos(i)) \\ &= \arcsin(\cos(23,45^\circ) \cdot \sin(98^\circ) \cdot \sin(0^\circ - 0^\circ) + \sin(23,45^\circ) \cdot \cos(98^\circ)) = -3,17^\circ \end{aligned}$$

$$\begin{aligned} \Delta t_{eclipse} &= \frac{T_{orbit}}{\pi} \cdot \cos^{-1} \left(\frac{(H^2 + 2R_E H)^{0,5}}{(R_E + H) \cdot \cos \beta} \right) \cdot 60 \text{ s} = \frac{\Delta t_{orbit}/3600s}{\pi} \cdot \cos^{-1} \left(\frac{(H^2 + 2R_E H)^{0,5}}{(R_E + H) \cdot \cos \beta} \right) \cdot 60 \text{ s} \\ &= \frac{1,54}{\pi} \cdot \cos^{-1} \left(\frac{((380 \cdot 10^3 \text{ m})^2 + 2 \cdot (6378 \cdot 10^3 \text{ m} \cdot 380 \cdot 10^3 \text{ m}))^{0,5}}{(6378 \cdot 10^3 \text{ m} + 380 \cdot 10^3 \text{ m}) \cdot \cos(-3,17^\circ)} \right) \cdot 60 \text{ s} = 2171,61 \text{ s} = 36,19 \text{ min} \end{aligned}$$

$$\begin{aligned} \Delta t_{sun} &= \Delta t_{orbit} - \Delta t_{eclipse} = \sqrt{\frac{4 \cdot \pi^2 \cdot a^3}{\gamma \cdot M_E}} - \Delta t_{eclipse} = \sqrt{\frac{4 \cdot \pi^2 \cdot (R_E + H_A)^3}{\gamma \cdot M_E}} - \Delta t_{eclipse} = \\ &= \sqrt{\frac{4 \cdot \pi^2 \cdot (6378 \cdot 10^3 \text{ m} + 380 \cdot 10^3 \text{ m})^3}{6,67 \cdot 10^{-11} \text{ Nm}^2/\text{kg}^2 \cdot 5,97 \cdot 10^{24} \text{ kg}}} - 2171,61 \text{ s} = 3360,07 \text{ s} = 56,00 \text{ min} \end{aligned}$$

In case of starting the iterations with the heating up phase is the minimum equilibrium temperature 202,39K selected as the start temperature T_o for the iterations, see steady state calculations above. The following equation 4.8 is solved in order to find the actual temperature T_a .

$$\Delta t_{sun} = c_{sun} \cdot \left[\left(\operatorname{arctanh} \left(\frac{T_a}{T_{Sat,sun}} \right) + \operatorname{arctan} \left(\frac{T_a}{T_{Sat,sun}} \right) \right) - \left(\operatorname{arctanh} \left(\frac{T_o}{T_{Sat,sun}} \right) + \operatorname{arctan} \left(\frac{T_o}{T_{Sat,sun}} \right) \right) \right]$$

Where:

$$T_o = 219,25\text{K (changes with every iteration)}$$

$$T_{Sat,sun} = 341,65\text{K}$$

$$c_{sun} = \frac{\frac{\sum_{i=1}^n m_i \cdot c_{p,i}}{\epsilon_{IR} \cdot A_{sat} \cdot \sigma}}{2 \cdot T_{Sat,sun}^3} = \frac{\frac{6571,4 \text{ J/K}}{\left(0,77 \cdot \frac{5}{14} + 0,888 \cdot \frac{1}{14} + 0,886 \cdot \frac{8}{14}\right) \cdot 0,156 \text{ m}^2 \cdot 5,67 \cdot 10^{-8} \frac{\text{W}}{\text{m}^2 \cdot \text{K}^4}}{2 \cdot (341,65\text{K})^3}} = 13063\text{s}$$

The above given equation for the heating up phase is true when T_a , the temperature at the end of the heating up phase, is equal to 226,35K. Temperature T_a is the starting temperature T_o for the cooling down phase.

$$\Delta t_{eclipse} = c_{eclipse} \cdot \left[\left(\operatorname{arccoth} \left(\frac{T_a}{T_{Sat,eclipse}} \right) + \operatorname{arctan} \left(\frac{T_a}{T_{Sat,eclipse}} \right) \right) - \left(\operatorname{arccoth} \left(\frac{T_o}{T_{Sat,eclipse}} \right) + \operatorname{arctan} \left(\frac{T_o}{T_{Sat,eclipse}} \right) \right) \right]$$

Where:

$$T_o = 226,35\text{K (changes with every iteration)}$$

$$T_{Sat,eclipse} = 202,39\text{K}$$

$$c_{eclipse} = \frac{\frac{\sum_{i=1}^n m_i \cdot c_{p,i}}{\epsilon_{IR} \cdot A_{sat} \cdot \sigma}}{2 \cdot T_{Sat,eclipse}^3} = \frac{\frac{6571,4 \text{ J/K}}{\left(0,77 \cdot \frac{5}{14} + 0,888 \cdot \frac{1}{14} + 0,886 \cdot \frac{8}{14}\right) \cdot 0,156 \text{ m}^2 \cdot 5,67 \cdot 10^{-8} \frac{\text{W}}{\text{m}^2 \cdot \text{K}^4}}{2 \cdot (202,39\text{K})^3}} = 62834\text{s}$$

The above given equation for the cooling down phase is true when T_a , the temperature at the end of the heating up phase, is equal to 223,51K. Temperature T_a is the starting temperature T_o for a new iteration for the heating up phase. The iteration stops when the temperature difference between 2 consecutive iterations is lower than 1K. Table 7 shows the results for the iterations carried out for this example.

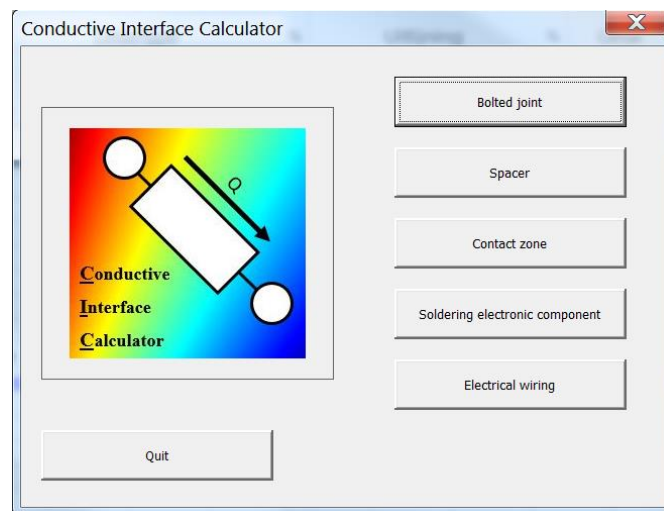
Temperature at the end of:	Iteration 1	Iteration 2	Iteration 3	Iteration 4	Iteration 5
Sun phase T_{max}	226,35K	245,56K	260,01K	270,31K	277,33K
Eclipse phase T_{min}	223,51K	239,80K	251,64K	259,84K	265,31K

Iteration 6	Iteration 7	Iteration 8	Iteration 9	Iteration 10
281,97K	284,96K	286,86K	288,06K $\Delta T < 1\text{K}$	288,81K
268,88K	271,16K	272,60K	273,49K $\Delta T < 1\text{K}$	274,06K

Appendix B

Conductive interface calculator

The Conductive Interface Calculator is able to calculate 5 different conductive interfaces, namely: bolted joints, spacers, contact zones, soldering interfaces of electronic components and bundles of electrical wiring. The interfaces are designed in such a way that it is immediately clear to the user which parameters are needed to define one of the previous mentioned conductive interfaces. The intermediate results of different calculations can be found in the different excel spreadsheet, which at the meanwhile allows experienced users to adapt other parameters than the ones suggested in the interfaces.



Figur 78: Start interface conductive Interface Calculator

B.1 Bolted joint

Conductive Interface Calculator Bolted Joint

Plate 1 thickness [mm] =

Plate 2 thickness [mm] =

Surface roughness of the plates [μm] = Nominal ($0,216\mu\text{m} \leq \sigma \leq 9,6\mu\text{m}$)
 ?

Bolt type: (Options: M1.6, M2, M2.5, M3, M3.5, Other type)

Material plate 1: (Options: Ti-6Al-4V(grade5), Copper 360 alloy, SST 316, Al6061-T6, Other material)

Material plate 2: (Options: Ti-6Al-4V(grade5), Copper 360 alloy, SST 316, Al6061-T6, Other material)

Material bolt: (Options: Ti-6Al-4V(grade5), Copper 360 alloy, SST 316, Al6061-T6, Other material)

Buttons: Quit, Calculate, Detailed calculation

Figure 79: Interface for the bolted joint

Figure 79 shows the interface for the calculation of the conductance for a bolted joint, where two titanium Ti-6Al-4V plates with each a thickness of 3mm are bolted together with a titanium M3 bolt. When no surface roughness is specified, the default value of $1,27 \mu\text{m}$ is used for the calculations. A GL value of $0,0036 \text{ W/K}$ is calculated with “calculate”. The bottom “detailed calculation” shows the different thermal resistance of the bolted joint resistance network (see figure 80).

Figure 80 shows the interfaces which has to be filled in when another bold than M1.6, M2, M2.5, M3 or M3.5 needs to be used.

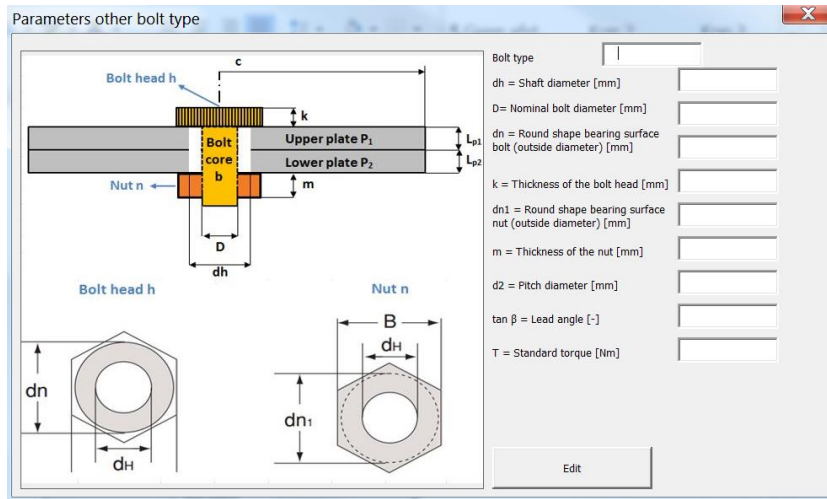


Figure 80: Interface to determine other bolts

Other plate materials than the ones listed are specified by entering the following information: thermal conductivity of the plate, poisson’s ratio of the plate, young’s modulus of the plate and hardness brinell number for the plate’s material. Another bolt’s material is defined by specifying the thermal conductivity of the bolt’s material.

After clicking on the “detailed calculation” in the interface for the bolted joint (see figure 79) and clicking on the “calculate” in the appeared interfaces, are the results of the different thermal resistances of the thermal network for a bolted joint shown.

calculated with “calculate”. There is again a possibility to define other spacer types or another material for the spacer.

Figure 83: Interface for spacer

Other plate materials for the spacers than the ones listed are specified by determining the following information: thermal conductivity, poisson’s ratio and young’s modulus of the spacer’s material

B.3 Contact zone

Figure 84 shows the interface for the calculation for a contact zone, where two copper-360 alloy plates where touching each other with a medium pressure. When no surface roughness is specified, the default value of 1,27 µm is used for the calculations. A contact conductance of 33855,77 W/m²K is calculated with “calculate”.

The contact pressure which can be selected in the conductive interface calculator are categorized in soft, medium and hard, where the contact pressure is respectively equal to 0,1 MPa, 5 MPa and 10 MPa. Those contact pressures are chosen because most of the tables in literature present contact conductance values for those pressures.

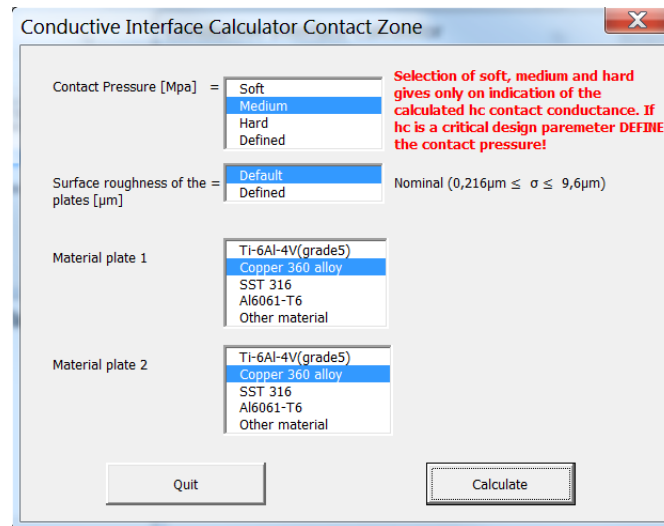


Figure 84: Interface for contact zone

B.4 Soldering of electronic components

Figure 85 shows the interface for the calculation of the linear conductance value GL for soldering interface of an electronic component. The electronic component connected with soldering to a PCB with a thickness of 1,33 mm has an groundpad of 200 mm² and 100 pins. A linear conductance value of 0,1637 W/K is calculated with the bottom “calculate”.

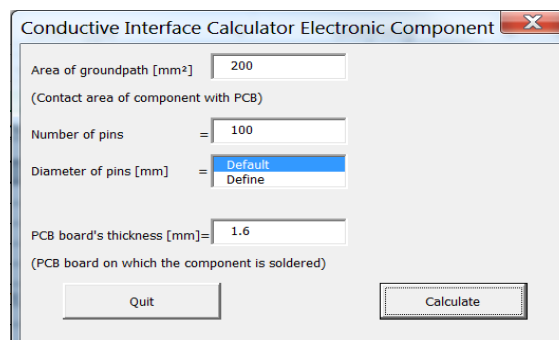


Figure 85: Interface for soldering of an electronic component

B.5 Bundle of electrical cables

Figure 86 shows the interface for the calculation of the linear conductance value GL for a bundle of electrical cables. The bundle of electrical wiring defined in the user interface for electrical wiring, can consist out three types of cables. For the following example is the bundle of cables formed by 5 wires from the type AWG-24 and 1 coax cable of the type RG-174 with a length of 100 mm. No second type of wire is defined. The selection fields also allow the user to define the different materials for the core, jacket, insulation and shield. A linear conductance value of 0,0047 W/K is calculated with the bottom “calculate”.

Conductive Interface Calculator Electrical Wiring

Length of the cables [mm]

The calculator calculates the thermal conductance of a bundle cables

1. First sort

Type
 None
 Wire

Number of Wires :

Wire gauge
Define
AWG-24
AWG-26

Material Core
Define
Copper

Material Jacket
Define
(PE) Polyethylene
(PTFE) Polytetrafluoroethylene

2. second sort

Type
 None
 Wire

Number of Wires :

Wire gauge
Material Core
Material Jacket

3. Third sort

Type
 None
 Coax cable

Number of coax cables:

Wire gauge
Define
RG-147
RG-174

Material Core
Define
Copper

Material Insulation
Define
(PE) Polyethylene
(PTFE) Polytetrafluoroethylene

Material Shield
Define
tinned plated Al, braided
pure Cu, braided

Material Jacket
Define
(PE) Polyethylene
(PTFE) Polytetrafluoroethylene

Quit Calculate

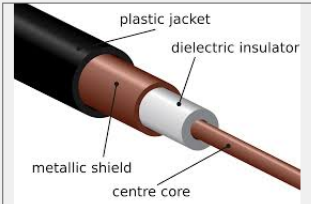


Figure 86: Interface for bundle of electrical wires

Appendix C

Uncertainty analysis re-entry

C.1 Pareto plots

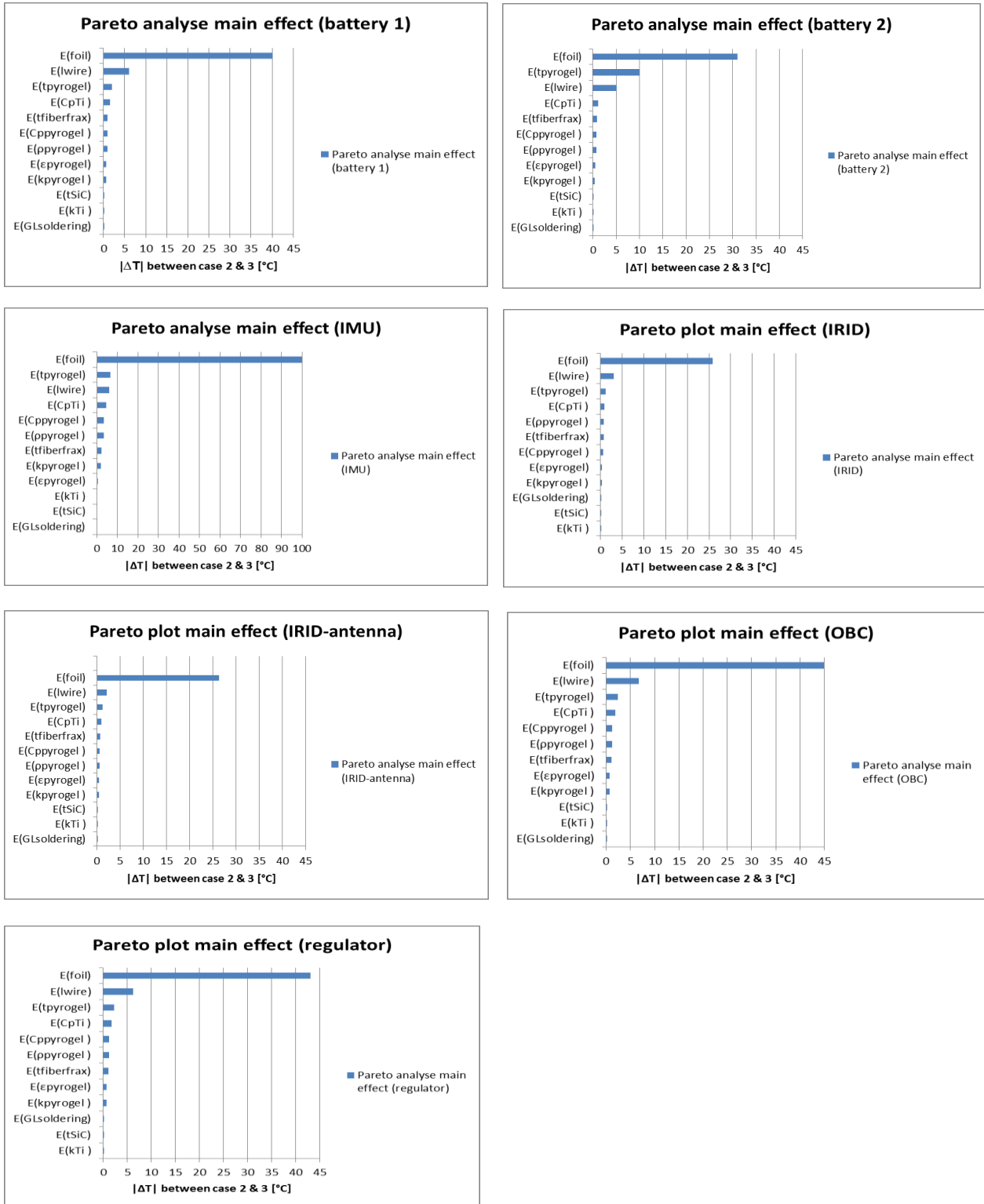
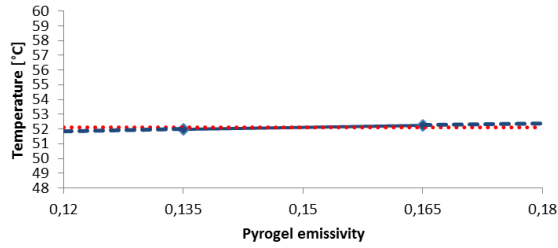


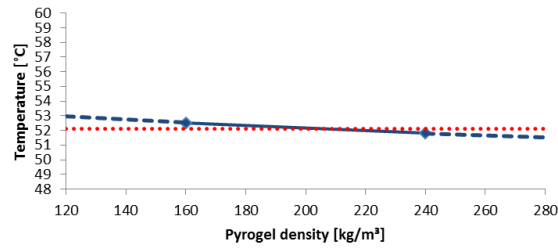
Figure 87: Pareto plot for the main effects (time 1400s during re-entry selected as reference)

C.2 Main effect plots

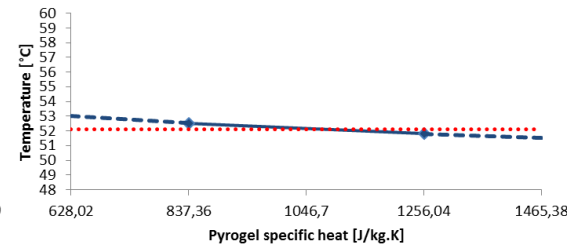
Main effect plot of response:
Pyrogel emissivity (Battery 2)



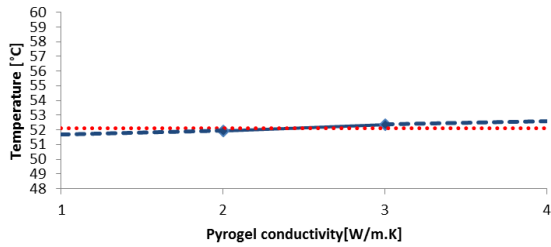
Main effect plot of response:
Pyrogel density (Battery 2)



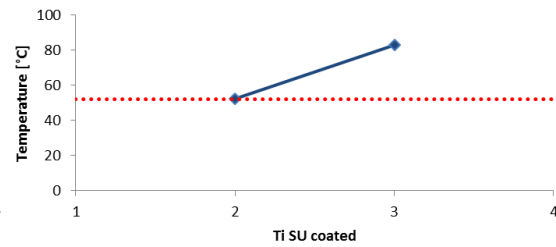
Main effect plot of response:
Pyrogel specific heat (Battery 2)



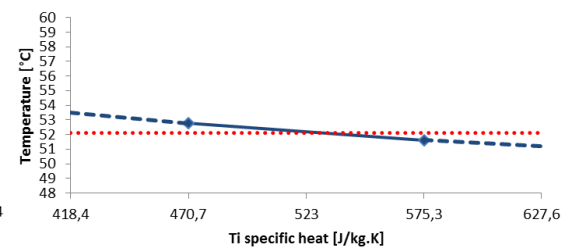
Main effect plot of response:
Pyrogel conductivity (Battery 2)



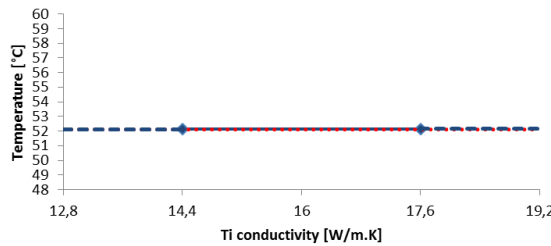
Main effect plot of response:
Ti Survival Unit coated (Battery 2)



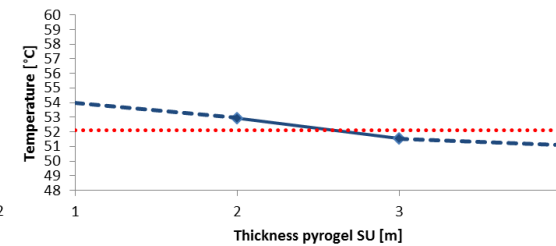
Main effect plot of response:
Ti specific heat (Battery 2)



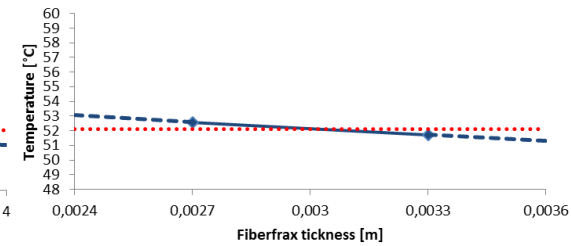
Main effect plot of response:
Ti conductivity (Battery 2)



Main effect plot of response:
Thickness pyrogel SU (Battery 2)



Main effect plot of response:
Fiberfrax tickness (Battery 2)



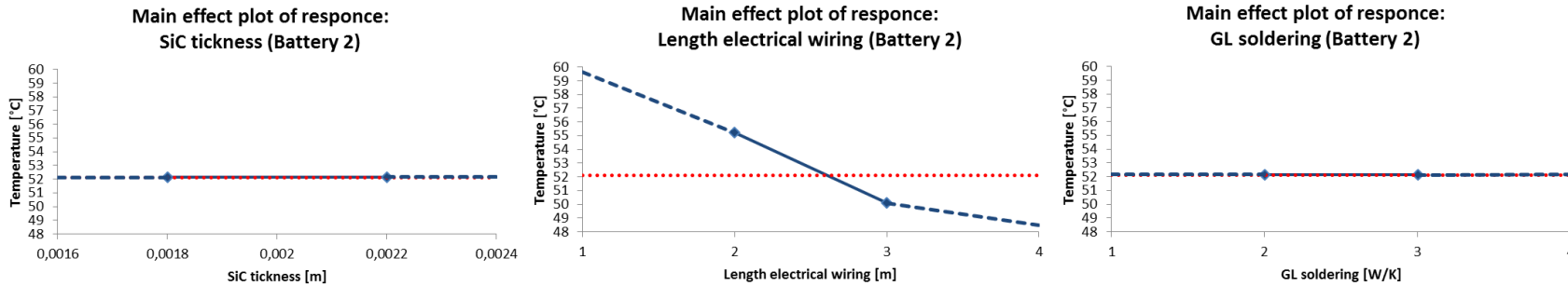
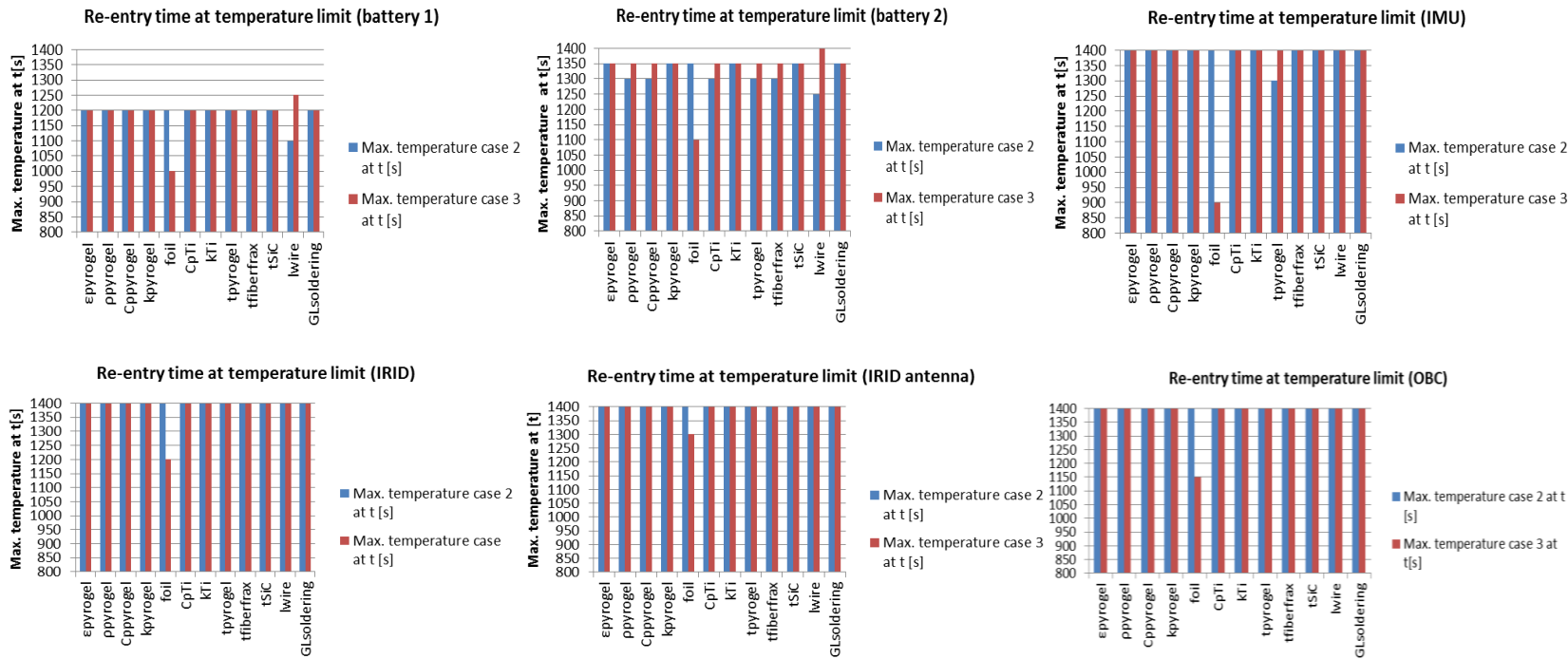


Figure 88: Main effect plots of battery 2 (time 1400s during re-entry selected as reference)

C.3 Reached temperature limit during re-entry



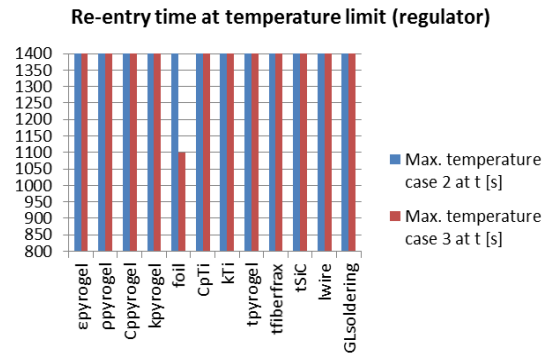


Figure 89: Limit temperature at time t during re-entry

C.4 Results DOE

Test	Test case description		
	X ₁ (ε _{foil})	X ₂ (l _{wire})	X ₃ (t _{pyrogel})
1	0,15	-20%	-1mm
2	0,3	-20%	-1mm
3	0,15	+20%	-1mm
4	0,3	+20%	-1mm
5	0,15	-20%	+1mm
6	0,3	-20%	+1mm
7	0,15	+20%	+1mm
8	0,3	+20%	+1mm

Test	Coded test cases												Z _{av.} [°C]
	I	X ₁	X ₂	X ₃	X ₁ .X ₂	X ₁ .X ₃	X ₂ .X ₃	X ₁ .X ₂ .X ₃	Z ₁ [°C]	Z ₂ [°C]	Z ₃ [°C]	Z ₄ [°C]	
1	1	-1	-1	-1	1	1	1	-1	94,10	97,24	92,22	94,91	94,62
2	1	1	-1	-1	-1	-1	1	1	112,19	116,47	110,59	113,62	113,22
3	1	-1	1	-1	-1	1	-1	1	89,35	92,92	87,64	89,71	89,91
4	1	1	1	-1	1	-1	-1	-1	107,35	108,28	105,93	112,08	108,41
5	1	-1	-1	1	1	-1	-1	1	84,05	80,41	82,36	83,16	82,50
6	1	1	-1	1	-1	1	-1	-1	96,41	94,48	99,18	97,59	96,92
7	1	-1	1	1	-1	-1	1	-1	74,62	72,83	76,48	74,91	74,71
8	1	1	1	1	1	1	1	1	94,63	89,65	91,37	92,07	91,93

Test	I.Z	X ₁ .Z	X ₂ .Z	X ₃ .Z	X ₁ .X ₂ .Z	X ₁ .X ₃ .Z	X ₂ .X ₃ .Z	X ₁ .X ₂ .X ₃ .Z	S _i ²
1	94,62	-94,62	-94,62	-94,62	94,62	94,62	94,62	-94,62	2,41
2	113,22	113,22	-113,22	-113,22	-113,22	-113,22	113,22	113,22	3,93
3	89,91	-89,91	89,91	-89,91	-89,91	89,91	-89,91	89,91	3,15
4	108,41	108,41	108,41	-108,41	108,41	-108,41	-108,41	-108,41	4,87
5	82,50	-82,50	-82,50	82,50	82,50	-82,50	-82,50	82,50	2,40
6	96,92	96,92	-96,92	96,92	-96,92	96,92	-96,92	-96,92	2,21
7	74,71	-74,71	74,71	74,71	-74,71	-74,71	74,71	-74,71	1,19
8	91,93	91,93	91,93	91,93	91,93	91,93	91,93	91,93	4,17
Sum=	752,20	68,75	-22,29	-60,10	2,71	-5,47	-3,25	2,90	24,34

effect i	β_i	$t_i = \beta_i/S_{\text{effect}}$	$t_i < 2.12$	Z=
$\beta_0=$	94,03	304,95	304,95	94,03
$\beta_1=$	8,59	27,87	27,87	8,59
$\beta_2=$	-2,79	-9,04	9,04	-2,79
$\beta_3=$	-7,51	-24,37	24,37	-7,51
$\beta_{12}=$	0,34	1,10	1,10	0,34
$\beta_{13}=$	-0,68	-2,22	2,22	-0,68
$\beta_{23}=$	-0,41	-1,32	1,32	
$\beta_{123}=$	0,36	1,17	1,17	